Graphene oxide-magnetite hybrid nanoadsorbents for toxin removal in aqueous system

Dissertation submitted to the

National Institute of Technology Rourkela

in partial fulfillment of the requirements of the degree of

Master of Technology (Research)

in

CERAMIC ENGINEERING

by

Pranati Badhai

Roll No: 613CR3002

Under the Supervision of

Prof. Shantanu Kumar Behera

AUGUST, 2016

Department of Ceramic Engineering

National Institute of Technology,

Rourkela- 769008, Odisha

Department of Ceramic Engineering
NATIONAL INSTITUTE OF TECHNOLOGY,
ROURKELA
Orissa-769008

CERTIFICATE

This is to certify that the thesis entitled ***"Graphene oxide-magnetite hybrid nanoadsorbents for toxin removal in aqueous system"*** submitted by ***Pranati Badhai*** for the degree of **Master of Technology (Research)** in **Ceramic Engineering** to the National Institute of Technology, Rourkela, is a record of bonafide research work carried out by her under my supervision and guidance. Her thesis, in my opinion, is worthy of consideration for the award of degree of Master of Technology (Research) in accordance with the regulations of the institute.

The results embodied in this thesis have not been submitted to any other university or institute for the award of a degree.

Dr. Shantanu K. Behera

Assistant Professor
Department of Ceramic Engineering
National Institute of Technology, Rourkela

Declaration

I hereby declare that my M.Tech (Research) thesis is entitled as "***Graphene oxide-magnetite hybrid nanoadsorbents for toxin removal in aqueous system*".** This thesis is my own work and has not been submitted in any form for another degree or diploma at any university or other institution of tertiary education. Information derived from the published and unpublished work of others has been acknowledged in the text and a list of references given in this thesis.

Pranati Badhai

_____ _____

Date Signature

Acknowledgement

It is with the most sincere thanks to who helped me to make this thesis possible.

I wish to express my deep, sincere gratitude to advisor ***Prof. Shantanu Kumar Behera*** for assigning me the project and for his inspiring guidance, constructive criticism and valuable suggestion throughout this research work.

I express my sincere thanks to *Prof. B. B Nayak*, Head of the Department, Ceramic Engineering for providing me all the departmental facilities required for the completion of the project work. I am also thankful to all other faculty members of the Department of Ceramic Engineering, NIT Rourkela for their constructive suggestions and encouragement at various stages of the work.

My sincere thanks to all non-teaching staffs in Department of Ceramic Engineering for providing full of high-spirited delight in the lab and helping me throughout this project.

My sincere indebted to my senior research colleagues *Abhisek Choudhary, Swarnima Kashyap, Pallavi Suhasinee Behera, Aiswarya Dash and Satyananda Behera* for their unconditional support and constant motivation whenever needed. I am very grateful my friends *Biswajit Baruah, Ipsita Swain, P. Venkatesh, P. Sreenivasulu, Soumya Prakash Sahoo and Sanjay Krishna Mohan*, who have given me their friendship, put up with my odd hours, and provided me with lifts and practical help.

Last but not least, I would like thank to my ***dear parents*** who have patiently extended all kinds of help for accomplishing this work.

Pranati Badhai

Roll no. 613CR3002

ABSTRACT

Rapid industrialization has led to massive environmental pollution, resulting in damage to the ecosystem and human health. Dyes and heavy metals are non-biodegradable toxins that possess carcinogenic and mutagenic properties. With the rising scarcity of water, these toxins need to be removed from water bodies economically and efficiently. Among all the classical wastewater treatment techniques, including complexation, chemical oxidation or reduction, solvent extraction, chemical precipitation, adsorption is the most promising separation method. However, it is a challenge to design adsorbent materials with high specific surface area and appropriate chemical functionality to selectively adsorb toxins.

The present work demonstrates one of the new types of adsorbent materials, which is a hybrid of graphene oxide (GO) and magnetite. Nanostructured two dimensional sheets, such as GO, can act as anchor points where the ceramic magnetic oxide can be precipitated, thus reducing the latter's agglomeration tendency and expose active sites effectively. A facile sonication assisted synthesis was adopted to prepare the hybrids, and tested for their toxin adsorption properties against three distinctly different materials. The adsorption characteristics of Cr(VI) (toxic heavy metal contaminant), malachite green (a toxic cationic dye), and phenol red (a neutral dye) on to the GO-Fe_3O_4 hybrids was systematically investigated. The hybrids exhibited better adsorption properties than that of bare Fe_3O_4 nanoparticles. In addition, the hybrids were proved to be an excellent material for the separation of malachite green, with efficiency as high as 97%, with faster kinetics. The removal efficiency of phenol red was moderate, owing to the lack of charge on the dye; upto 68% removal was observed due to the interaction of the zwitterions with the adsorbents.

The presentation aims to discuss the effects of time, pH, and concentration on adsorption. The experimental results will be analyzed based on various kinetic models, including pseuo-first order, pseudo-second order, intraparticle diffusion, Bangham model. Equilibrium adsorption isotherms of these toxins on the GO-Fe_3O_4 hybrids will be discussed in the context of Langmuir, Freundlich, Temkin and Dubinin-Radushkevich models.

Keywords: Adsorption, hybrid, hexavalent chromium, malachite green, phenol red

Table of Contents

List of figures

List of tables

CHAPTER-1

INTRODUCTION

In this section, the nature of the problem is introduced. Out of the many adsorbents used in the literature, the selection of a specific type of hybrid ceramic is introduced. Subsequently, the scope of the work is outlined, for the use of the synthesized nanoadsorbents in the removal of hexavalent chromium, malachite green, and phenol red.

One of the most pressing problems the world is facing today is access to clean uncontaminated water for domestic and industrial use. Anthropogenic activities and rapid industrialization have led to the discharge of a range of toxins to water bodies causing irremediable damage to the ecosystem [1-3]. Such ecological imbalances create new forms of diseases. The fact that water is moving throughout the world continuously changing its states, there is no gain or loss of water as a whole. Thus, contaminated water left untreated can continue to remain in the aqueous environment, and get absorbed by living organisms. Heavy metal ions, including lead, zinc, chromium, copper, mercury, arsenic, and many more are indiscriminately released into the water bodies [4]. Unlike organic pollutants, heavy metals are non-biodegradable in the environment, and also can accumulate in living tissues, particularly in human bodies, causing significant physiological damage [5]. Such disorders include damage to the central nervous system, blood composition, and irreversible damage to vital organs of the body. Chromium is one of the important hazardous heavy metal ions in the environment. It's most commonly occurring oxidation states are +3 and +6, among which the +6 state is more toxic. The hexavalent state is not a stable oxidation state and has a tendency to get reduced to +5 (completely unsafe) and +3 (relatively safe) inside the human body. Exposure to hexavalent chromium beyond its permissible limit can cause gastro intestinal disorders, damage RBCs (Red Blood Cells), reduce blood platelets, and cause asthma in the human body [6]. Therefore, removal of hexavalent chromium is an important area of work.

Dyes, a common waste from textile and leather industries, are well known to influence the quality of water due to their toxicity and carcinogenic effects [7]. Extremely low concentrations of dye in water is visible and unsuitable for use. Most of the dyes have complex aromatic structures, render the penetration of UV-light into water bodies making difficulties in various photocatalytic activities in the aquatic system. Exposure to carcinogenic dyes can permanently damage eyes, liver, kidney in living beings. Hence, the presence of heavy metals and organic matters in natural water and industrial wastewaters is a subject of great interest in environmental engineering owing to its great relative impact on daily lives worldwide [8].

Various technological approaches including, complexation, chemical oxidation or reduction, solvent extraction, chemical precipitation, reverse osmosis, ion exchange, filtration, membrane

processes, evaporation and coagulation are reported in the literature, for the treatment or removal of toxic heavy metal from contaminated wastewater [9-15]. However, these techniques are not very popular owing to certain disadvantages including, incomplete removal, high consumptions of reagent and energy, low selectivity, high capital and operational cost, and generation of secondary wastes that are difficult to be disposed of [16, 17]. For example, among the conventional methods, precipitation method followed by coagulation is particularly reliable for the removal of heavy metals from water [18]. But this process requires large settling tanks for precipitation of large volumes of sludge and requires subsequent treatment. Membrane filtration is a proven way to remove heavy metals. But its high cost limits the widespread use of this method [19]. For situations where the concentration of heavy metal ions is high in wastewaters, the traditional removal techniques can be suitable. However, it becomes ineffective when the concentration of heavy metals are low, but the water is still unsuitable for usage [20].

Besides the classical wastewater treatment techniques, adsorption of heavy metals is the most promising separation and purification method possessing many advantages including, high efficiency in removing very low levels of pollutants from dilute solutions, easy handling, high selectivity, lower operating cost, minimum production of chemical or biological sludge and regeneration of adsorbent [21-23]. Adsorption is a process by which molecules of a substance such as gas or liquid, accumulate on the surface of another solid material. Toxins, called as adsorbate in adsorption process, are attracted and bound to the adsorbent by different mechanisms. The mechanism of adsorption is complex and considered to take place via several mechanisms including, chemisorption complexation, coordination, chelating, physical adsorption, micro precipitation [24, 25] and ion exchange [26].

Hence, the approach followed in this work is to synthesize a novel, economical, easily available synthetic nanoadsorbent, which comprises a strong affinity and loading capacity. Some of the reported low-cost adsorbents include rice husk [27], flyash [28], pine bark [29], saw dust [30] and animal bone [31] for heavy metal ions removal. In conventional treatment processes, activated carbons have been widely used as an adsorbent for decontamination of drinking and wastewaters. Although activated carbon has large surface area and high adsorption capacity,

the high cost of activated carbon limits its use as an adsorbent [32]. Carbon-based materials including carbon nanotubes (CNTs) are very well known as adsorbents. Yet again, a prohibitively expensive material cannot be used for such a common and extremely large scale use, such as water decontamination.

Graphene, a fascinating two dimensional carbon-based material possessing atomic thickness and high surface to volume ratio, has attracted considerable attention world over. But its separation problems and hydrophobic nature limit their practical application in water. Additionally, graphene has a tendency to agglomerate due to strong van der Waals forces, leading to drop in the surface area, hence a reduction in adsorption performance [33]. An apparent solution to this problem is chemical functionalization of graphene materials. Graphene oxide (GO) is a highly oxidized form of graphene, generally prepared by chemical oxidation of graphite resulting in extended graphene sheets decorated with (-COOH), carbonyl (-C-O), epoxy (C-O-C) and hydroxyl (-OH) groups. One of the major advantages with GO is that it is hydrophilic with very high negative charge density arising due to the oxygen containing functional groups. These functional groups are also responsible for the formation of stable aqueous colloid that can be obtained by simple sonication. GO can act as weak acid cation exchange resin because of the ionizable carboxyl groups. However, the problem associated with GO is the difficulty in separation of the materials from an aqueous system, leading to recontamination of water and nanotoxicity [33].

A solution to all of these problems is the incorporation of molecules and nanomaterials into GO sheets, which can arrest the agglomeration, increase surface area and adsorption capacity. Moreover, if the incorporated material is magnetic in nature it the overall composite can become magnetically separable, thus mitigating separation issues. Among the magnetic materials magnetite (Fe_3O_4) is the oldest known magnetic material with excellent magnetic properties and surface area. There is much recent interest in the use of engineered magnetite nanoparticles in wastewater treatment because of nanosized particles, easily magnetic separable, low cost and eco-friendly nature [34]. But magnetite nanoparticles have poor thermal stability, and they further oxidize to maghemite and hematite, thus limiting adsorption

efficiency. It also possesses strong magnetic dipoles leading to decrease in surface area and drop in adsorption capacity.

Keeping the above facts in mind, in the present work we have explored the use of a hybrid material by incorporating magnetite nanoparticles into GO sheets where the graphene oxide sheets act as substrates for Fe_3O_4 precipitation. The hydrophilic nature of the GO sheets keep the hybrid materials dispersed in the aqueous system and retard the leaching of Fe_3O_4 during water treatment process. The motivation of this work is to maximize the practical use of the combined advantages of both the components as active materials for improving the adsorption performance. In the present work, nanoparticulate Fe_3O_4 was synthesized individually, as well as anchored in GO sheets by a facile sonication assisted straight forward wet chemical route. The batch adsorption study was performed for Cr(VI) removal by bare magnetite particles as well as by the GO-Fe_3O_4 hybrid material and studied the effect of various process parameters (including adsorbent dose, pH, contact time, and initial concentration) on adsorption capacity was studied. The hybrid material was also tested for the removal of malachite green (a toxic cationic dye) and phenol red (a toxic neutral dye) followed by the study of the effect of various process parameters on it. Enhanced adsorption capacity and excellent adsorption kinetics were established the studied approach. For a better understanding of adsorption mechanisms, different kinetic models including, pseudo-first order, pseudo-second order, Weber-Morris, Elovich, and Bangham were applied to study the experimental data. Further, to understand equilibrium adsorption kinetics, various empirical isotherm models, including Langmuir, Freundlich, Dubinin–Radushkevich, and Temkin were applied to model the experimental data. Finally, all of the experimental results were assimilated to suggest the efficacy of the nanoadsorbents for the removal of the toxins.

CHARTER-2

LITERATURE REVIEW

In this section, relevant literature on the process of toxin removal using various adsorbents is reviewed. First the carbon based adsorbents are discussed, followed by that of various Fe based oxide nanoparticles. Subsequently, the recent literature based on the use of GO-Fe_3O_4 materials as adsorbents is reviewed. Then, literature based on the three different toxins used in this work are examined with regards to their effects, and the various adsorbents used for removal of these toxins.

The contamination of surrounding water bodies is mainly due to uncontrolled anthropogenic activities in the society and direct discharge of untreated industrial waste into water reservoirs, including rivers and lakes. Contamination of water is dangerous to living organisms that directly or indirectly use water for life processes. Adsorption is most widely used, feasible, and inexpensive method suitable for the separation of all kinds of contaminants, including heavy metals, dyes, and organic pollutants. The following paragraphs provide a brief overview of different types of adsorbent material, their synthesis, properties and performance in the field of water treatment.

Fu et al. [35] reviewed the literature on removal of heavy metals from waste water through chemical precipitation, ion-exchange, adsorption, membrane filtration, coagulation, flocculation, flotation, and electrochemical methods. They concluded that adsorption was recognized as an effective and economical method for low concentration heavy metal removal by low-cost adsorbents and biosorbents. Additionally, the adsorbent of heavy metals by biosorbent is summarized through a review paper by *Febrianto et al.* [36]. The purpose of this paper was to explain biosorption of heavy metals through adsorption equilibria and kinetic modeling. Pseudo-first order and pseudo-second order rate equations have been widely used for studying the kinetics of biosorption of heavy metals from aqueous solutions. Various empirical models were fitted to explain the interaction of adsorbent surface with adsorbate materials.

2.1. Carbon Based Materials as Adsorbents

Carbon based materials have been preferred by many scientists for adsorption experiments due to their inherent large surface area. Activated carbon, a form of carbon that generally has much higher specific surface area than other carbon forms, has got remarkable attention for the removal of various pollutants, especially metal ions from drinking water [37, 38]. Due to economic considerations, use of activated carbon, however, has been limited. But, new inexpensive ways are progressively being found using activated carbon prepared from industrial and agricultural waste [39, 40]. Other low cost adsorbents, such as saw dust, distillery sludge and biomass, have also been developed for the removal of hexavalent chromium from

waste water [41-43]. However, these low cost adsorbents could not be used at industrial scale due to their poor mechanical stability. Additionally, their disposal also has created problems, thus further aiding environmental pollution.

Carbon nano tubes (CNTs) are amongst the newer forms with nanostructured size and unique morphology that have been found to be popular as adsorbents [44, 45]. *Stafiej et al.* [46] used carbon nanotubes as efficient adsorbent for Cu^{2+}, Co^{2+}, Cd^{2+}, Zn^{2+}, Mn^{2+}, Pb^{2+}. Adsorption efficacy of CNTs as a function of pH and initial metal ion concentration were studied. Optimum conditions were pH-9 for toxin removal, and the equilibrium adsorption followed Freundlich isotherm. To improve the adsorption efficiency functionalization of CNTs was done through surface oxidation. *Tofighy et al.* [47] also studied the adsorption of divalent metal ions (Cu^{2+}, Zn^{2+}, Pb^{2+}, Cd^{2+}, Co^{2+}) using oxidized carbon nanotubes, synthesized by chemical vapor deposition of cyclohexanol and ferrocene in a nitrogen atmosphere. Various isotherms, kinetics of adsorption and its variation with initial metal ion concentration were studied with a preferential ordered of adsorption as $Pb^{2+} > Cd^{2+} > Co^{2+} > Zn^{2+} > Cu^{2+}$. *Rao et al.* [44] reviewed adsorption of divalent metal ions by both raw and surface oxidized CNTs showing that oxidation of CNTs remarkably increased the potential for adsorption. Effects of adsorption parameters on adsorption followed by competition of specific metal ion adsorption in the presence of multiple ions were also addressed. They achieved regeneration of CNTs using an acid solution, which considerably damaged the adsorbent bed. CNTs are not only shown potential adsorption capacity for metal ions but also employed for dye pollutants including azo dyes [48], reactive dyes [49] and direct dyes etc. [50]. *Gupta et al.* [45] reviewed adsorption of dyes from aqueous solution using CNTs and modified CNTs composites. They discussed the interaction sites on CNTs and adsorption capacity of functionalized CNTs. It showed that these materials show better results than non-functionalized single and multi-walled CNTs. Although many progresses have been made using CNTs as an adsorbent material, its fabrication cost limits their application in a larger scale. In addition, the nanotoxicity of CNT based materials in living organisms is not clearly understood. Also complete regeneration of CNTs is not a cost effective process. [51, 52].

A possible alternative to CNTs is "graphene", which is another carbon based material with a lattice of sp^2 hybridized carbon atom sheet with a great surface area. Graphene is the thinnest but strongest material and can be synthesized easily from graphite. This material also has acquired considerable attention in the field of water treatment, as can be seen from the following.

Liu et al. [53] reported use of graphene prepared by modified Hummers' method for adsorption of methylene blue from aqueous solution. Investigations describing the effect of various process parameters on the adsorption capacity of methylene blue onto prepared adsorbent were done. The experimental data followed Langmuir adsorption isotherm at 293 K with a maximum adsorption capacity of 153.85 mg g^{-1}. The calculated thermodynamic parameters suggested that adsorption process of methylene blue is endothermic, spontaneous, and followed pseudo second-order kinetics.

Use of graphene as an adsorbent for fluoride removal from aqueous solution has been explored by *Li et al.* [54]. The batch experiments as a function of pH, contact time, and temperature were evaluated resulting optimum initial fluoride concentration and temperature to be of 25 mg L^{-1} and 298 K, respectively. The experimental data fitted well to Langmuir isotherm model, resulting in maximum fluoride adsorption capacity of 35.59 mg g^{-1} at pH-7. The adsorption of fluoride showed pseudo-second-order kinetics and was found to be a spontaneous, endothermic, and irreversible process, as investigated by thermodynamic parameters calculation.

Zhao et al. [55] have taken graphene sponge prepared by hydrothermal treatment of graphene with the use of thiourea. They developed a sponge like very porous but mechanically stable structure, which can be used for the removal of dyes, oils and other organic pollutants. Graphene sponges are found to have efficient adsorption capacity for both cationic and anionic dyes. Adsorption of dyes are highly dependent on the surface charges associated with the dye structures and the specific surface area of adsorbent material. Oil adsorption capacity was 129 mg g^{-1}, primarily due to high specific surface area of graphene sponge. The adsorption capacity of methylene blue, rhodamine B and methyl orange onto graphene sponges are calculated to

be 184 mg g^{-1}, 72.5 mg g^{-1} and 11.5 mg g^{-1}, respectively. Moreover, the regeneration of graphene sponge can be done by simple treatment without structural degradation.

Decontamination of Bisphenol A (BPA) from aqueous solution on graphene was explored by *Xu et al.* [56]. The maximum adsorption capacity (q_m) of graphene for BPA obtained from a Langmuir isotherm was 182 mg g^{-1} at 302.15 K, and the kinetics followed pseudo-second-order model. The thermodynamic studies indicated that the adsorption process was spontaneous and exothermic process. It was suggested that both π-π interactions and hydrogen bonds might be responsible for the adsorption of BPA on graphene. Besides, the presence of NaCl in the solution was also speculated to facilitate the adsorption process, whereas the alkaline pH range and higher temperature of the solution were unfavorable.

The literature studied proved that graphene as a nanoadsorbent has offered potential benefits for various pollutants [53-56]. However, some important aspects of the use of graphene as adsorbent need to be considered. Graphene cannot be easily collected or separated from water after batch experiments, leading to recontamination or nanotoxicity, which eventually results additional problems to the ecosystem [57]. Again, graphene as a bulk material in solution phase has the tendency to agglomerate and restack due to strong van der Waals interactions to form graphite and results in large drop in the surface area and hence the adsorption capability [57]. To mitigate these problems various functionalization schemes of graphene have been explored in the literature. Among the chemically functionalized graphene, graphene oxide (GO), a highly oxidized form of graphene with functional groups decorated all over the sheets such as carboxyl (-COOH) and carbonyl (-C=O) groups at the sheet edges, and epoxy (C-O-C) and hydroxyl (-OH) groups on the basal plane [58]. Its oxygen containing functional groups and extremely high surface area favour its applications in the field of water decontamination. Several research groups have reported the beneficial uses of GO as an excellent adsorbent material for the removal of heavy metal ions, dye molecules and others cationic compounds [59-64].

Lei et al. [59] used three-dimensional free-standing graphene oxide foam (GOF) for the removal of heavy metal ions. Its adsorption capacity for the removal of heavy metal ions demonstrated that GOF had superior adsorption ability and good recyclability towards a wide range of metals ions, such as Zn^{2+}, Fe^{3+}, Pb^{2+}, and Cd^{2+}. GOF was prepared by direct oxidation of graphene foam, synthesized by microwave plasma chemical vapor deposition. The GOF processed a very high surface area (578.4 m^2 g^{-1}) and abundant oxygen functional groups with a rather low C/O ratio of 0.65. The maximum adsorption capacities found were 252.5, 326.4, 381.3, and 587 mg g^{-1} for Cd^{2+}, Zn^{2+}, Pb^{2+} and Fe^{3+}, respectively. The experimental data agreed well with the Langmuir isotherm adsorption model with 85% of the maximum adsorption capacities.

Zhao et al. [60] synthesized fewlayered graphene oxide (FLGO) nanosheets from graphite using the modified Hummers method, and used as sorbents for the removal of Cd(II) and Co(II) ions from large volumes of aqueous solutions. The abundant oxygen-containing functional groups on the surfaces of graphene oxide nanosheets played a significant role in the adsorption of Cd(II) and Co(II). The effects of pH, ionic strength, and humic acid on Cd(II) and Co(II) sorption were investigated. The results showed that Cd(II) and Co(II) sorption on the FLGO nanosheets was strongly dependent on pH and weakly dependent on ionic strength. The presence of humic acid (HA) reduced Cd(II) and Co(II) sorption on graphene oxide nanosheets at pH < 8. Although the surface site density of graphene oxide nanosheets is lower than that of HA, the strong interaction of HA with graphene oxide nanosheets occupies parts of surface sites on graphene oxide nanosheets and also reduces the available binding sites of HA, leading to the formation of $Co(OH)_2$ precipitation at pH > 8.2. The maximum sorption capacities of Cd(II) and Co(II) on graphene oxide nanosheets at pH 6.0 and 303 K were found about 106.3 and 68.2 mg g^{-1} respectively. The thermodynamic parameters calculated from temperature-dependent sorption isotherms suggested that Cd(II) and Co(II) sorption on graphene oxide nanosheets were endothermic and spontaneous processes.

Yang et al. [61] have studied the adsorption kinetics, isotherms and thermodynamics of Cr(III) on graphene oxide (GO). The adsorption kinetic data and the equilibrium data were well described by pseudo-second-order kinetics and Langmuir model, respectively. The thermodynamic parameters calculation indicated that the adsorption of Cr(III) on GO was spontaneous and endothermic. The maximum adsorption capacity of Cr(III) on GO at pH 5.0 and T = 296 K was about 92.65 mg g^{-1} with a strong dependence on solution pH, but weak dependence on ionic strength. Fourier transform infrared (FTIR) spectra suggested that Cr(III) was adsorbed on GO mainly through the formation of inner-sphere complexes with the O-containing functional groups on GO surface. *Ramesha et al.* [62] studied the adsorption of various charged dyes such as methylene blue (MB), methyl violet (MV), rhodamine B (RB), and orange G (OG) from aqueous solutions by exfoliated graphene oxide (EGO) and reduced graphene oxide (rGO). EGO consists of single layer of graphite decorated with oxygen containing functional groups such as carboxyl, epoxy, ketone, and hydroxyl groups in its basal and edge planes. Consequently, the large negative charge density available in aqueous solutions helps in the effective adsorption of cationic dyes on EGO with efficiency of up to 95% for cationic dyes while the adsorption was negligible for anionic dyes. On the other hand, rGO that has high surface area does not possess high negative charge and was found to be very good adsorbent with removal efficiency 95% for anionic dyes, and 50% for cationic dyes. The adsorption can be attributed to the electrostatic interaction of nitrogen (ammonium ion) of MV with the COO^- group of EGO. The delocalization of electrons in MV may influence the interaction and the charge transfer may not be strong. The nature of amine group (secondary amine) and possibly the steric hindrance limits the extent of interaction with EGO. With EGO/RB system, there is perhaps weak van der Waals and electrostatic interactions, and between EGO and OG, it is possibly van der Waals interactions alone. Electrostatic interactions play a role with EGO/MV and EGO/MB, while it is only van der Waals interaction with EGO/OG. The interactions with EGO/RB are probably both electrostatic and van der Waals type. According to the literature discussed, GO showed promising adsorption behaviors for water decontamination. However, GO has poor affinity for acidic/anionic compounds due to strong electrostatic repulsion between negative functional groups of GO and negative charge

on adsorbents leading to weak adsorption capacity [62]. Also, collection or separation of GO after adsorption is a serious problem. Moreover, unprecipitated feature of GO may cause a potential nano-toxicity to aquatic creatures, leading to a serious recontamination.

Functionalization of graphene oxide has been explored by many research groups [57, 65, 66]. It may be achieved by the carboxylic acid group of graphene oxide or at the epoxy group of graphene oxide or non-covalent functionalization of graphene oxide or functionalization of reduced graphene oxide [58]. It improved their interactions with pollutants and maximized adsorption performance and potential.

Wang et al. [67] reviewed the novel use of graphene based nanomaterials for remediation of various pollutants that may be inorganic and organic compounds from water. The physiochemical properties of GO were discussed with its limitations, especially in the field of water decontamination. Modification of graphene oxide or graphene with metal oxides or organics were considered to enhance adsorption capacity, separation efficiency, and better reusability. *Kui et al.* [68] also reported graphene-based nanomaterials including modified graphene, graphene/metal nanoparticle composites, graphene/semiconductor hybrids, and graphene-complex oxide composites for better pollution management than pristine graphene. *Perreault et al.* [69] also highlighted graphene-based materials for environmental applications. They reviewed the recent developments using graphene-based materials as an adsorbent as well as its photocatalytic activities for environmental decontamination.

GO has strong mechanical properties, its sheets help as a building frame increasing the mechanical properties of porous materials. *Zhang et al.* [70] prepared a porous Chitosan–gelatin/Graphene oxide (CGGO) monoliths with 97% porosity by a unidirectional freeze-drying method for the use of metal ions adsoption, such as Cu^{2+} or Pb^{2+} adsorption. All the CGGO monoliths exhibited extraordinarily high water absorption abilities, which should facilitate the diffusion of metal ions to the surface and interior regions of the porous structures. The adsorption behavior of the CGGO monoliths and influencing factors such as pH, GO concentration, metal ion concentration as well as the effect of EDTA were investigated. The incorporation of GO significantly increased the compressive strength of the CGGO monoliths

in both their wet and dry states, changed their porous structure with decent dimensional stability in aqueous solutions. The adsorbing ability for metal ions decreased at low pH, but increased from 20% to 88% upon the addition of EDTA at low pH. The remarkable increase in adsorption was mainly due to the high porosity of the CGGO monoliths, and the electrostatic interactions between the Cu^{2+}–EDTA complexes and the protonated amino groups on the backbone of the chitosan macromolecules. Because of the high porosity of the CGGO monoliths, a large number of protonated amino groups are exposed to the solution. Since Cu^{2+}–EDTA complexes exhibit anionic properties, they can be easily attached by the exposed protonated amino groups through electrostatic interactions.

The recent advances in graphene based materials largely include the anchoring of metal oxide nanoparticles into graphene/graphene oxide sheets. There are number of literature reported in a review article by *Upadhyay et al.* [71] using GO/metal oxide composites for water treatment, in which the authors have suggested all possible interactions GO/metal oxide composites. Another review paper by *Hua et al.* [72] described the heavy metal removal from wastewater by numbers of nanosized metal oxides, including ferric oxides, manganese oxides, aluminum oxides, titanium oxides, magnesium oxides, and cerium oxides. The adsorption efficiencies for all of the oxides were measured by varying experimental parameters. They mainly focused on their preparation method, physicochemical properties, and adsorption mechanism for heavy metal removal. Also, porous and magnetic nanomaterials got special attention in some section due to their unique separation performance.

Nanotoxicity in water is a serious cause due to separation problem of graphene/graphene oxide from treated water. This can be controlled by incorporation of substances having magnetic properties so that magnetic separation can be possible. *Li et al.* [73] have functionalized GO with magnetic cyclodextrin-chitosan for chromium(VI) removal. The prepared material showed excellent adsorption behavior as a result of high specific surface area, sufficient binding sites (hydroxyl and amino groups), and their surface charge concentration, the additional effect of magnetite nanoparticles added extra adsorption properties. The novel

adsorption capacity of the material exhibited Langmuir isotherm at low pH for hexavalent chromium removal.

2.2. Magnetite as an Adsorbent

Among all pronounced magnetic materials, magnetite (Fe_3O_4) is the oldest and is one of the best magnetic material on earth [74, 75]. Magnetite nanoparticles also have contributed a lot in water decontamination due to the relative ease of synthesizing uniform nano sized particles with high surface area. These are well dispersed in water and are benign to the ecosystem [76-78]. Magnetite nanoparticles show superparamagnetic behavior at room temperature with high saturation magnetization so that it can perform best in magnetic separation process [78]. There are numbers of published literature, where magnetite as nanoadsorbent has been used widely for dyes as well as toxic heavy ions removal. *Shen et al.* [79] have prepared magnetic Fe_3O_4 nanoparticles by (i) co-precipitation method, (ii) co-precipitation followed by surface decoration, and (iii) polyol process showing three different average particle sizes of 8 nm, 12 nm, and 35 nm respectively. They used synthesized Fe_3O_4 nanoparticles for removal of heavy metal ions such as Cu(II), Ni(II), Cd(II) and Cr(VI) mainly followed mechanism of electrostatic attraction. A special attention to particle size have been studied to investigate the adsorption capacity of magnetite nanoparticles showing increased adsorption with decreasing the particle size. Various process parameters (pH, temperature, adsorbent dose, contact time) for the smallest (8 nm) particles were optimized and used for all four kinds of ions. The maximum adsorption capacity was found to be 35.46 mg g^{-1} at pH-4, 293 K, six times higher value as compare to coarse particles (low surface area). They concluded that the magnetite nanoparticles with <10 nm sized were convenient for the removal of toxic ions with a maximum adsorption capacity of 41.86 mg g^{-1} for Ni^{2+}, 47.44 mg g^{-1} for Cu^{2+}, 45. 86 mg g^{-1} for Cd^{2+}, and 43.59 mg g^{-1} for Cr^{6+}.

Yuan et al. [80] have prepared diatomite-supported/unsupported magnetite nanoparticles using co-precipitation and hydrosol methods for hexavalent chromium removal. The prepared diatomite-supported magnetite nanoparticles by hydrosol method were found to be of 15 nm size, good dispersion, less aggregation, and high thermal stability, with excellent adsorption

behavior. The interaction of Cr(VI) was described by a physico-chemical process such as an electrostatic attraction followed by a reduction of Cr(VI) to Cr(III). They studied pH dependence study on adsorption of Cr(VI), the kinetics studies showing a pseudo-second-order rate. The isotherm studies for both diatomite-supported/unsupported magnetite fitted well to the Langmuir isotherm equation. The maximum adsorption capacity obtained from the Langmuir equation followed order of 69.2 mg g^{-1} > 21.7 mg g^{-1} > 14.6 mg g^{-1} for diatomite-supported/unsupported nano-scaled magnetite and micron-scaled magnetite respectively.

Nano sized magnetite rods have been used by *Karami* [81] for Fe(II), Pb(II), Zn(II), Ni(II), Cd(II) and Cu(II) from aqueous solution. The pulsed current electrochemical method was used synthesize magnetite nanorods of 60 nm average diameters and 1000 nm average lengths showing excellent quantitative adsorption behavior. The experimental data exhibited that the adsorption of heavy metal ions onto magnetite nanorods followed Langmuir isotherm model and pseudo-second order kinetics. The maximum adsorption capacities of magnetite nano-adsorbents calculated from the Langmuir isotherm models for Fe^{2+}, Pb^{2+}, Zn^{2+}, Ni^{2+}, $Cd^{2+}$and Cu^{2+} were 127.01,112.86, 107.27, 95.42, 88.39 and 79.10 mg g^{-1} respectively. The regeneration of the nanorods was achieved by acid leaching with a cost effective eluent, HNO_3 (nitric acid) solution.

Saha et al. [82] have reported adsorption of different types of dyes (erichrome black-T, bromophenol blue, bromocresol green, methyl red, methylene blue, methyl orange, and fluorescein) onto iron oxide nanoparticles, and also demonstrated a comparative study between dyes containing -OH groups and without -OH groups. The synthesized iron oxide nanoparticles by co-precipitation method possessed 20-40 nm average size and ~70 m^2 g^{-1} specific surface area, and showed ferromagnetic behavior, both at room and low temperature, which helped for magnetic separation. The group of dyes (erichrome black-T, bromophenol blue, bromocresol green and fluorescein) containing especially hydroxyl groups showed enhanced adsorption capacity on the iron oxide surface as compared those that didn't have -OH groups. The kinetic studies of dyes with hydroxyl groups indicated a faster second order rate in the pH range of 4

to 5. The adsorption equilibrium data exhibited interesting multilayer isotherm, well fitted to Freundlich model. The weak interactions (physisorption) of these dyes with iron oxide surface were evaluated from the Dubinin-Raduskevich isotherm model. The optimum pH for complete desorption was achieved at highly alkaline pH (> 11) with efficient reusability property.

2.3. GO-Fe_3O_4 Hybrids as Adsorbents

From the above cited literature, magnetite nanoparticles appear to be low cost, and eco-friendly adsorbent for wastewater treatment, owing to their high surface area, easy magnetic separation process, shorter sedimentation time, no sludge formation, and easily recycling back into the process [76-79, 81-83]. However, bare magnetite nanoparticles are susceptible to air oxidation and possess poor thermodynamic stability. Their further oxidation to other forms of the oxide, including maghemite (γ-Fe_2O_3) and hematite (α-Fe_2O_3), is proving to be a major hurdle for field application [34]. Additionally, due to a strong magnetic dipole, magnetite particles tend to aggregate in aqueous systems [84, 85]. The incorporation of engineered magnetite particles into GO based planar (2-dimensional) materials can mitigate the individual drawbacks of both GO and magnetite, and the synthesis of a hybrid of these materials can combine advantages of both of the materials. Graphene oxide, due to the presence of hydrophilic functional groups, can stay dispersed in aqueous systems, and can prevent restacking of the graphene sheets, unlike pure graphene. Therefore, GO can be used as template, or substrate, where magnetite nanoparticles can form a nucleus and growth to the required size. Thus, the magnetic nanoparticles being anchored to the GO surface can enhance and sustain a specific surface area of the hybrid during water treatment process. Various literature that have used the said or related concepts are reviewed in the next section.

Yang et al. [86] have studied the interactions and adsorption performance of the organic (1-naphthol and 1-naphthylamine) and inorganic pollutants (Pb^{2+}) with synthesized GO-iron oxide and rGO-iron oxide composites using GO or rGO (reduced graphene oxide) as substrates, respectively. The comparative studies showed that the GO-iron oxide composite performs better for Pb(II) than organic pollutants due to complexation interaction and electrostatic attraction of inorganic metal ion with the negative oxygen-containing functional groups on GO. The data indicated q_{max} value of GO-iron oxides and RGO-iron oxides as 588.24 and 454.55

mg g^{-1}, respectively. Also, adsorption capacities of naphthylamine on GO-iron oxides and RGO-iron oxides were calculated to be 285.7 and 303.03 mg g^{-1}, respectively, concluding better performance of rGO-iron oxides.

Adsorption of Cd(II) and ionic dyes was studied by *Deng et al.* [87]. The potential adsorption of magnetic graphene oxide (MGO) was simultaneously used for Cd(II), methylene blue (MB) and orange G (OG). The results showed the maximum sorption capacities in ultrapure water for Cd(II), MB and OG were 91.29 mg g^{-1}, 64.23 mg g^{-1} and 20.85 mg g^{-1}, respectively, and confirmed to pseudo-second-order kinetic model. The effect of adsorption capacities of Cd(II) in presence of MB and vice-versa were briefly studied by Cd(II)–MB binary system. However, in the same way, sorption capacity of OG in presence of Cd(II) and Cd(II) in presence of OG was studied in Cd(II)–OG binary system. The increase in solution pH for Cd(II) and MB system increase the sorption capacities, however, showed a contrary behavior for OG.

Nano-sized [44-47, 51, 52] magnetite/graphene oxide (M/GO) composite was developed by *Liu et al.* [88] for the removal of Co(II) from aqueous solutions. The sorption of Co(II) on the magnetite-GO composite as a function of various process parameters were investigated. The adsorption data followed Langmuir isotherm model and pseudo-second-order kinetics. Thermodynamic parameters indicated endothermic process, and adsorption was spontaneous for the temperature range studied. The maximum adsorption capacities of Co(II) calculated from Langmuir isotherm model were 12.98 mg g^{-1} for the composites and a small value of 6.2 mg g^{-1} for bare magnetite particles. The results indicated that the adsorption capacity of Co(II) on the Fe_3O_4-GO composite is much higher than that of Co(II) on Fe_3O_4. The inner-sphere surface complexation of Co(II) on Fe_3O_4-GO was observed at low pH. However, higher pH led to precipitation. The easy magnetic separation and recovery process proved the composite material to be suitable for metal ions decontamination from water in the natural environment.

2.4. Cr(VI) As a Toxin and its Removal

Industrial discharge bears lots of heavy metal ions among which most hazardous are Cd, Cr, Cu, Ni, As, Pb, and Zn. These ions are non-biodegradable inorganic pollutants that accumulate in living beings causing serious carcinogenic effects. Further, these ions are highly soluble in

aqueous systems and get easily absorbed in the food chain polluting the whole living system [89], although essential for human living process when present at trace levels. But, when the presence of these ions exceeds the critical/permissible limits, severe carcinogenic concerns arise. Among the heavy metal ions, chromium is one of the most hazardous. It is the 21st most abundant metal in natural earth crust existing in a wide range of oxidation states of +1 to +6, where +3 and +6 are most commonly occurring states. Among +3 and +6 oxidation states, +6 is more toxic, stable, and exists as either in the form of chromate (CrO_4^{2-}), dichromate ($Cr_2O_7^{2-}$), or hydrochromate ($HCrO_4^-$) ions [90].

The primary sources of chromium discharge are corrosion of natural elemental rocks and dust from volcanic eruption. The main and major source of chromium is industrial or anthropogenic activities; including the direct or indirect discharge of effluents of chrome plating, stain-less steel production, and manufacturing of photographic plates from various industries. Chromium (VI and III) exposure can happen by both volatile and non-volatile forms causing various skin diseases and lung carcinoma [91]. It goes into human body by simple breathing, consumption of contaminated food and drinking contaminated water. Direct or indirect contact with skin can also cause primary skin irritation. Therefore, a maximum permissible limit hexavalent chromium has been set as a value of 0.05 mg L^{-1} by USEPA (2011). ATSDR (2000) found excess ingestion and exposure to hexavalent chromium beyond permissible limit can cause diarrhea, gastrointestinal disorders, irritation in the mucous membrane, low blood platelets, headache, damaged RBC, asthma, chest pain, and vomiting.

Many adsorbent materials have been developed having selective properties, especially for the removal of hexavalent chromium from waste water. *Pradhan et al*. [92] studied the uptake of hexavalent chromium by activating red mud, an industrial waste. They suggested the heterogeneous adsorption behavior of adsorbent surface show both Langmuir as well as Freundlich adsorption isotherm models. Prominent effect of temperature, foreign ions and initial chromium concentration on adsorption behavior were investigated. Among all foreign ions sulfate (SO_4^{-2}), and phosphate (PO_4^{-3}) had perceptible effects on chromium adsorption. The optimum conditions for maximum adsorption found were pH in the range of 5 at 303 K, with initial chromium concentration 2-30 mg L^{-1}. The maximum adsorption capacity was

calculated to be 30.74 mmol g^{-1}. *Deng et al.* [93] used fiber material for removal of trivalent and hexavalent chromium. Polyacrylonitrile fibers were tested as a function of pH and found that adsorption performance was greatly dependent on solution pH. Adsorption of trivalent chromium occurred completely through surface complexation or chelating interaction of nitrogen containing surface group and Cr(III). However, the hexavalent chromium bound through hydrogen bonding or electrostatic attraction depending on pH of the solution. The mechanism of adsorption was analyzed by X-ray photoelectron spectroscopy (XPS) and FTIR spectra after adsorption of toxic ions. Adsorption of hexavalent chromium was found up to a maximum of 96%. The regeneration of both Cr(VI) and Cr(III) loaded fibers were done by base and acid leaching, respectively, without loss of adsorption capacities. *Ow lad et al.* [94] have published a review article on Cr(VI) removal from waste water mainly focusing on adsorption, as well as some typical methods including membrane filtration, ion exchange, and electrochemical treatment methods. Adsorption was found to be promising and new technique widely used to overcome water contamination. Different types of adsorbent materials, such as activated carbons (that possess high specific surface area), chitosan polymer (highly hydrophilic and flexible with surface amino groups), and inorganic membranes with high chemical and thermal stability were discussed. Biosorption using some low cost biosorbent followed by chemical modifications to get better performance were also discussed.

Grandos-Correa et al. [95] used synthesized boehmite as adsorbent material for hexavalent chromium removal. Effect of various process parameters on chromium adsorption, isotherm, thermodynamic and kinetic studies were performed in order to get the adsorption mechanism at optimum conditions. Thermodynamic parameters suggested that adsorption is endothermic and spontaneous. Freundlich, Langmuir and Dubinin–Radushkevich isotherm models were studied to understand the equilibrium adsorption process. Overall boehmite was found to be a potential adsorbent for chromium removal. Another modified adsorbent, a mixed hydroxide of aluminum and magnesium were prepared by *Li at al.* [96] in nano sized range for Cr(VI) removal. Different Mg/Al molar ratios were synthesized by co precipitation and tested. It was found that molar ratio 3 (Mg/Al) showed maximum adsorption efficiency because of the smallest average particle size and high zeta potential value. Adsorption of Cr(VI) was favorable

at alkaline medium with a greater reaction rate. The interaction mechanism was attributed to a combination of both anion exchange and surface complexation. The maximum adsorption capacity was found to be in the range of 105.3-112.0 mg g^{-1} at temperature ranges from 20-40 ^{o}C. The adsorption experiment was endothermic and followed pseudo-second-order kinetics.

Later *Gupta et al.* [97] have also used a low cost fertilizer from industrial waste for uptake of Cr(VI). They converted carbon slurry, an industrial waste generated in generators of fuel oil-based industries, into a practically applicable adsorbent for hexavalent chromium removal from contaminated water. The raw material was oxidized with hydrogen peroxide and then acid activated with HCl to increase active surface area. Various adsorption conditions were applied with respect to adsorption efficiency. The equilibrium parameters for maximum adsorption were found at 70 min of digestion time, solution of pH-2, 100 mg L^{-1} initial Cr(VI) concentration, 4.0 g L^{-1} adsorbent dose, and 303 K temperature. Both Langmuir and Freundlich adsorption isotherm models were applicable to the adsorption behavior, and the kinetics followed pseudo-second order rate model. Maximum adsorption capacity was calculated as 15.24 mg g^{-1} for Cr(VI) removal on activated carbon slurry. Regeneration of the adsorbent was proposed by column study.

In the previous literature survey chitosan polymer were proved to be suitable adsorbent material for hexavalent chromium [94]. *Sufia Hena* [98] prepared a modified form of chitosan biopolymer coated with poly-3-methyl thiophene polymer. This surface functionalization was performed to achieve maximum adsorption capacity of the biopolymer than other commercially available activated carbon and adsorbents reported in other literatures [98-109]. Langmuir isotherm model better fitted the adsorption mechanism of chitosan coated with poly-3-methyl thiophene than Freundlich of Temkin isotherm models in the optimum temperature range. The maximum adsorption capacity was found to be 127.62 mg g^{-1}, which is a greater value than reported literature.

Both biopolymer and ionic liquid have been gathered considerable attention in the field of adsorption applications. *Kumar et al.* [110] have analyzed the active adsorption of chromium(VI) using a chitosan biopolymer impregnated with tetraoctylammonium bromide

by ultrasonication. The coupling mechanism of chitosan and ionic liquid was governed by effective mass transfer due to ultrasonication followed by hydrogen bonding between chitosan-ionic liquid. The adsorption mechanism was facilitated by electrostatic interaction between amino groups in chitosan and Cr(VI) through three center (3c) co-operative mechanism. The Langmuir adsorption capacity of chromium onto prepared adsorbent was 63.69 mg g^{-1}. Adsorption accompanied pseudo second order kinetics and exothermic spontaneous adsorption process.

Graphene based material also have been used in recent years showing excellent adsorption efficacy towards carcinogenic metal ions. *Wu et al.* [111] used a modified form of graphene with cetyltrimethylammonium bromide as an active adsorbent. The results from batch experiment suggested the maximum uptake happened at lower pH value. The equilibrium temperature was at 293 K showing exothermic and spontaneous behavior. The adsorption processes were very fast and fitted well to pseudo-second-order model. The maximum Langmuir adsorption capacity was 21.57 mg g^{-1} at optimum temperature value. *Kumar et al.* [112] have reported exfoliated graphene oxide modified with an ionic liquid (aliquat-336) as an adsorbent to get a combined effect of hexavalent chromium removal. Graphene oxide worked as an impregnating platform for ionic liquid through electrostatic interaction mechanism. The adsorption mechanism of hydrochromate anion, the dominant complex form of hexavalent chromium in the optimum pH range, interacted with the prepared hybrid by cation-π, anion-π, as well as electrostatic interactions. The process followed second order kinetics and the Langmuir adsorption capacity was 285.71 mg g^{-1}. Regeneration of the adsorbent could be possible with ammonium hydroxide, which leached out hexavalent chromium as ammonium chromate complex.

The main sources of dye pollutions are from textile, paper and food processing industries releasing untreated water in to river and water reservoir. These dyes are water soluble, non-biodegradable, but can be decomposed into poisonous aromatic amines that may cause ill health effect to living beings. Even a very low concentration of dye (< 1 ppm) in water is considered problematic for human use. These complex structured dyes can hamper the cycles of aquatic ecosystem too by slowing down the photosynthesis process of green plants. These

dyes do not allow the penetration of light and reach the aquatic plants [113, 114]. Some of it also affect the catalytic activities of microorganism [115].

Therefore, direct disposal of waste containing dyes should be restricted and must be treated before releasing. Some of the above literatures suggest that adsorption is a promising method for dyes removal and that various adsorbent materials have been tried for different kinds of dyes. In the following sections, two specific dyes mostly found in industrial wastes, named malachite green and phenol red, will be discussed.

2.5. Malachite Green as a Toxin and its Removal

Malachite green (MG) is a cationic dye also known as triarylmethane. The primary sources of malachite green are mainly leather dying, ceramic, and fertilizer industries. It has a complex structure (**Figure.2.1**) containing nitrogen groups. MG was categorized as hazardous dye by WHO in 1964 and found to be carcinogenic or mutagenic [116, 117]. Malachite green is highly soluble in water and can harm the aquatic system, render the penetration of UV light into water bodies. Its health effects include damage to the liver, gill, kidney, and intestine of living characters in aquatic system [118, 119]. In case of human beings, even inhalation, ingestion, or contact can cause extreme irritation, and may cause permanent injury to eyes.

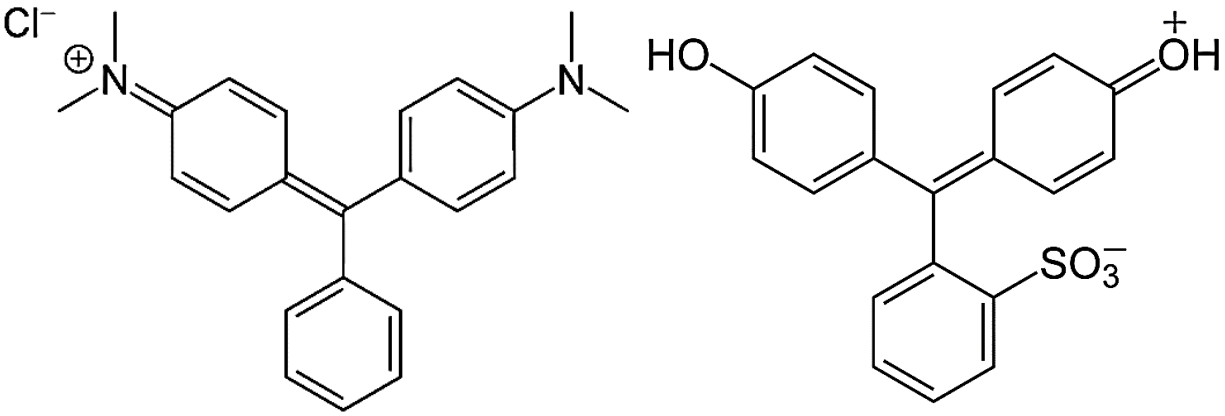

Figure.2.1. The molecular structure of malachite green (left) and phenol red (right).

Keeping the hazardous effect of malachite green in mind different types of adsorbent materials have been synthesized by many researchers for potential adsorption of MG from waste water. A number of low cost adsorbents have been developed for uptake of malachite green. *Chowdhury et al.* [119] have chemically modified rice husk by treating it with sodium hydroxide and used in batch experiments. The adsorption of malachite green followed Freundlich isotherm model. Chemical ion-exchange was the main mechanism with maximum adsorption capacity was 7.395 mg g^{-1} at 313 K. Adsorption of malachite green onto modified rice husk was endothermic and followed pseudo-second order kinetics. *Khattri et al.* [120] used neem saw dust as an adsorbent, and found monolayer adsorption of MG dye with Langmuir maximum adsorption capacity of 4.354 mg g^{-1}. *Vasanth Kumar et al.* [121] used pithophora sp., a water algae for malachite green adsorption. This water alga performed maximum when activated at 300 °C for 50 min for 20-100 mg L^{-1} dye concentration. It followed Redlich-Peterson isotherm model with maximum sorption capacity 117.647 mg g^{-1}. *Gupta et al. [122]* used another low cost adsorbent called bottom ash, a thermal power plant waste. Almost 100% of malachite green was adsorbent by bottom ash. Langmuir and Freundlich adsorption isotherm models were analyzed. Acetone was used as eluent for the recovery of adsorbent bed. *Ahmad et al.* [123] have studied ginger waste for adsorption of malachite green through batch and column methods. Rechienberg's equation was used to understand the complete film diffusion of adsorption. Alkaline medium was found favorable for maximum adsorption with monolayer adsorption capacities 84.03, 163.9 and 188.6 mg g^{-1} at 30, 40 and 50 °C respectively. *Onal et al.* [124] used activated carbon prepared from lignite by chemical activation with potassium hydroxide. They produced activated carbon which possessed high specific surface area (1000 $m^2 g^{-1}$), and behaved as a good adsorbent for malachite green. Mass transfer and pore diffusion were found to be the governing mechanisms for the diffusion of MG. The process was endothermic in nature. The use of many other types of adsorbent materials have been tested in the literature with low to moderate adsorption capacity, including mesoporous carbons [125], activated carbon prepared from the epicarp of ricinus communis [126], rice husk-based porous carbon [127], rice husk-based active carbon [128], activated carbon derived from borassus

aethiopum [129], silica gel [130], rice straw-derived char [131], bentonite [132], Activated carbon/$CoFe_2O_4$ composites [133], and chitosan bead [134].

Graphene materials also have been attended as potential adsorbent material for malachite green. *Bradder et al.* [135] have studied layered graphene oxide prepared by modified Hummers method. Layered GO that contains large numbers of oxygen containing functional groups with a high surface area showed better adsorption behavior than graphite. The Langmuir maximum adsorption capacity was 351 mg g^{-1} and 248 mg g^{-1}, respectively, for methylene blue and malachite green.

Zhigang Geng et al. [136] have functionalized reduced graphene oxide–Fe_3O_4 nanoparticles a composite material for dye adsorption. A series of dyes, including Rhodamine 6G (R6G), acid blue 92 (AB92), orange (OII), malachite green (MG), and new coccine (NC) have been used as adsorbate. The mechanisms of adsorption of dyes were mainly ascribed through π-π conjugation. The magnetic property of Fe_3O_4 helped the composite material to be separated from solution through magnetic separation. The hybrid material was regenerated successfully for reuse. Graphene oxide–Fe_3O_4 materials possessed numerous advantages, such as low cost, easy processing, combine adsorption performance of both GO and iron oxide, good regeneration capacity.

2.6. Phenol Red as a Toxin and its Removal

Dyes containing industrial waste also majorly contain phenol red (PR). It is also one of the most toxic dyes to both human beings and animals. In aqueous solutions containing PR, photocatalytic degradation, microbial decomposition and chemical oxidation are difficult due to the dye's complex aromatic structure [137]. Phenol red induces cytotoxicity to Hela cells during tissue culture [138], and is considered a serious threat to living organisms. Therefore, removal of phenol red is a major concern and thus, there is a need to establish conventional, cost efficient and practically applicable technologies for removal of such carcinogenic materials from water. Some of the literature related to adsorption of phenol red from contaminated water are discussed below.

Mittal et al. [97] suggested adsorption, a conventional removal method for phenol red using different types of waste material. Their main motivation of that research work was use of waste as an adsorbent for wastewater treatment. They used bottom ash, a thermal power plants waste and deoiled soya, an agricultural waste material as effective adsorbents. Equilibrium studies were performed and monolayered adsorption with a maximum of 2.6×10^{-5} mol g^{-1} capacity. Thermodynamic calculations indicated that the process was endothermic, and followed inter particle and film diffusion mechanisms. Almost 90% regeneration was achieved by acid leaching. *Iqbal et al.* [139] studied the adsorption of dyes by activated charcoal. They had taken a number of industrially important dyes, where phenol red was one of them. Adsorption performance of activated charcoal was investigated individually and also for a mixture of dyes that showed L-type and S-type isotherms. In case of mixture of dyes, the dye–dye interaction dominates over adsorbent and dyes attraction. Effect of pH on adsorption concluded that increase in pH can increase the adsorption for cationic dyes. However, for phenol red, the adsorption efficiency decreased with increasing pH. The negative values of Gibb's free energy and enthalpy change for phenol red revealed that adsorption was exothermic and spontaneous. The maximum Langmuir capacity for phenol red was 0.0409 mg g^{-1} at 298 K.

Wu et al. [140] have used mesoporous silica and hybrid gels for organic dyes like alizarin red S and phenol red adsorption. The comparative studies for both adsorbents demonstrated the hybrid gels to have more adsorption capacity than silica gel. They suggested that the adsorption mechanism of organic dyes are governed by interaction of hydrophobic gel surface and dye molecules. Toth isotherm (heterogeneity in adsorption behavior) showed better regression as compared to Langmuir isotherm. *Wu* [141] with another group of researchers investigated the adsorption study of organic dyes (methyl orange, alizarin red S, brilliant blue FCF, and phenol red) by porous xerogels. Here also, the mechanism of adsorption was the hydrophobic interaction of gel surface with organic dyes. Hybrid xerogels performed better than untemplated xerogels. Electrostatic interactions (hydrogen bonding) of xerogel surface and dye molecules effected by pH change, but was not found as a dominant mechanism.

OBJECTIVES

The main objectives of the research work produced here are:

- To synthesize nano-structured magnetite particles Fe_3O_4 by a facile sonication assisted chemical co-precipitation method.
- To perform Cr(VI) removal test for bare magnetite system by batch experiments and study the effect of various process parameters including adsorbent doses, pH, contact time and initial adsorbate concentration, on adsorption.
- To synthesize graphene oxide(GO) by modified Hummer's method.
- Anchoring of Fe_3O_4 nanoparticles into GO sheets to synthesize GO-Fe_3O_4 hybrids materials by a facile and straight forward wet chemical route with enhanced surface area and phase stability.
- To study the removal kinetics of Cr(VI) ions on GO-Fe_3O_4 hybrids as the adsorbent system and explore the effect of various process parameters including adsorbent doses, pH, contact time and initial adsorbate concentration, on adsorption.
- To test the removal efficiency of malachite green, a form of cationic dye with the use of GO-Fe_3O_4 hybrid adsorbents and study the effect of adsorbent doses, pH, contact time and initial adsorbate concentration, on adsorption.
- To test the removal of efficiency phenol red (PR), a form of neutral dye, with the use of GO-Fe_3O_4 hybrid adsorbents and study the effect of various process parameters such as adsorbent doses, pH, contact time and initial adsorbate concentration, on its adsorption process.
- To understand the isotherms and kinetics of adsorption for all of the toxin/adsorbent systems, corroboration of the experimental data to various mathematical models.

CHAPTER-3

EXPERIMENTAL DETAILS

In this section, details of materials synthesis, and procedures for adsorption studies are presented. First, the synthesis of magnetite nanoparticles is shown, followed by the synthesis of graphene oxide from modified Hummer's method. Subsequently, the processing of the GO-Fe_3O_4 hybrid adsorbents is performed. Adsorption studies are detailed thereafter. Some theoretical aspects of the adsorption kinetics and isotherm modeling are also presented.

3.1. Experimental Details: Materials Synthesis and Characterization

3.1.1. Chemicals and Materials

The qualities of reagents were pure and of analytical grade. Water was deionized prior to use for the dilution of aqueous solutions. $FeCl_3$ $6H_2O$ and $FeCl_2$ $4H_2O$ were procured from Loba Chemie, India. Graphite and all other chemicals including H_2SO_4, $NaNO_3$, $KMnO_4$ and H_2O_2 were purchased from Merck, India. A working solution of 100 mg L^{-1} Cr(VI) for batch adsorption experiments was prepared from stock 1000 mg L^{-1} Cr(VI) using $K_2Cr_2O_7$ (Merck). Diphenyl carbazide reagent was used for spectrophotometric determination of chromium in the aqueous. Dyes (malachite Green, phenol Red) were obtained from Sigma-Aldrich, India. The pH of the solution was maintained by the addition of required amount of 0.1M HCl (Merck) and 0.1M NaOH (Merck). All glassware used for experimental purposes were acid-washed and subsequently rinsed with deionized (DI) water to avoid metal contamination. All of the materials were used without further purification.

3.1.2. Preparation of Magnetite Nanoparticles

Ferrous chloride tetrahydrate ($FeCl_2$ $4H_2O$) (Loba Chemie, India) and Ferric chloride hexahydrate ($FeCl_3$ $6H_2O$) (Loba Chemie, India) were used as the precursors. Aqueous solutions of ferric and ferrous salts were mixed together in the ratio of 1:2. The mixture was heated with continuous stirring, then ammonia (NH_3) (AR grade, Merck) in water was added to it as a precipitating agent. A brown colored precipitate of Fe^{2+}/Fe^{3+} ions was formed which is subjected to horn ultra-sonication (Oscar Ultrasonics, Mumbai) for 30 mins. Then the solution was cooled to room temperature, washed several times with deionized water to remove excess ammonium and dried under vacuum at 70 ˚C.

3.1.3. Synthesis of graphene oxide (GO)

Graphene oxide was synthesized from natural graphite by a modified Hummers method from the natural flake Graphite (Merck). 69 ml. of H_2SO_4 (Merck) was added to 3 g. graphite powder and 1.5 g. $NaNO_3$ (Merck). Then the mixture was cooled in an ice bath. 9 g. of $KMnO_4$ (Merck),

an oxidizing agent was gradually added while stirring. The rate of addition was carefully controlled to keep the reaction temperature below 20 ˚C. Subsequently, the reaction mixture was diluted with distilled water in an ice bath where the temperature was rapidly increased to 98 ˚C. The suspension was stirred at 98 ˚C for 1 day. 3 ml. H_2O_2 (Merck) was then added to the mixture. The resulting suspension was heated, and then air cooled. The solid GO was obtained after the black deposit was filtered followed by centrifugation, washed several times with distilled water and alcohol, and dried at 100 ˚C for 12 h in a vacuum oven.

3.1.4. Synthesis of Graphene Oxide-Magnetite Hybrids

The Magnetite/Graphene Oxide (GO- Fe_3O_4) composite was synthesized by coprecipitation of $FeCl_3$ $6H_2O$ (Loba Chemie, India) and $FeCl_2$ $4H_2O$ (Loba Chemie, India) in the presence of GO. The mixed water solution of $FeCl_3$ and $FeCl_2$ in the ratio of 2:1 was added slowly to the GO solution, and heated with continuous stirring, 10 ml ammonia solution was added to adjust the pH to 10 to precipitate Fe^{2+}/Fe^{3+} ions for synthesis of magnetite (Fe_3O_4) particles. The mixed solution was taken to a ultrasonicate horn (Oscar Ultrasonics, Mumbai). After ultra-sonication for 45 min, the solution was cooled to room temperature. The dark black colored solution was then centrifuged and washed several times with deionized water and dried in vacuum at 70 ˚C.

3.1.5. Physico-chemical characterization

The FT-IR spectra of Magnetite, Graphene Oxide and GO-Fe_3O_4 adsorbent were recorded using Perkin Elmer FT-IR (spectrum RX-I) spectrometer in the range 500-4000 cm^{-1} by mixing the samples with spectroscopy grade KBr (Loba) in 1:2 ratios. Their X-ray diffraction (XRD) patterns were obtained using a Rigaku ultima IVdiffractometer (Rigaku, Japan) using Cu-Kα radiation (λ = 1.54 Å) operating at 40 kV and 40 mA. Scattering angle 2θ was ranged from 10 to 80 at a scanning rate of 2°/minute and was analyzed using standard software. The qualitative element composition of the Fe_3O_4 and GO-Fe_3O_4 adsorbent before and after adsorption of chromium(VI) were analyzed using the energy dispersive spectral analysis (EDS) followed by microstructure analysis with a Nova NanoSEM/FEI FESEM analyzer operated at an accelerating voltage of 10 KeV. Transmission Electron Microscopy (FEI, Technai^{TM} G2)

imaging of bare magnetite particles was performed by drop cast method using a carbon coated copper grid (300 mess, Ted Pella, USA). Specific surface area and adsorption isotherm were measured at liquid N_2 temperature using the Brunauer–Emmett–Teller (BET) surface area analyzer (Quantachrome AUTOSORB-1, USA). The samples were degassed at 150 °C under vacuum. The pH measurements of aqueous solutions were made using a Calibrated Orion 2 Star bench top pH meter. After adsorption, Spectrophotometric determination of Cr(VI), malachite green and phenol red in the filtrate were determined by a UV visible spectrophotometer (Perkim Elmer, USA) using 10 mm quartz cuvettes. Calibrations were done using standard solutions of calculated concentration prepared from their corresponding stock solutions.

3.2. Experimental Details: Adsorption Studies

3.2.1. Preparation of Cr(VI) stock and standard solutions

Potassium dichromate ($K_2Cr_2O_7$) was used as the source for chromium stock solution. All of the required solutions were prepared with analytical reagents and double-distilled water. 2.82 g $K_2Cr_2O_7$ was dissolved in distilled water of 1000 ml volumetric flask up to the mark to obtain 1000 ppm (mg L^{-1}) of Cr(VI) stock solution. Samples of different concentrations of Cr(VI) are prepared from this stock solution by appropriate dilutions. For example, 100 mg L^{-1} chromium stock solution was prepared by diluting 100 mL of 1000 mg L^{-1} chromium stock solution with distilled water in a 1000 mL volumetric flask up to the mark. Similarly, solutions with different metal concentrations such as (10, 20, 30, 40, 50 and 60 mg L^{-1}) are prepared.

3.2.2. Preparation of dye stock and standard solutions

Malachite Green (Sigma-Aldrich, India) of analytical grade was used to prepare the stock solution. 1 gm of malachite green was dissolved in 1000 ml deionized water to make 1000 mg L^{-1} stock solution. Furthermore, 1000 mg L^{-1} phenol red (Sigma-Aldrich, India) stock solution was prepared from 1 gm in 1000 ml deionized water. Various concentrations of dyes were prepared by diluting appropriate amount of the above stock solutions as 10 to 100 mg L^{-1} for malachite green and 10 to 100 mg L^{-1} for phenol red.

3.2.3. Adsorption of Cr(VI) by Magnetite nano particles and GO- Fe_3O_4 hybrids

Adsorption of hexavalent chromium on to the prepared adsorbents (Magnetite nanoparticles and GO-Fe_3O_4) were studied by batch experiments. All of the batch experiments were performed at room temperature. A series of capped bottles were used to avoid change in chromium concentration containing 100 mL of 10 mg L^{-1} Cr(VI) solution. Required amount of adsorbent material was added to each bottle, well shaken for a predetermined time period and then subjected to magnetic separation process. The aqueous volume and chromium concentration were fixed at 100 ml and 10 mg L^{-1} respectively during the whole study for both the adsorbents. Effect of experimental parameters such as adsorbent dose, contact time, pH, and initial concentration have been studied to investigate the Cr(VI) adsorption process for Magnetite nanoparticles and GO-Fe_3O_4 hybrid. The solution pH was adjusted by adding required amounts of 0.1M HCl or 0.1M NaOH solutions. The isotherm studies were performed at room temperature varying initial Cr(VI) concentrations and various isotherm models were used to corroborate the experimental data. Kinetic studies were investigated by different kinetic modelling.

Absorbance spectra of Cr(VI) solution were measured by UV-vis spectrophotometer in 10 mm quartz cuvettes. Absorbance vs. concentration behavior of dichromate solution is complicated because the combined concentration of [$HCrO_4^-$], [CrO_4^{-2}], and [$Cr_2O_7^{-2}$] species together is indicated as Cr(VI) and the equilibrium between these species is dependent on both concentration and pH. Therefore, diphenylcarbazide solution is used for the spectrophotometric determination of Cr(VI) in the aqueous phase. It forms chromium(VI)-diphenylcarbazide complex which gives a distinct red-violet color characteristic of chromium(VI) at 540 nm (**Figure.3.1**).

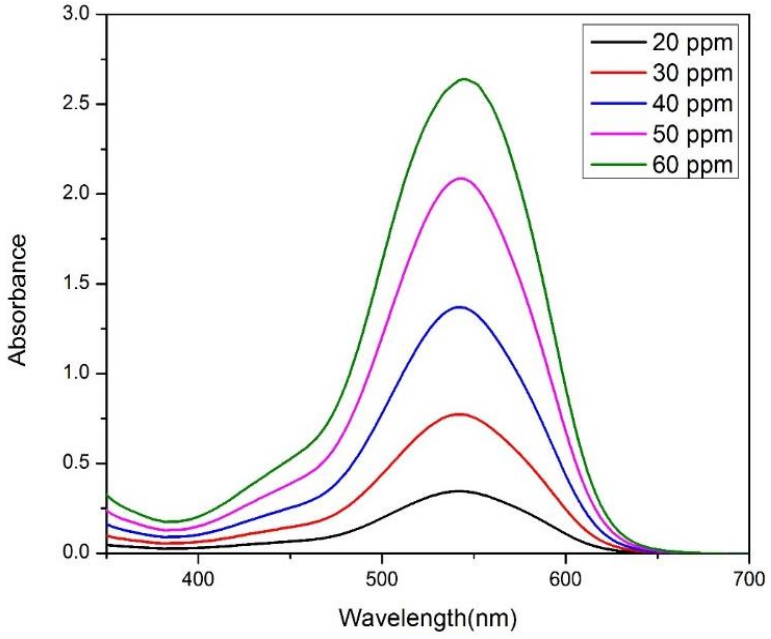

Figure.3.1. Absorption spectrum of Cr(VI)-diphenyl carbazide complex at 540 nm with varying initial concentration of the adsorbate solution.

3.2.4. Adsorption of dyes by GO-Fe_3O_4 hybrid

Adsorption of dyes on to prepared GO-Fe_3O_4 hybrid was studied by batch experiments. Experiment procedures for dyes were almost same as used in batch adsorption of Cr(VI). All of the experiments were performed in capped bottles for a fixed volume (100 mL) of 10 mg L^{-1} dye concentration. Magnets are used for the separation process. Effect of various adsorption parameters such as adsorbent dose, contact time, pH, and initial adsorbate concentration for adsorption of dyes on GO-Fe_3O_4 hybrid have been studied. The pH was adjusted by adding required amounts of 0.1M HCl or 0.1M NaOH to the solutions. Data obtained from effect of initial dye concentration and contact time on adsorption were used for the isotherm and kinetic modelling respectively. UV-vis spectrophotometer is used for the spectrophotometric determination of malachite green and phenol red. It gives a distinct green color characteristic spectra for malachite green at 620 nm (**Figure.3.2**) and a distinct red color characteristic spectra for phenol red at 435 nm (**Figure.3.3**).

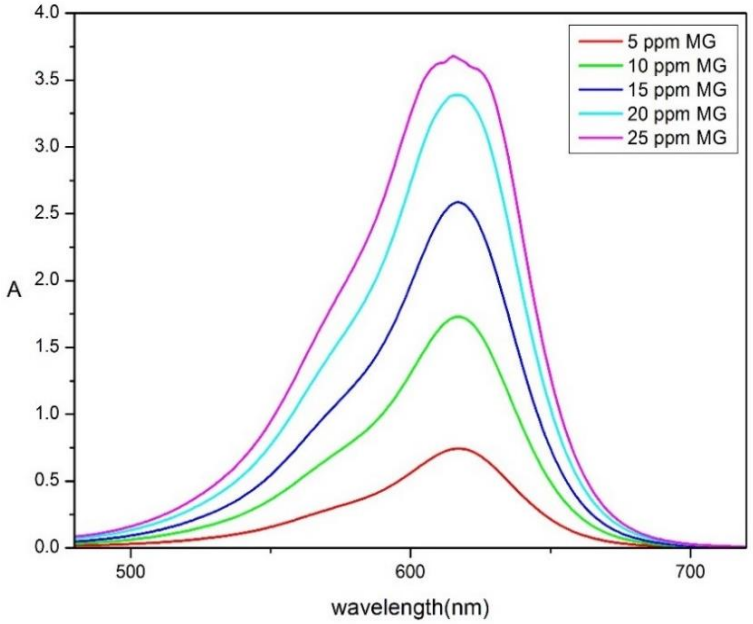

Figure.3.2. Absorption spectrum of malachite green at 620 nm.

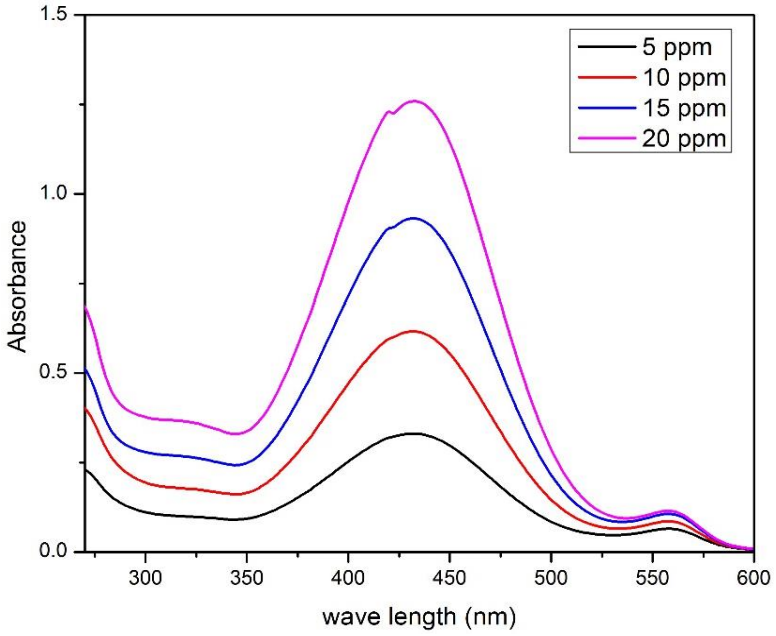

Figure.3.3. Absorption spectrum of phenol red at 435 nm.

3.3. Modelling of Adsorption Kinetics

The kinetics of adsorption was studied by agitating the adsorbent loaded toxin solution for different time intervals, followed by finding out the adsorbate concentration and the adsorption capacity. Initially, the data were modelled based on Lagergren's pseudo-first order and Ho and McKay's pseudo-second order adsorption kinetics. The pseudo-first order kinetics can be expressed as

$$\log (q_e - q_t) = \log\ q_e - \frac{K_I}{2.303\ t} \qquad \textbf{Eq. 3.1}$$

where q_e is the equilibrium adsorption capacity (in mg g^{-1}), q_t is the adsorption capacity (mg g^{-1}) at time t, and K_I is the first order rate constant (in min^{-1}). The pseudo-second order kinetics can be expressed as.

$$\frac{t}{q_t} = \frac{1}{K_{II} q_e^2} + \frac{1}{q_e} t \qquad \textbf{Eq. 3.2}$$

where K_{II} is the second order rate constant (g mg^{-1} min^{-1}). Plotting t/q_t with t, and fitting a straight line to it can enable calculation of the equilibrium adsorption capacity and the rate constant.

The above two kinetic models indicate whether or not the process is governed by chemisorption. However, no information on the diffusion processes can be concluded from the said models. Therefore, to understand more about the adsorption process, the data were analyzed with other established kinetic models, including the Elovich model, Weber-Morris model for intraparticle diffusion, and Bangham model for pore diffusion controlled kinetics.

The Elovich model can be expressed as

$$q_t = \frac{1}{\beta} \ln (\alpha\beta) + \frac{1}{\beta} \ln\ t \qquad \textbf{Eq. 3.3}$$

where, α represents the initial sorption rate, and can indicate the extent of surface coverage. Plotting q_t with t, and fitting the data with a straight line can yield other unknowns. The term β shows the activation energy for chemisorption. Confirmation of this kinetic model itself can mean that diffusion is the main process for adsorption.

To find out the type of diffusive processes involved, one can model the experimental data with intraparticle diffusion model, known as the Weber-Morris model. The expression can be written as

$$q_t = K_{IP} t^{\frac{1}{2}} + C \qquad \textbf{Eq. 3.4}$$

where K_{IP} is the intraparticle diffusion constant (in mg g^{-1} $min^{-0.5}$), and C is the intercept. Plotting the adsorption capacity at a specific time (q_t) with $t^{0.5}$ can yield a straight line as per this equation if the data follow intraparticle diffusion model. However, it has generally been seen that the data set in the above said plot can comprise of various segments. The initial data set may obey a linear relationship, as discussed above, followed by a plateau. In such a case, it may be appropriate only to model the linear part to find out the intraparticle diffusion constant. The onset of the plateau region might indicate the dominance of some other mechanism, mostly other slower diffusive processes, such as diffusion through pores. Additionally, it also can be checked if the linear segment has any intercept with the y-axis (C), in which case, it might indicate the instantaneous adsorption formed by a boundary layer. Moreover, a negative intercept also can mean that the formation of such boundary layer tends to impede the process of adsorption.

The Bangham model can be expressed as follows:

$$\log\log\left[\frac{C_i}{C_i - mq_t}\right] = \log\frac{K_B}{2.303\,V} \propto \log t \qquad \textbf{Eq. 3.5}$$

where, C_i is the initial concentration of the adsorbate solution (in mg L^{-1}), α is a constant usually less than unity, m is the mass of the adsorbent used, and V is the volume of the solution. The quantity $log\ log\ C_i/(C_i - mq_t)$ can be plotted against $log\ t$ to yield a straight line, if the data were to obey Bangham model. The model indicates if pore diffusion has any role to play in the adsorption process. It is physically possible that the adsorbates follow surface diffusion and get adsorbed on the freely available particle surface. However, after the saturation on the surface, the adsorbate moves to the inner pores of particles or agglomerates of the particles. In this process, however, the diffusion slow down, and pore diffusion becomes the rate limiting step.

3.4. Modelling of Adsorption Isotherms

Equilibrium adsorption analysis is important to find out the adsorption levels at a specific adsorbate concentration and to underpin further the types of adsorption followed. Therefore, experiments were conducted by varying the initial adsorbate concentration (mg L^{-1}) and evaluating the equilibrium adsorbate concentration (C_e) and equilibrium adsorption capacity. Thus obtained data were analyzed based on established adsorption isotherm models. The most simplistic adsorption isotherm model is the Langmuir expression, where it is assumed that all of the adsorption sites possess equal affinity for the adsorbate and that no interactions between the adsorbates are possible. This covers from a sub-monolayer to a maximum of monolayer coverage of adsorbate on the adsorbent surface. It can be expressed as

$$\frac{1}{q_e} = \frac{1}{C_e q_m K_L} + \frac{1}{q_m} \qquad \textbf{Eq. 3.6}$$

where, C_e, and q_e are equilibrium adsorbate concentration and capacity, respectively, q_m is the maximum calculated adsorption capacity of the adsorbent (mg g^{-1}), and K_L is the Langmuir adsorption constant (in L mg^{-1}). A plot between C_e^{-1} and q_e^{-1} can yield a straight line, from where the maximum adsorption capacity can be calculated from the intercept. The Langmuir constant is an indicative of the free energy for the process of adsorption (ΔG), which can be calculated with the expression

$$\Delta G = -RT \ln K_L \qquad \textbf{Eq. 3.7}$$

A negative value of free energy indicates spontaneity of the process. Additionally, through a dimensionless equilibrium Langmuir parameter (R_L), it can be found out of the process is favourable. R_L can be expressed as

$$R_L = \frac{1}{1+(1+K_L C_0)} \qquad \textbf{Eq. 3.8}$$

Where C_0 is the initial adsorbate concentration. A value of $R_L > 1$, indicates an unfavorable process, whereas < 1 indicates favorable process. A value of 0 indicates irreversible adsorption process.

The adsorption process on heterogeneous adsorbent surfaces is modelled by the Freundlich isotherm model. It is based on the assumption that the adsorption sites are distributed exponentially with respect to their enthalpy of adsorption. It is generally prevalent with multi-layered adsorption. The model can be expressed as

$$\log q_e = \log K_F + \frac{1}{n} \log C_e \qquad \textbf{Eq. 3.9}$$

Where, K_F is the Freundlich constant, an approximate indicator of adsorption capacity. The term *1/n* is a function of the strength of adsorption; a value of <1 indicates normal adsorption, and >1 indicates cooperative adsorption. The smaller the value of n the higher is the heterogeneity of adsorption in the system, and '*n*' in the range of 1 to 10 generally indicates favorable adsorption process.

By changing the condition of no interactions between the adsorbates in the Langmuir model, a new type of isotherm model can be derived. The Temkin model takes into account the interactions between adjacent adsorbate ions and assumes that the heat of adsorption linearly decreases with the increase of adsorbate coverage on the surface. It can be expressed as

$$q_e = \frac{RT}{b} \ln K_T + \frac{RT}{b} \ln C_e \qquad \textbf{Eq. 3.10}$$

Where, b is the heat of sorption (in Joules mole^{-1}), and K_T is the Temkin equilibrium constant (in L mg^{-1}), R is the universal gas constant, and T is the absolute temperature.

For porous materials, the Dubinin-Raduskevich isotherm model relates the adsorption characteristics with the available porosity in the adsorbents. It assumes a Gaussian distribution of energies on a heterogeneous surface. It can be expressed as

$$q_e = q_s e^{-K_{DR}\epsilon^2} \qquad \textbf{Eq. 3.11}$$

This expression simplifies to the following form

$$\ln q_e = \ln q_s - K_{DR}\varepsilon^2 \qquad \textbf{Eq. 3.12}$$

Where, q_s is the theoretical adsorption saturation capacity (in mg g^{-1}), KDR is the D-R isotherm constant (mol2 J-2). The term ε can be calculated as follows:

$$\epsilon = RT \ln\left[1 + \frac{1}{C_e}\right] \qquad \textbf{Eq. 3.13}$$

By plotting ε^2 with $ln\ q_e$, a straight line fit can be performed. Subsequently the mean free energy for adsorption (E) can be calculated as:

$$E = \frac{1}{\sqrt{2K_{DR}}} \qquad \textbf{Eq. 3.14}$$

This model is generally applied to solutions containing intermediate to high range of concentration.

CHAPTER-4

RESULTS AND DISCUSSION

In this section, all of the outcome of the current work are discussed and are explained in the context of toxic ion removal. In the first part, the structure, morphology, and other physical characteristics of the processed nanoparticles, and hybrid adsorbent are discussed. This is followed by the results and discussions on the adsorption of Cr(VI) by magnetite nanoparticles, and the GO-Fe_3O_4 hybrids. Subsequently, the adsorption of malachite green, a cationic dye, by GO-Fe_3O_4 hybrid adsorbents is presented. In the last part, the adsorption of Phenol red, a neutral dye, on GO-Fe_3O_4 hybrid powders is discussed.

4.1. PROPERTIES OF THE SYNTHESIZED NANOADSORBENTS

4.1.1. Characterization of Magnetite nanoparticles

4.1.1.1. XRD analysis

The XRD patterns of prepared samples were recorded on a (X'pert High Score diffractometer, Rigaku, Japan) using Cu-Kα radiation (λ = 1.54 Å) operating at 40 kV and 40 mA. Scattering angle 2θ was ranged from 10 to 80 at a scanning rate of 2º/minute and was analyzed using standard X'pert High Score software provided with the instrument. Then crystalline structure of the magnetite nanoparticles as shown in **Figure.4.1**. The diffraction peaks of (220), (311), (400), (422), (511) and (440) reflect the magnetite crystal with a cubic spinel structure. The intense diffraction peaks indexed to (220), (311), (400), (422), (511), and (440) planes appearing respectively, are consistent with the standard XRD data for the cubic phase Fe_3O_4 with a face centered cubic (fcc) structure [142].The unit cell of cubic spinel structure consists of eight ferric ions at tetrahedral sites (A sites) each with four oxide ions nearest neighbors, and eight ferric ions and eight ferrous ions at octahedral sites (B sites) each with six oxide ions as the nearest neighbors. This system could be referred to the structural formula of (Fe^{3+}) A $[Fe^{2+}Fe^{3+}]$ BO_4. However, a magnetite can be easily oxidized in presence of air to form the maghemite (γ-Fe_2O_3) at temperature 110–230 ˚C and can be further transformed to the hematite (α-Fe_2O_3) at temperature above 250 ˚C. Generally, the diffraction peaks at (113), (210), (213) and (210) are the characteristic peaks of maghemite and hematite, respectively [143]. However, these peaks do not appear in the XRD pattern which implies no other iron compounds in the synthesized magnetite [144].

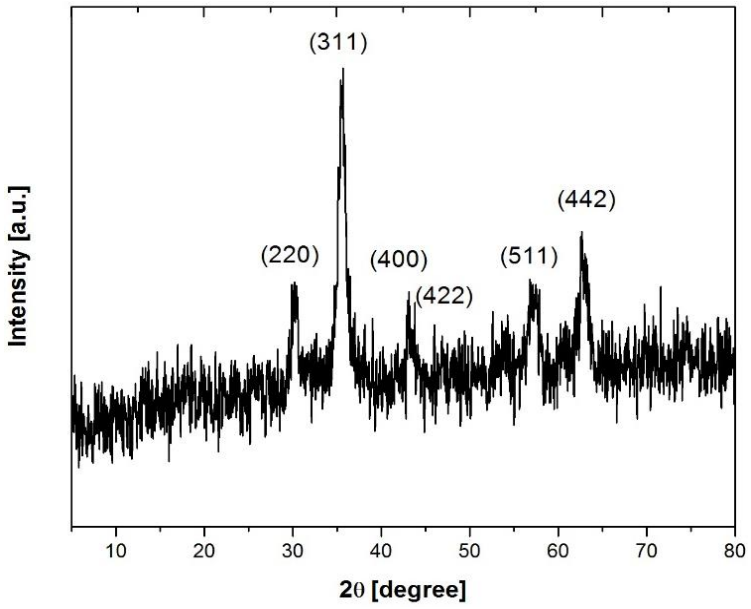

Figure.4.1. XRD pattern of magnetite nanoparticles (JCPDS no. 76-1849).

4.1.1.2. FESEM and EDX analysis

The morphological study (FESEM images) of bare magnetite nano particles as prepared by chemical co-precipitation method are shown in **Figure.4.2**. It consists of sphere shaped particles with diameter ranging from 20-70 nm. From the images, agglomeration of the particles is also shown. Presence of Fe and O in the elemental analysis of magnetite is in agreement with its successful synthesis shown in the EDX spectrum.

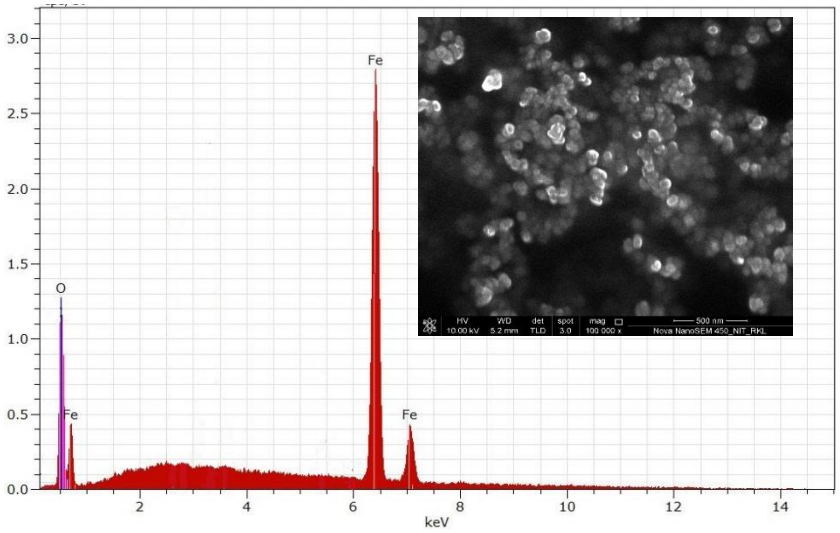

Figure.4.2. FESEM and EDX study of bare magnetite nanoparticles.

4.1.1.3. TEM analysis

The morphological studies of bare magnetite particles are shown in **Figure.4.3** from transmission electron micrographs, which indicated a cluster of spherical shaped nanoparticles in the size range of 20-50 nm. However, these agglomerates are found to be occasional in nature, and well dispersed nanoparticles of 15-30 nm size were frequently observed during microscopy. The presence of pores are clearly visible from the high resolution TEM image of magnetite.

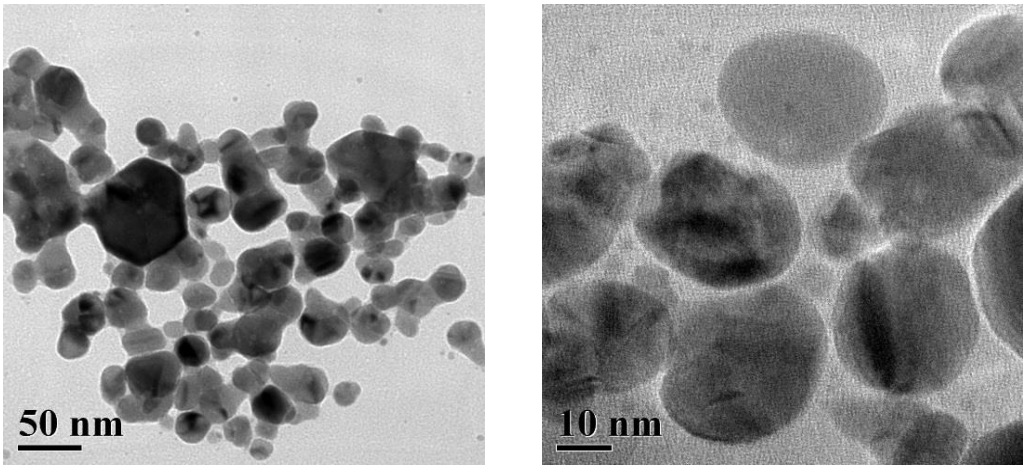

Figure.4.3. TEM images of magnetite particles.

4.1.1.4. BET analysis

BET isotherm studies of magnetite nanoparticles were performed in the N_2 atmosphere at degassing temperature 150 °C. The **Figure.4.4** shows the complete N_2 adsorption and desorption curves for magnetite nanoparticles with observed hysteresis. The BET isotherm is valid within a relative pressure range of 0.02-1.0, giving surface area 128.6 $m^2 g^{-1}$. Presence of small hysteresis between absorption-desorption curve is an indication of presence of mesopores and majority of the pores fall in the range of 2-6 nm shown in the Particle size distribution graph of magnetite nanoparticles.

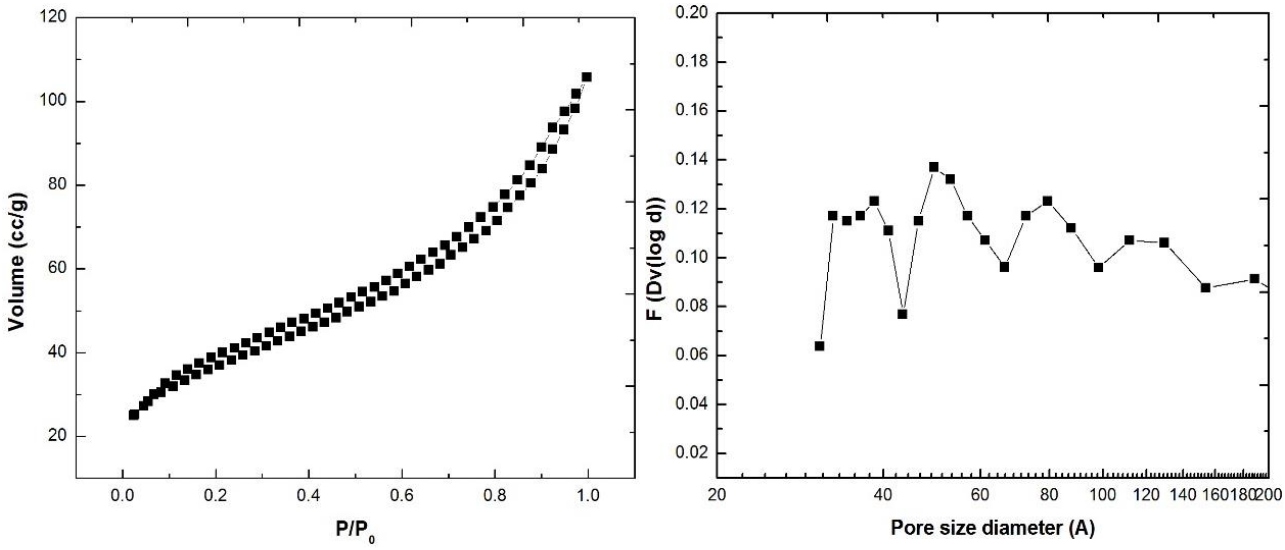

Figure.4.4. BET isotherm (left) and PSD analysis (right) of magnetite nanoparticles.

4.1.1.5. FTIR analysis

FTIR analysis of magnetite nano particles is shown in **Figure.4.5**. The FTIR spectrum have two prominent bands at 580 cm^{-1} for metal-oxygen bond vibration and a small hump at 1630 cm^{-1} corresponds to hydroxyl groups stretching associated to the surface of magnetite nano particles.

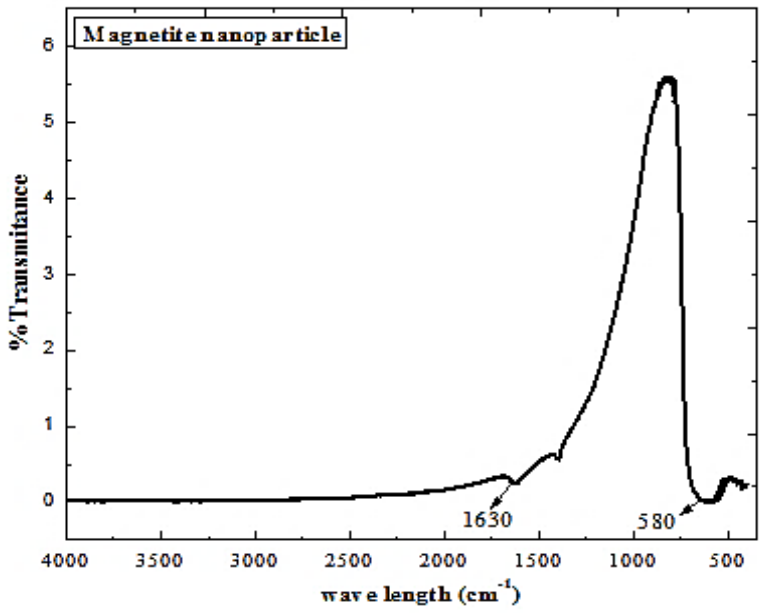

Figure.4.5. FT-IR spectrum of bare magnetite nanoparticles.

4.1.2. Characterization of Graphene Oxides

4.1.2.1. XRD analysis

The XRD patterns of flaky graphite and the synthesized graphene oxide is presented in **Figure.4.6**. The flaky graphite showed characteristic (002) peak of graphitic layers at ~26° of 2θ. However, the peak was found shifted to about 10° for the GO materials. This confirms that the interlayer distance of 3.34 Å in graphitic structure has increased to about 8 Å in graphene Oxide. It can, however, be not claimed as a single layer of GO, since the peak would be absent in such a situation.

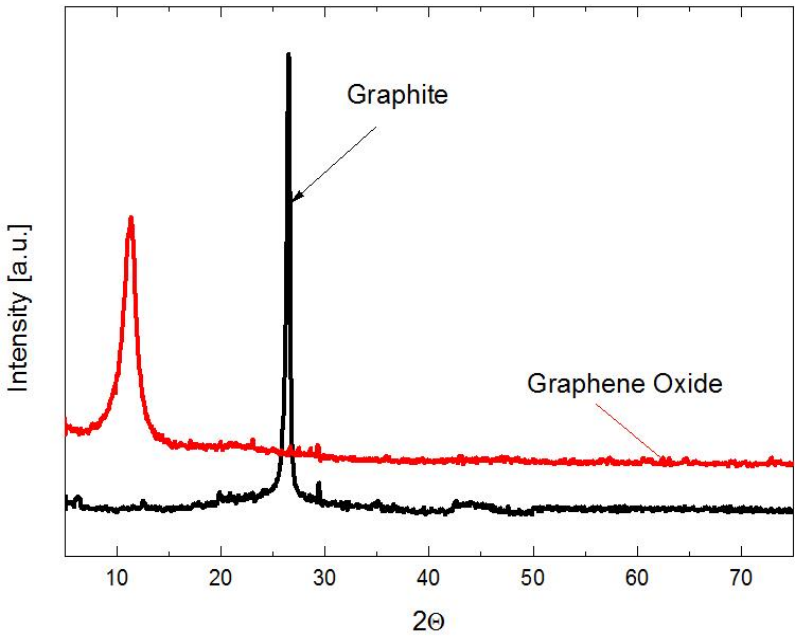

Figure.4.6. X-ray diffraction patterns of graphite and graphene oxide.

4.1.2.2. FESEM and EDX analysis

The typical morphology of GO was analyzed in **Figure.4.7** showing distinctive wrinkled silk like surface, which is a characteristic of the vigorous chemical reactions during the exfoliation process. Presence of large opened GO sheets with highly semi-ordered structures in the SEM image of GO revealed its successful preparation by modified Hummer's method. The

interactions of the interlayered hydrogen bonds facilitate the surfaces of GO sheet to become more hydrophilic.

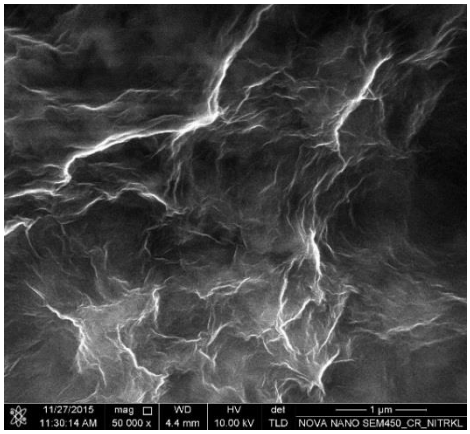

Figure.4.7. FESEM image of graphene oxide.

4.1.2.3. UV-Vis analysis

Further, the formation of GO was proved by the UV-Vis spectrum of the GO colloid in water is presented in **Figure.4.8** that shows the absorption at 230 nm due to π-π* transition of the atomic C=C bonds form the GO sheets.

.

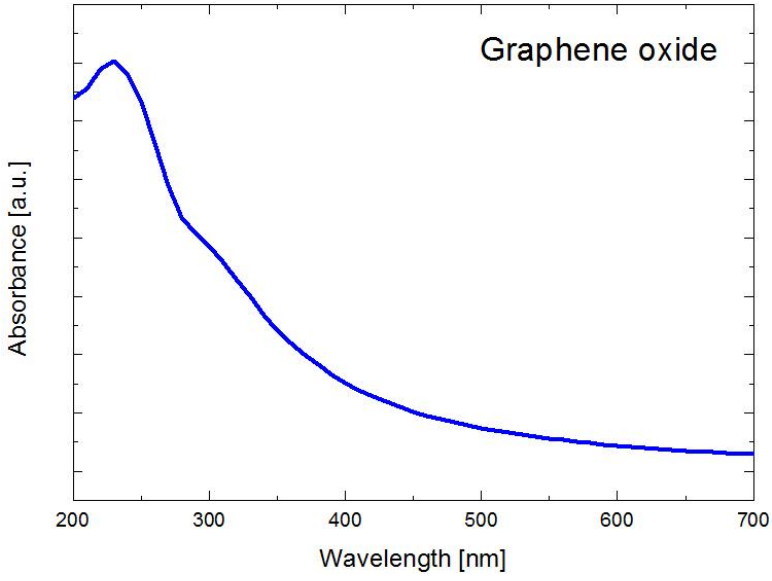

Figure.4.8. UV-Vis spectra of graphene oxide.

4.1.2.4. FTIR analysis

Functional groups such as hydroxyl, carboxyl and epoxy group are introduced characteristics of GO. **Figure.4.9** shows the characteristics FT-IR spectrum of Graphene oxide. In case of Graphene Oxide stretching vibrations of OH functional groups were obtained at 3334 cm^{-1}. The carbonyl group (C=O) stretching vibrations were seen at 1725 cm^{-1} and alkoxy C–O stretching at 1045 cm^{-1}. The aromatic C=C stretching 1615 cm^{-1} and C–OH stretching bands were obtained at 1402 cm^{-1}. All the peaks discussed above satisfied the theoretical characteristics peaks values of graphene oxides.

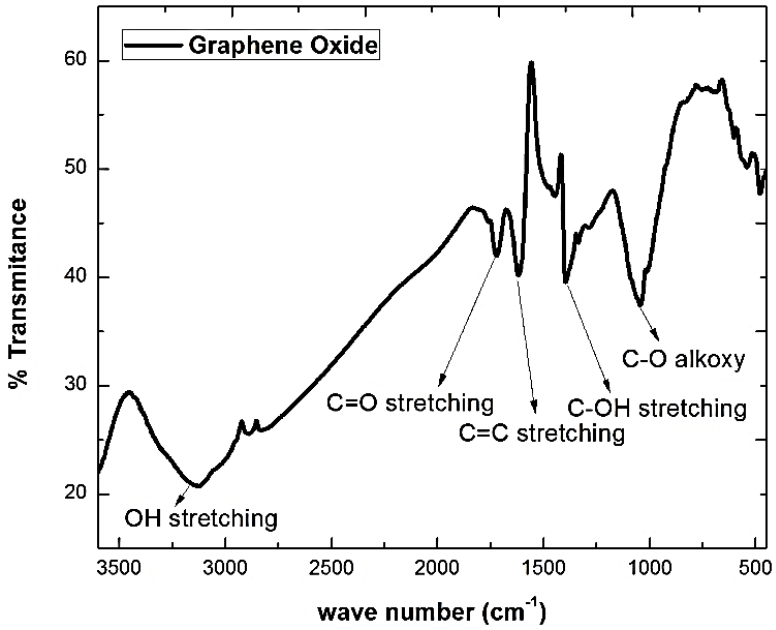

Figure.4.9. FT-IR spectra of graphene oxide.

4.1.3. Characterization of GO-Fe_3O_4 hybrid

4.1.3.1. XRD analysis

The XRD pattern of the GO-Fe_3O_4 hybrid material (**Figure.4.10**) indicates peaks that are predominantly from magnetite. This is due to the fact that the hybrids possess a very low volume fraction of GO. The broad diffraction peaks indicate the nanoparticles with extremely fine crystallites [142]. There are no peaks of GO appeared in XRD pattern of GO-Fe_3O_4 hybrid. The reason is (1) more monolayer graphene oxide caused in the presence of magnetite,

resulting in weaker peaks from carbon being observed; (2) the strong signals of the iron oxides overwhelming the weak carbon peaks [144].

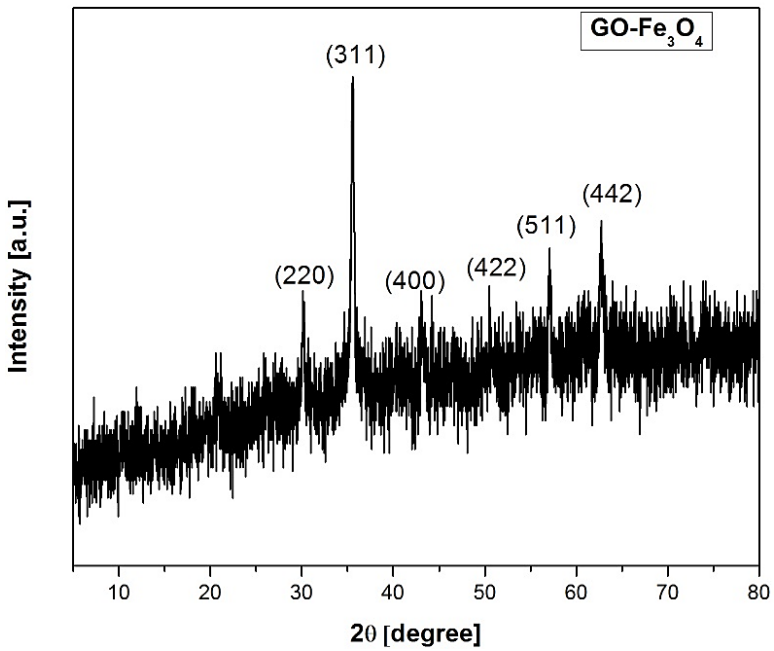

Figure.4.10. XRD pattern of GO-Fe_3O_4 hybrid.

4.1.3.2. FESEM and EDX analysis

In FESEM image of GO-Fe_3O_4 hybrid, Iron oxide nanoparticles are successfully decorated over the GO sheets (**Figure.4.11**). After combination, the crumpled GO waves acted as growing matrix for magnetite nanoparticles and where the nanoparticles are successfully decorated over the GO sheets preventing the former's agglomeration.

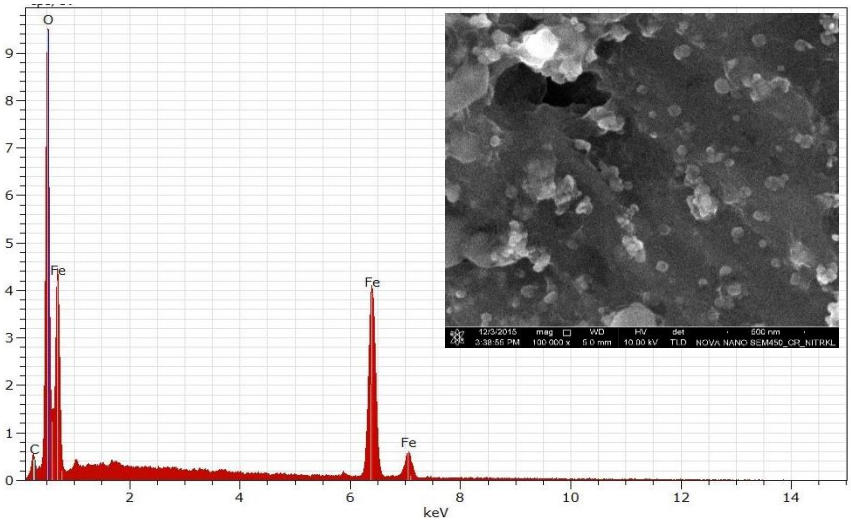

Figure.4.11. FESEM and EDX image of GO-Fe_3O_4 hybrid.

4.1.3.3. FTIR analysis

Figure.4.12 showing the FT-IR spectra of GO-Fe_3O_4 hybrid before and after adsorption. In case of GO-magnetite hybrid, the characteristics peaks are described as O–H stretching was obtained at 3359 cm^{-1}, carbonyl group (C=O) stretching vibrations were seen at 1729 cm^{-1}, the aromatic C=C stretching at 1622 cm^{-1} and C–OH stretching peaks at 1401 cm^{-1}.

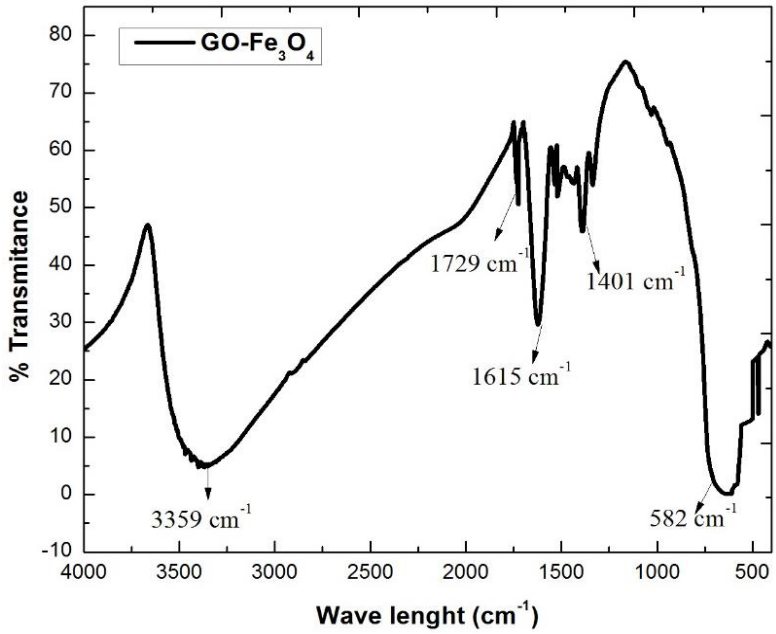

Figure.4.12. FT-IR spectra of GO-Fe_3O_4 hybrid.

4.2. ADSORPTION STUDIES

4.2.1. ADSORPTION STUDIES OF Cr(VI) ON MAGNETITE NANOPARTICLES

4.2.1.1. Effect of adsorbent dose

Effect of variation of adsorbent doses on extent of adsorption was carried out by batch technique. Series of 100 mL hexavalent chromium solution with initial concentration of 10 mg L^{-1} were taken in bottles with varying adsorbent doses from 0.25 to 0.85 gm. The solutions were shaken for almost 90 minutes at room temperature and neutral pH to get the optimum adsorbent dose. From **Figure.4.13**, it can be clearly seen that the general trend of adsorption efficiency of hexavalent chromium increases with increase in adsorbent doses from 11 to 75.7%. The result suggested that increase in adsorption efficiency is due to increase in number of active sites that play an important role in binding the impurities. But a visibly constant value in adsorption efficiency after 0.65 g of adsorbent doses is seen due to agglomeration of particles which reduce the effective surface area. Hence, 0.65 g was considered to be the optimum adsorbent dose and used for further adsorption studies.

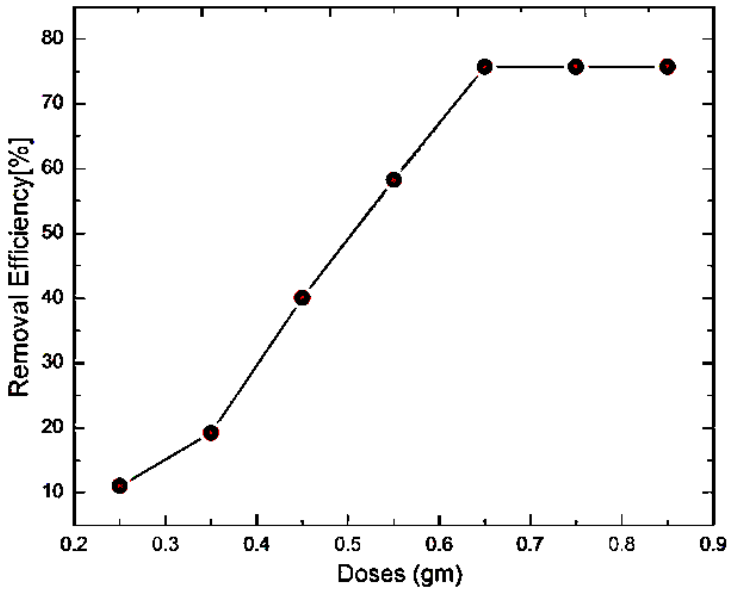

Figure.4.13. Effect of adsorbent doses versus % removal of Cr(VI) using magnetite nanoparticles for initial Cr(VI) concentration of 10 mg L^{-1}, at room temperature and neutral pH.

4.2.1.2. Effect of pH and mechanism of interaction of Fe_3O_4 nanoparticles with Cr(VI)

Metal ion adsorption and its interaction with the adsorbent was probed by varying the pH of the solution. Although pH plays an important role in adsorption, it depends on the type of metal ions (adsorbates) and its chemistry in solution. Optimization of pH was carried out for series of 100 mL of 10 mg L^{-1} of Cr(VI) solution using 0.65 g adsorbent dose at room temperature. The pH of the solution was maintained by suitable acid and base like (0.1 M) HCl and (0.1M) NaOH. From **Figure.4.14** it is evident that increase in pH leads to decrease in adsorption efficiency of hexavalent chromium. At pH < 5 and > 2 the predominant form of Cr(VI) is $HCrO_4^-$ (oxo-anion). That mechanism is briefly discussed later through predominance diagram (**Figure.4.27**). Under acidic medium adsorbent surface is highly protonated that leads to electrostatic attraction with chromium oxo-anions [151]. Higher pH leads to deprotonation of adsorbent surface resulting in electrostatic repulsion with chromium oxo-anions. Also higher pH leads to partial dissolution and coating phenomenon of magnetite nano particles in presence of excess NaOH [152, 153]. The two steps mechanism of dissolution of iron oxides as a function of pH is summarized in next adsorption system. It is also possible that $[OH^-]$ is high at higher pH leads to competition with negative oxo-anion. So, the optimized pH value for maximum 75.6 % adsorption was found at pH 4.

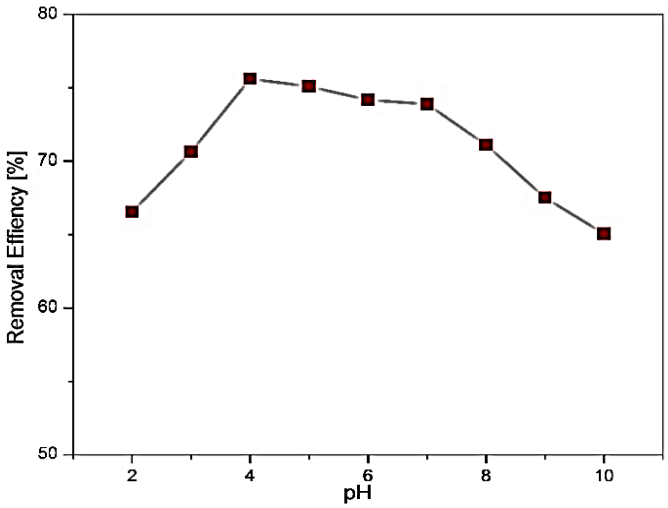

Figure.4.14. Effect of pH versus % removal of Cr(VI) using magnetite nanoparticles for initial Cr(VI) concentration of 10 mg L^{-1}, adsorbent dose 0.65 g and at room temperature.

4.2.1.3. Adsorption Kinetics

The rate of adsorption was performed by varying the contact times from 10 to 100 mins with 10 mg L^{-1} of Cr(VI) solution, 0.65 g adsorbent dose at room temperature for pH-4. It is observed from the **Figure.4.15** that adsorption efficiency increased up to a maximum of 75.7% with time of adsorption than became constant after 90 minutes. This may be because of number of open available sites that progressively get saturated with the formation of a monolayer of metal ions on the adsorbent surface. So, the optimum time period was considered to be 90 mins which prove, the rate of adsorption is considerably lower. Also, the slope is almost uniform throughout the graph for all time intervals it means the material is not kinetically much active.

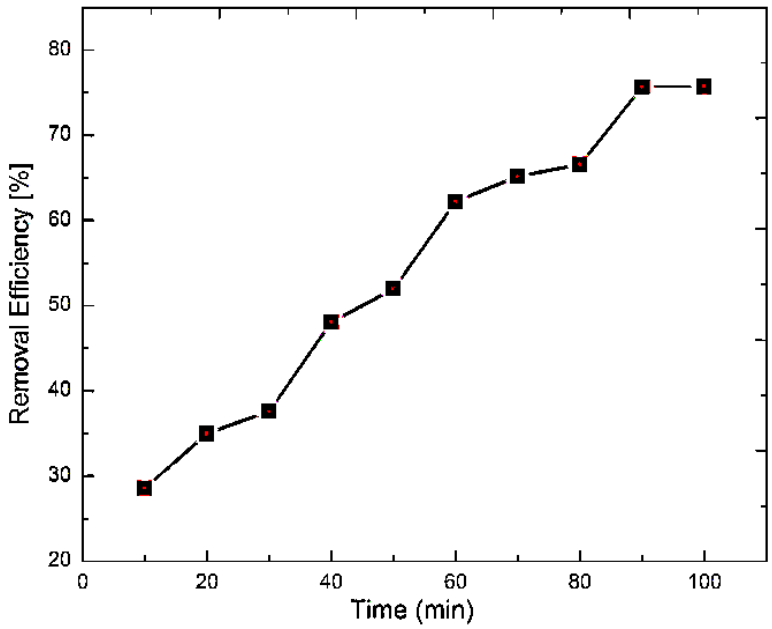

Figure.4.15. Effect of contact time versus % removal of Cr(VI) using magnetite nanoparticles for initial Cr(VI) concentration of 10 mg L^{-1}, adsorbent dose 0.65 g and pH 4.

Adsorption kinetic mechanisms of Cr(VI) on magnetite nano particles were investigated by fitting the experimental data with different kinetic models such as pseudo-first-order (**Eq. 3.1**), pseudo-second-order (**Eq. 3.2**), Elovich (**Eq. 3.3),** Weber- Morris (**Eq. 3.4)** and Bangham (**Eq. 3.5)** models, which are extensively used for all adsorption process [154, 155]. The fitting results obtained from different models are summarized in **Table.4.1**.

Fist the experimental data were fitted by pseudo-first order and pseudo-second order models indicated acceptable fits to the experimental data, with the second order model showing better regression coefficient R^2=0.98 (**Figure.4.16**). The maximum adsorption capacity (q_e) of 1.67 mg g^{-1} and K_{II} of 0.01 g mg^{-1} min^{-1} was found out. The initial adsorption rate, V_0 ($K_{II}q_e^2$) was also calculated from the pseudo-second order data to be 0.03 mg g^{-1} min^{-1}. Thus experiment results supports the assumption behind the model that the rate limiting step in adsorption of Cr(VI) through chemisorption.

Table.4.1. Kinetic parameters for Cr(VI) removal onto magnetite nanoparticles.

Kinetic models	**Parameters**	**Values**
Pseudo-1st Order	R^2	0.929
	K_I (min^{-1})	0.024
	q_e (mg g^{-1})	1.294
Pseudo-2nd Order	R^2	0.975
	K_{II} (g mg^{-1} min^{-1})	0.01
	q_e (mg g^{-1})	1.67
	V_0 (mg g^{-1} min^{-1})	0.03
Elovich	R^2	0.966
	β (mg g^{-1} min^{-1})	2.75
	α (g mg^{-1})	0.18
Weber-Morris	R^2	0.99
	K_{IP} (mg g^{-1} $min^{-1/2}$)	0.126
Bangham	R^2	0.99
	K_B (ml g L^{-1})	62.13
	α	0.78

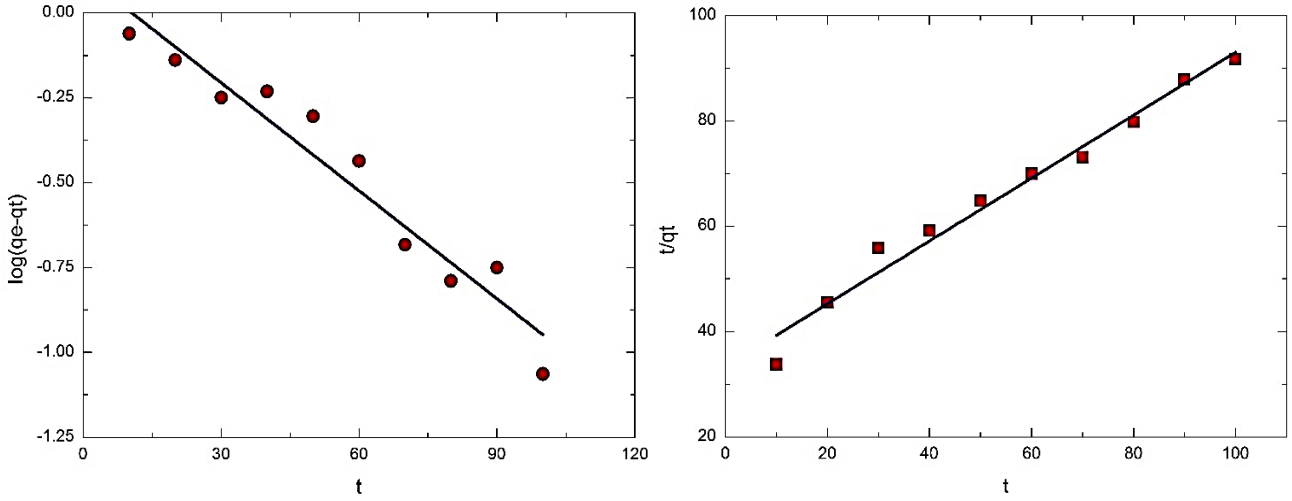

Figure.4.16. Pseudo-first-order model and Pseudo-second-order model for the removal of Cr(VI) by magnetite nanoparticles.

To understand the nature of diffusion kinetics the Elovich model was applied, which showed acceptable R^2=0.966 as evidence that the rate determining step is not completely diffusion in nature but moderately it affects the adsorption process (**Figure.4.17**).

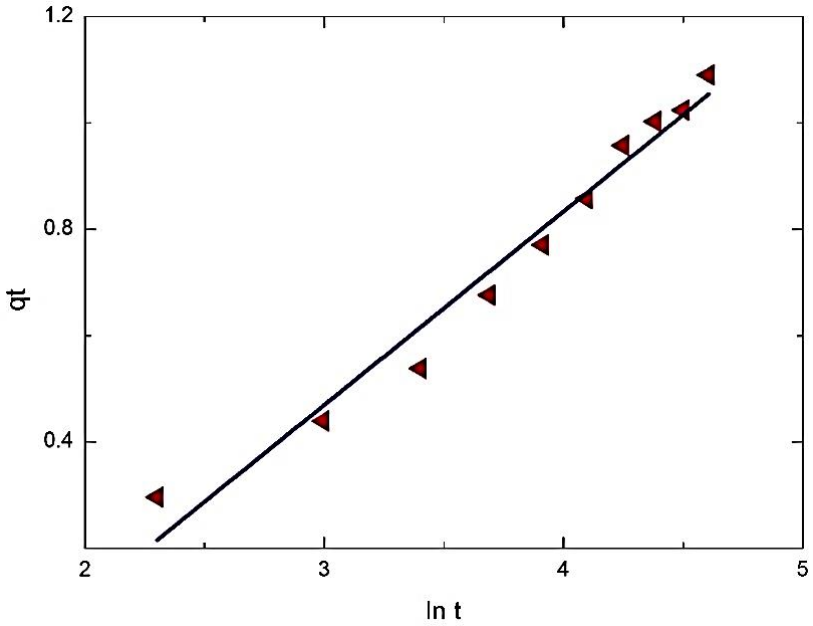

Figure.4.17. Elovich model for the removal of Cr(VI) by magnetite nanoparticles.

To assess the type of diffusion mechanisms involved in the adsorption process, the intraparticle diffusion model (Weber-Morris equation) was applied. The data indicated excellent fit (R^2=0.99) with $t^{0.5}$ in the x-axis (**Figure.4.18)** pointing out the first stage of kinetics is intraparticle diffusion controlled. In the process, the adsorbent progressively adsorbs onto the Fe_3O_4 nanoparticles, as the process may be controlled by surface diffusion. In addition, the fact that the fitted straight line almost passes through the origin indicates the formation of boundary layer is not there.

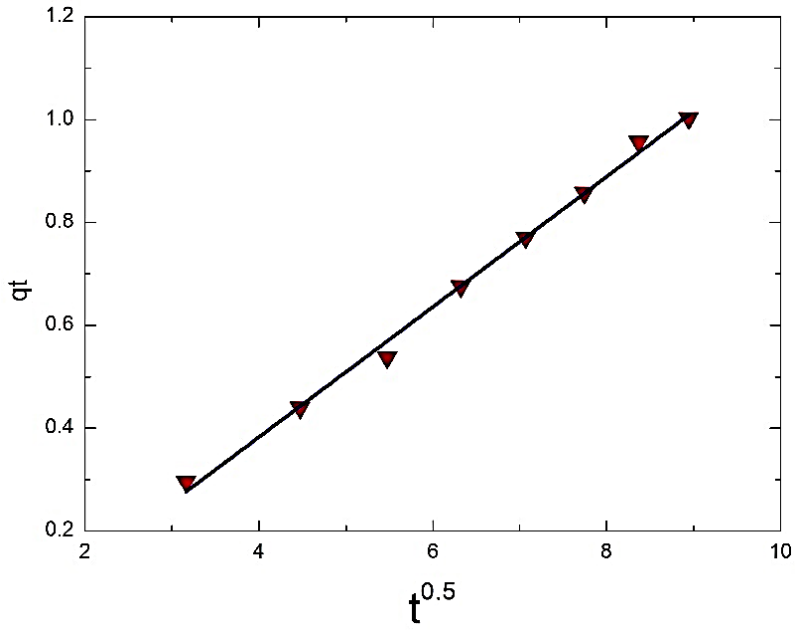

Figure.4.18. Weber- Morris model for the removal of Cr(VI) by magnetite nanoparticles.

The adsorption close to the saturation time cannot be modelled based on the W-M model, where the adsorption significantly decreases indicating the dominance of the other processes during such stage (close to saturation). In order to understand if the effect of porosity is there, the data was modelled based on its Bangham kinetic equation (**Figure.4.19**). Interestingly, the data confirmed to Bangham model with excellent fit (R^2=0.99). It is possible that after the kinetically enhanced uptake of the Chromium (VI) ions by the adsorbate, the diffusion of the toxins can be controlled by its diffusion through the pore clusters of the nanoparticles. Occasional porosity in the nanoparticles has been seen by TEM image (**Figure.4.3**) of

magnetite which corroborates the conclusion from the Bangham model. Thus, it can be inferred that the adsorption of chromium is primarily surface-diffusion controlled with some contribution from pore diffusion.

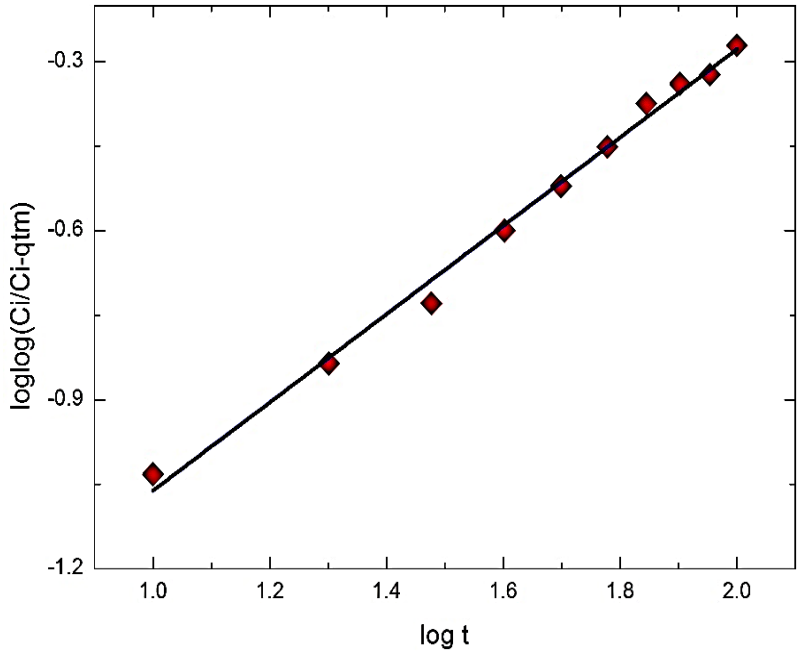

Figure.4.19. Bangham model for the removal of Cr(VI) by magnetite nanoparticles.

4.2.1.4. Adsorption Isotherms

The effect of initial Cr(VI) concentration on adsorption was performed to investigate the type of adsorption behavior of the material surface. Adsorption may be monolayer or multilayer depending on the type of interaction of metal ion with the adsorbent surface. Batch experiment was performed at room temperature by varying the initial Cr(VI) concentration from 10 to 60 mg L^{-1} using 0.65 g adsorbent at pH-4 well shaken for 90 mins. **Figure.4.20** shows that the adsorption behavior seems to be monolayer or takes place at homogeneous surface as adsorption efficiency decreases with increase in initial Cr(VI) concentration. The reason is that the adsorbent dose is constant for all concentrations and the number of active adsorption sites are fixed which get saturated with concentration.

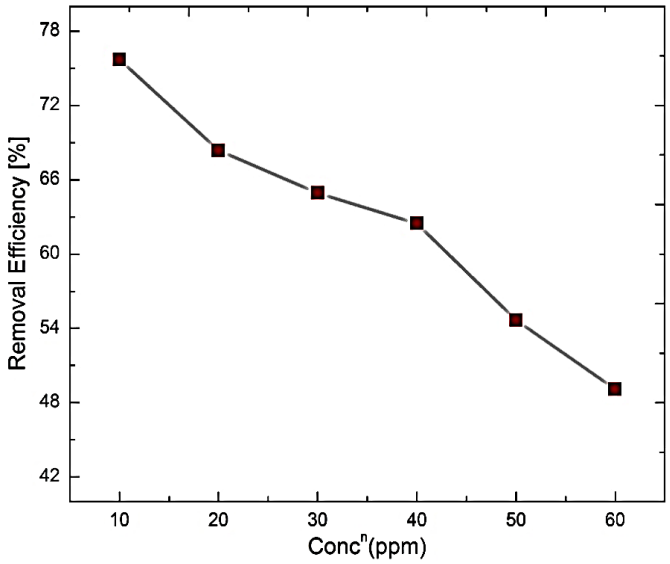

Figure.4.20. Effect of initial Cr(VI) concentration versus % removal using magnetite nanoparticles for adsorbent dose 0.65 g, pH-4, room temperature and time 90 mins.

Further mechanism of adsorption is estimated by different isotherm modellings such as Langmuir (**Eq. 3.6)**, Freundlich (**Eq. 3.9)**, Temkin (**Eq. 3.10)** and Dubinin–Radushkevich (**Eq. 3.12)** equations. All the corresponding isotherm parameters were calculated from their slopes and intercepts, summarized in **Table.4.2**.

The Langmuir adsorption isotherm describes monolayer formation that takes place in homogeneous surface. This model assumes uniform energies of adsorption onto the surface and no transmigration of adsorbates in the plane of the surface. The Langmuir plot obtained from C_e^{-1} and q_e^{-1} yields a straight line as shown in **Figure.4.21**. The plot indicated that adsorption of Cr(VI) onto magnetite is applicable to monolayer adsorption isotherm with very good fitting higher $R^2 = 0.99$. The maximum adsorption capacity, q_m and Langmuir constant, K_L could be evaluated from the slope and intercept. The maximum monolayer adsorption capacity (q_m) of magnetite nanoparticles was calculated to be 5.9 mg g^{-1}. The free energy, ΔG (**Eq. 3.7**) calculated from the Langmuir constant was found to be -11.38 kJ mol^{-1}, which indicates that the process is spontaneous with +ve enthalpy. Moreover, the magnitudes of equilibrium parameter (R_L) calculated from **Eq. 3.8** falls between 0.489 for 10 mg L^{-1}

concentration of Cr(VI). This represents favorable adsorption of Cr(VI) oxo-anion with adsorbent [156].

Table.4.2. Isotherm parameters for Cr(VI) removal onto magnetite nanoparticles.

Isotherm models	**Parameters**	**Values**
Langmuir	R^2	0.99
	q_m (mg g^{-1})	5.9
	K_L (L mg^{-1})	0.098
	ΔG (kJ mol^{-1})	-11.38
	R_L	0.489
Friendlich	R^2	0.96
	K_F (mg g^{-1})	0.88
	n	1.79
DR	R^2	0.95
	K_{DR}	-0.001
	q_m (mg g^{-1})	5
	E (kJ mol^{-1})	16.9
Temkin	R^2	0.975
	b (J mol^{-1})	1764.34
	K_T (L g^{-1})	0.858

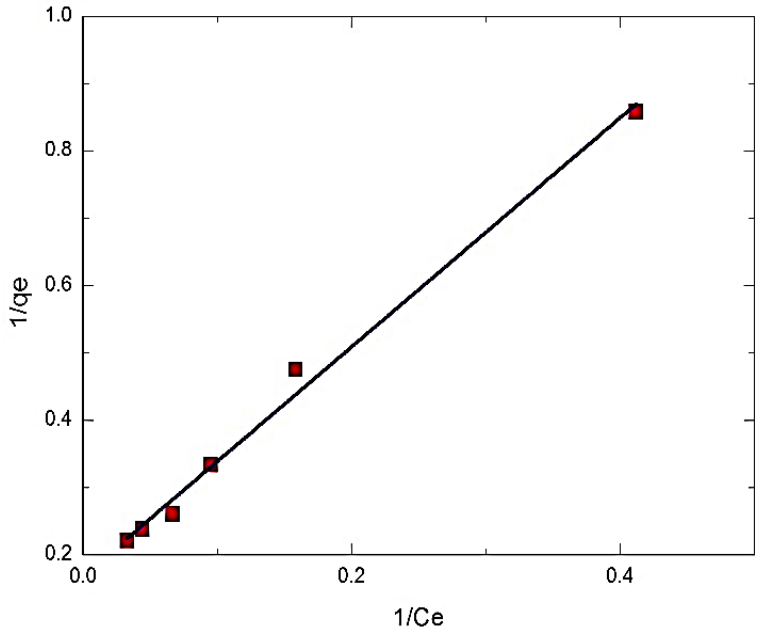

Figure.4.21. Langmuir model for the removal of Cr(VI) by magnetite nanoparticles.

The possibility of adsorption of Cr(VI) on heterogeneous surface was modelled by Freundlich isotherm model. The linear plot of log q_e and log C_e showed a moderate fit with regression coefficient of 0.96 (**Figure.4.22**), indicating that multilayer formation on adsorbent surface is not significant. The Freundlich constant, K_F and Freundlich coefficient, n were calculated from the slope and intercept as 0.88 mg g^{-1} and 1.79. The value of n is an indication of favorable adsorption process.

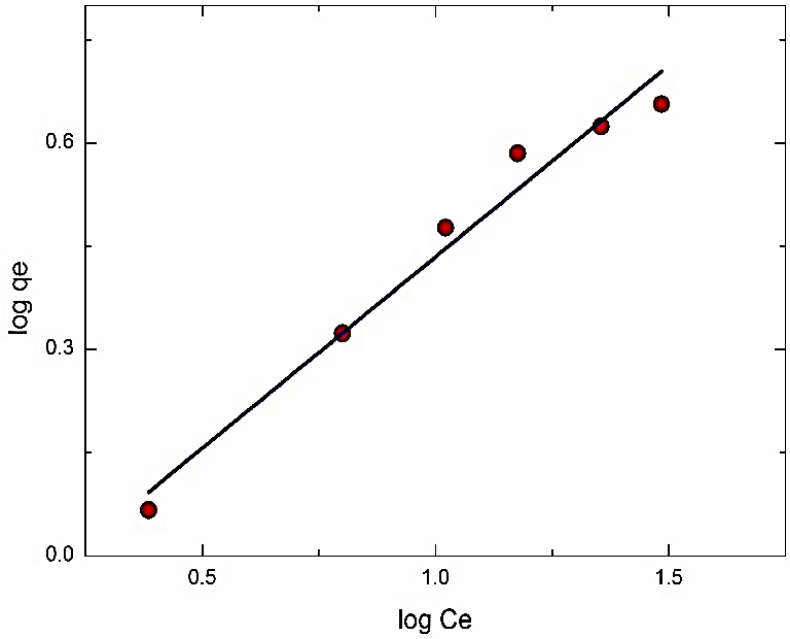

Figure.4.22. Freundlich model for the removal of Cr(VI) by magnetite nanoparticles.

To evaluate the adsorption potentials of the Fe_3O_4 nanoparticles for Cr(VI) ions, Temkin isotherm model was used. The Temkin plot of lnC_e vs. q_e is presented in **Figure.4.23**. The linear fit of Temkin model is acceptable with R^2=0.975. The energy parameter b, related to heat of adsorption was found to be 1.7 kJ mol^{-1} indicating the process of adsorption is chemisorption.

The experimental data were found to be partially applicable to D-R model with R^2 value 0.95 (**Figure.4.24**). The type of adsorption is also predicted by the mean sorption energy (E) value from the D-R model. The value of E (**Eq. 3.14**) for this system was found to be 16.9 kJ mol^{-1} suggesting the chemical nature of adsorption. The Langmuir maximum adsorption capacity of 5.9 mg g^{-1} was found to be comparable to the D-R adsorption capacity of 5 mg g^{-1}. It means

adsorption of Cr(VI) onto magnetite surface is completely monolayer with a uniform distribution of adsorption energy.

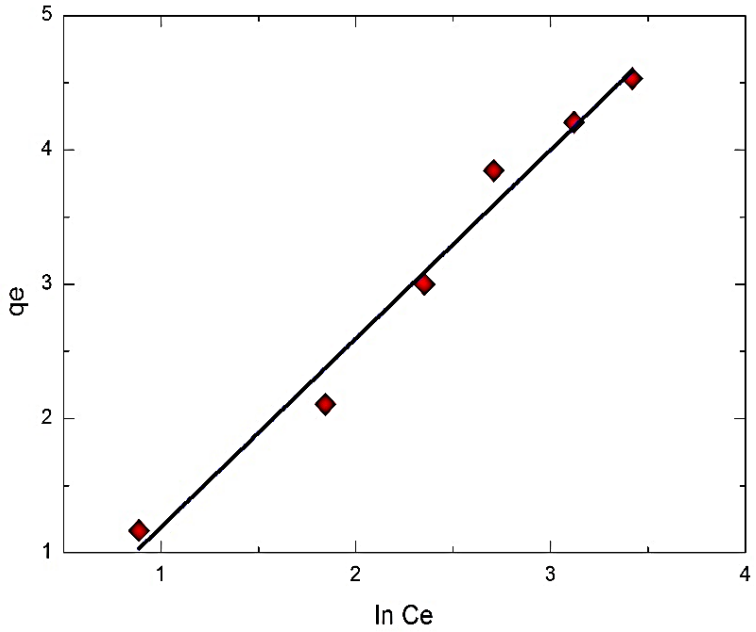

Figure.4.23. Temkin model for the removal of Cr(VI) by magnetite nanoparticles.

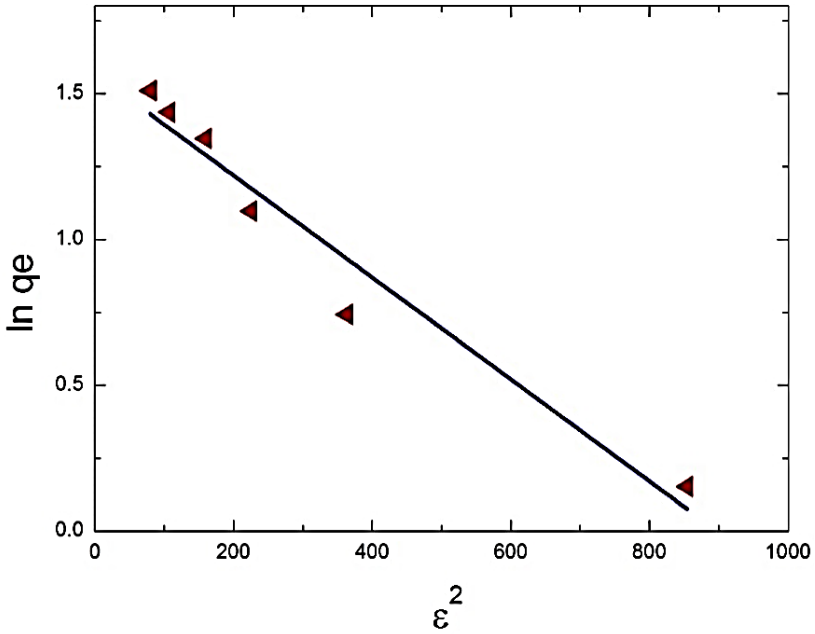

Figure.4.24. D-R model for the removal of Cr(VI) by magnetite nanoparticles.

4.2.1.5. Mechanism of Desorption

Desorption experiment is generally assessed for the economic and cost effectiveness of used adsorbent [24]. The reusability test was done by acid or base leaching process. The reagents used would not affect the adsorbent bed after desorption experiment so that it can be used again as fresh one. Both adsorption and desorption of the metal ions are strongly dependent on pH of the solution. So, 0.1M HCl and 0.1M NH_4OH are used for our studies, to find out desorption efficiency as a function of pH (**Figure.4.25**). The desorption efficiency (DE) was calculated by using equation.

$$DE\ (\%) = \frac{\text{Concentration of Cr(VI) desorbed into the eluate}}{\text{Concentration of Cr(VI) adsorbed onto the adsorbent}} \times 100 \qquad \textbf{Eq. 4.1}$$

The highest desorption efficiency was calculated to be 67.23% at highest pH-12. The poor desorption is attributed to chemisorption. As discussed before the process of adsorption of Cr(VI) on magnetite nanoparticle is favorable (75%) in acidic medium. But under basic medium process of desorption predominance over adsorption. Higher pH leads to negatively charged magnetite surface so that all possible desorption occurred due to electrostatic repulsion. Also, NH_4OH helps chromium to desorb as corresponding ammonium chromate salt to the solution at high pH [145]. Sometimes NH_4OH is known to help in reduction of Cr(VI) to the less toxic Cr(III) [145].

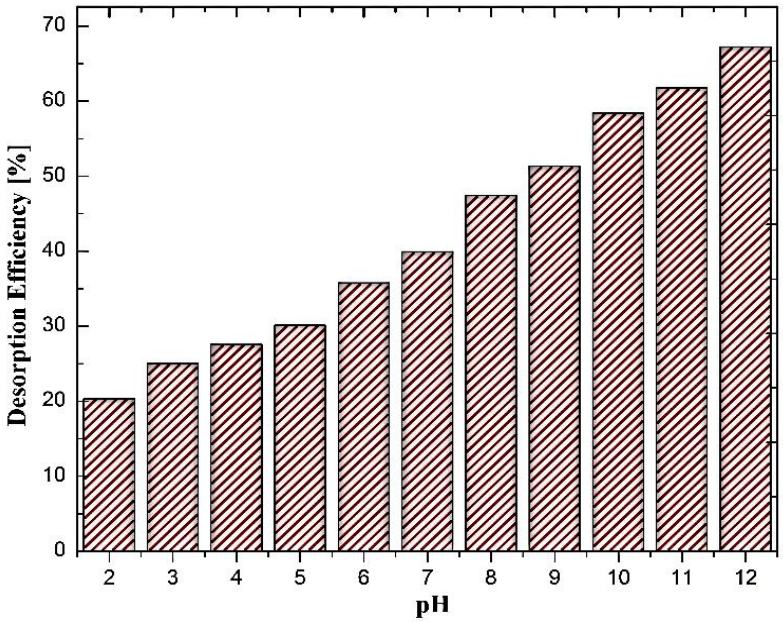

Figure.4.25. %desorption of Cr(VI) from magnetite nanoparticles as a function of pH.

4.2.2. ADSORPTION STUDIES OF Cr(VI) ON GO-Fe_3O_4 HYBRIDS

4.2.2.1. Effect of Adsorbent Dose

Adsorption studies were mainly carried out by batch technique to obtain equilibrium data. A series of 100 mL samples having Cr(VI) initial concentration 10 mg L^{-1} were shaken for 1h with the varying adsorbent doses. It was observed from **Figure.4.26** that the adsorption efficiency of was increased from ~ 61 to ~ 95% with increase the adsorbent dose from 0.05 to 0.35 g, as number of active sites increases with respect to adsorbent dose. A very high value of adsorption efficiency is seen for this system at dose 0.25 g (less) than dose 0.65 g (high) for magnetite nanoparticles. However, it was observed that after dose of 0.25 g, there was no significant change in adsorption efficiency of Cr(VI). This may be due to overlapping of active sites at higher dose. So, there was not any significant increase in the effective surface area due to the agglomeration of particles considering 0.25 g per 100 mL as optimum dose for further study.

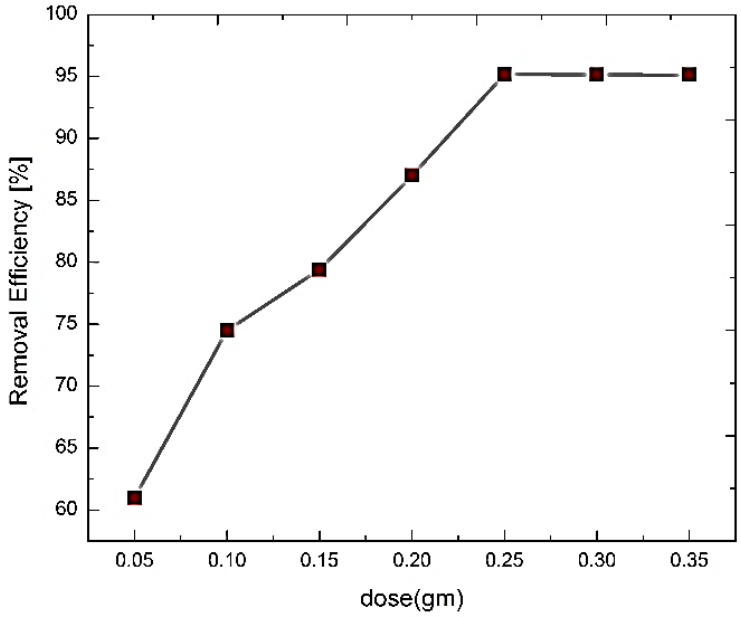

Figure.4.26. Effect of adsorbent dose versus % removal of Cr(VI) using GO-Fe_3O_4 hybrids with initial Cr(VI) concentration of 10 mg L^{-1}, at room temperature and neutral pH.

4.2.2.2. Effect of pH, mechanism of interaction of GO-Fe_3O_4 hybrids with Cr(VI)

The incorporation of magnetite nanoparticles on graphene oxide limits their re-stacking and aggregation, thereby enhancing the surface area of the composite. The growth of metal oxide nanoparticles on graphene oxide sheets results in less agglomeration among particles as GO acts as building blocks for the nanoparticles growth and keeps them in dispersed form. Furthermore, the functional groups and defect sites of GO act as the nucleation and growth sites for Fe_3O_4 nanoparticles.

The pH dependence experiment of Cr(VI) adsorption is largely allied to the metal chemistry in the solution, as it exists in different ionic forms in solution and also to the properties of the adsorbent used. The most common Cr(VI) states in solution are chromate ($Cr_2O_7^{2-}$), dichromate ($Cr_2O_7^{2-}$) and hydrogen chromate ($HCrO_4^-$) at various pH of the solution. At pH <5 and >2 the dominant form of Cr(VI) is hydrogen chromate [146, 147, 157, 158] ion [$HCrO_4^-$] in dilute solution but the dichromate ion is predominant in more concentrated solutions. Increasing the

pH would shift the equilibrium to the CrO_4^{-2} oxy anion. At pH less than 2 the dichromate ion, $Cr_2O_7^{-2}$ is the key species that exists in solution [147]. The distribution of Cr(VI) species as dependence on both pH and total chromium concentration is shown by a predominance diagram (**Figure.4.27**).

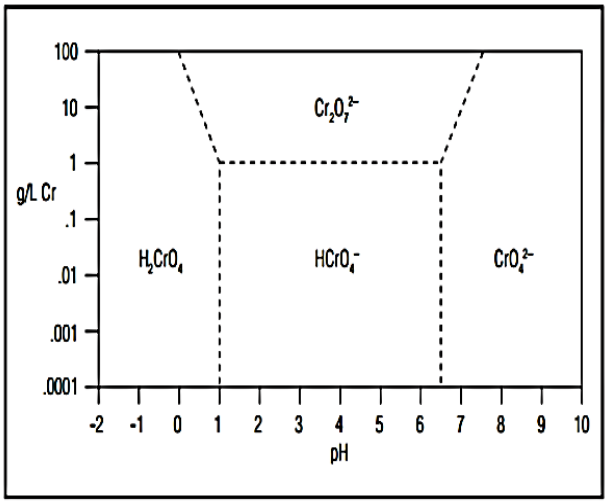

Equilibrium reactions:

$$H_2CrO_4 \leftrightarrow H^+ + HCrO_4^-$$

$$HCrO_4^- \leftrightarrow H^+ + CrO_4^-$$

$$2HCrO_4^- \leftrightarrow Cr_2O_7^{2-} + H_2O$$

Figure.4.27. The predominance diagram with relative distribution of Cr(VI) species in water as a function of pH and concentration of chromium along with its equilibrium reactions.

In a solution containing Cr(VI) ions, the interaction of hexavalent chromium certainly would depend on the pH of the medium. Hence, adsorption was measured as a function of pH of the solutions and its role in the interaction of the magnetite particles and graphene oxide. The optimization of pH was studied for an initial Cr(VI) concentration of 10 mg L^{-1} and the pH of the solution were adjusted from pH 1 to10 using dilute (0.1M) of both HCl and NaOH. At pH 3-4, due to higher $[H^+]$ the hydrated surface of graphene oxide is protonated leading to positively charged surface, and this promotes the adsorption of $HCrO_4^-$ (oxo-anion) due to electrostatic attraction. The magnetite particles are also involved in an electrostatic interaction with the $HCrO_4^-$ anion as well as protonated hydroxyl groups on the surface [151]. The mechanism of protonation of iron oxide surface is summarized in two steps [153]. First, in aqueous solution Fe is coordinated to a neutral OH/OH_2 pair forming a neutral compound $[Fe^{III}(OH)(OH_2)]$, Second in acidic medium the OH group absorb a proton to form a positively charged compound $[Fe^{III}(OH_2)_2]^+$, which helps in electrostatic attraction with $HCrO_4^-$ anion.

The overall mechanism and different modes of interaction of GO-Fe_3O_4 hybrids with $HCrO_4^-$ could be summarized in **Figure.4.28**. Above pH-4, the surface charge of adsorbent becomes negative with the slow deprotonation of the surface groups thereby acquiring a negative charge leading to electrostatic repulsion between the hexavalent chromium oxo-anion and the adsorbent surface (**Figure.4.29**). It is evident from the above data that there was decrease in adsorption efficiency with increase in pH of the solution. It means higher pH leads to partial dissolution of magnetite nanoparticles in the aqueous solution and also may be due coating phenomena at around neutral and higher pH due the presence of sodium hydroxide [152]. As discussed before increase in pH also increase OH^- concentration in the solution which competes with Cr(VI) oxo-anions. The measured data suggested that the optimum pH for removal of Cr(VI) was 4. This is a characteristic feature associated with the existence of hydrochromate anion as reported by several groups working on the removal of chromium [146, 148].

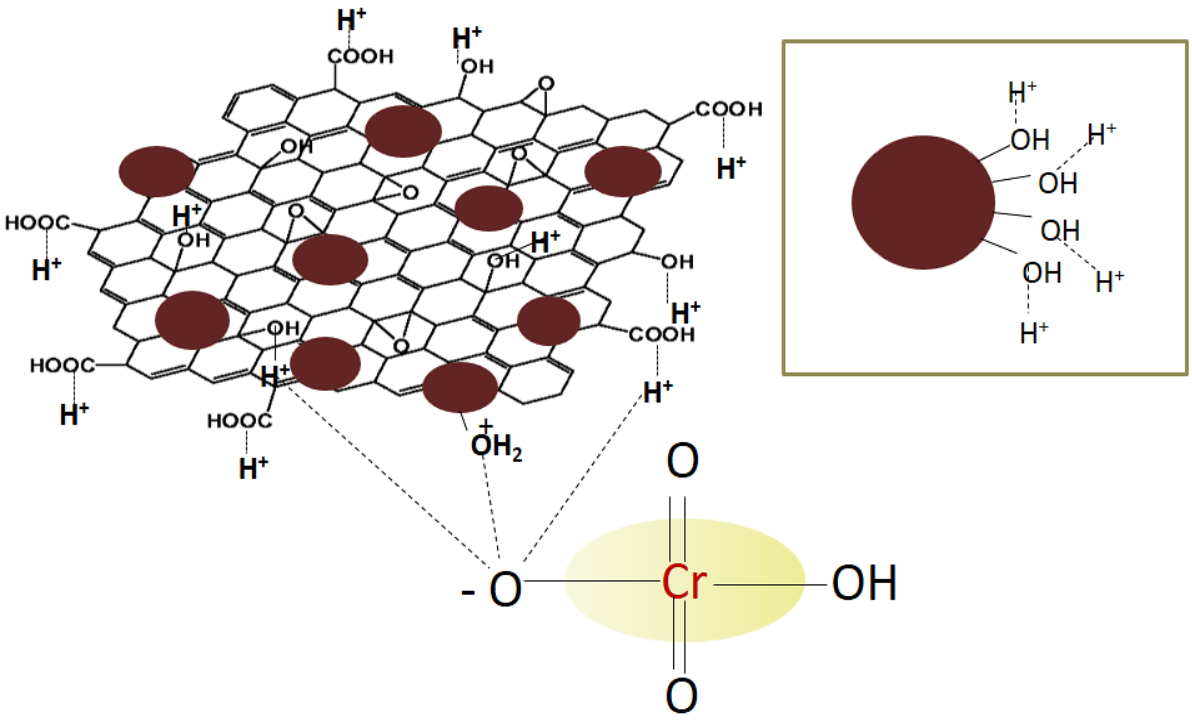

Figure.4.28. Possible interactions involved in the adsorption of Cr(VI) on GO-Fe_3O_4 at optimum pH.

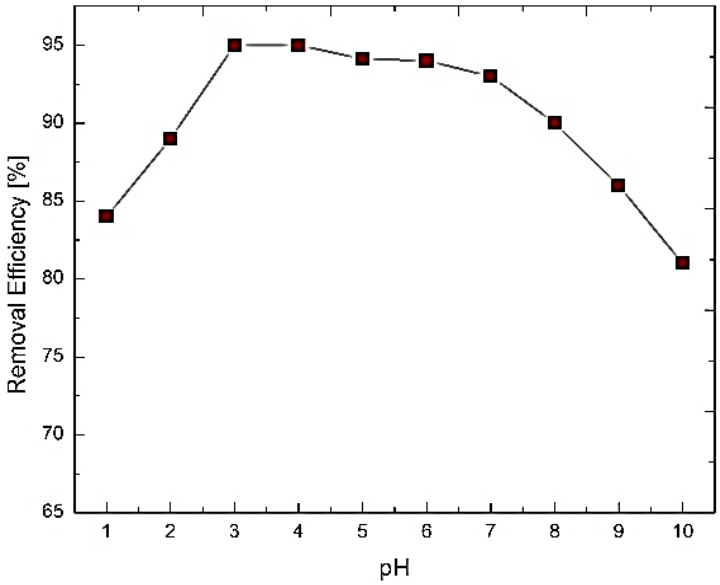

Figure.4.29. Effect of pH versus percentage removal of Cr(VI) by GO-Fe_3O_4 hybrids with initial concentration of 10 mg L^{-1} and adsorbent dose 0.25 g.

4.2.2.3. Adsorption Kinetics

Adsorption of Cr(VI) at different contact times was studied for an initial concentration of 10 mg L^{-1} keeping dose 0.25 g and pH 3-4 to be constant. The result, presented in **Figure.4.30** shows that rate of adsorption of Cr(VI) onto GO-Fe_3O_4 hybrids is very fast as compare to bare magnetite nanoparticles. The adsorption efficiency was found to increase from 31.8 to 95% for a contact time of 5 to 30 min. It is evident from the figure that the Cr(VI) adsorption rate is high at the beginning of the adsorption, this may be due to the adsorption sites are opened and Cr(VI) interact easily with these sites. Cr(VI) uptake becomes almost constant after 30 min; this indicates the possible monolayer formation of Cr(VI) ions on the outer surface and that can be considered as equilibrium time of Cr(VI) adsorption. The observed data proved that the composite material is much more kinetically active than magnetite nanoparticles. The adsorption kinetics were evaluated by fitting experimental data to different kinetic models e.g. pseudo-first-order (**Eq. 3.1**) and pseudo-second-order (**Eq. 3.2**), Elovich (**Eq. 3.3),** Weber-Morris (**Eq. 3.4)**, and Bangham (**Eq. 3.5)**. The amount of the Cr(VI) adsorbed at equilibriums, their respective kinetics constants and related regression coefficients are calculated and summarized in **Table.4.3**.

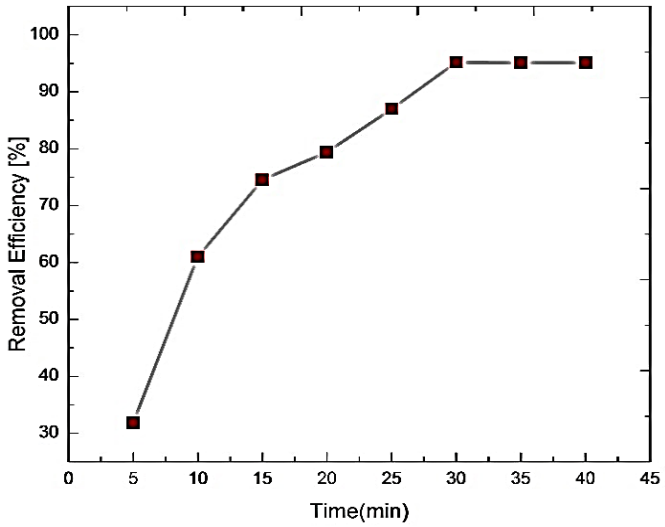

Figure.4.30. Effect of contact time versus %removal of Cr(VI) by GO-Fe_3O_4 hybrids for initial Cr(VI) concentration of 10 mg L^{-1}, adsorbent dose 0.25 g and pH 4.

To understand the order of the adsorption, first the experimental data were tested with pseudo-first-order and pseudo-second-order kinetic models as shown in **Figure.4.31**. The low value of K_{II} (0.023) and high value of R^2 (0.99) indicates that the adsorption completely followed pseudo-second-order kinetics. The second order adsorption capacity and initial adsorption rate were found to be 4.6 mg g^{-1} and 0.48 mg g^{-1} min^{-1}, which is much higher value than Cr(VI)/magnetite system. *Jung WooaLee et al.* has reported a V_0 value of 0.29 mg g^{-1} min^{-1} with 1 mg g^{-1} adsorption capacity for initial Cr(VI) concentration 120 mg L^{-1} by iron nanoparticles decorated on the graphene [159]. An initial adsorption rate 0.30 mg g^{-1} min^{-1} was reported by Jiahua *Zhu et al.* [160] where mesoporous magnetic carbon nanocomposite was used as an adsorbent for Cr(VI) removal. *Yan Liu et al.* found 2.77. mg g^{-1} min^{-1} initial adsorption rate for 300 mg L^{-1} Cr(VI) removal by manganese dioxide/iron oxide/graphene oxide system as adsorbent [161]. The initial adsorption rate for the present system is much better with initial Cr(VI) concentration 10 mg L^{-1} than another system reported in above literature.

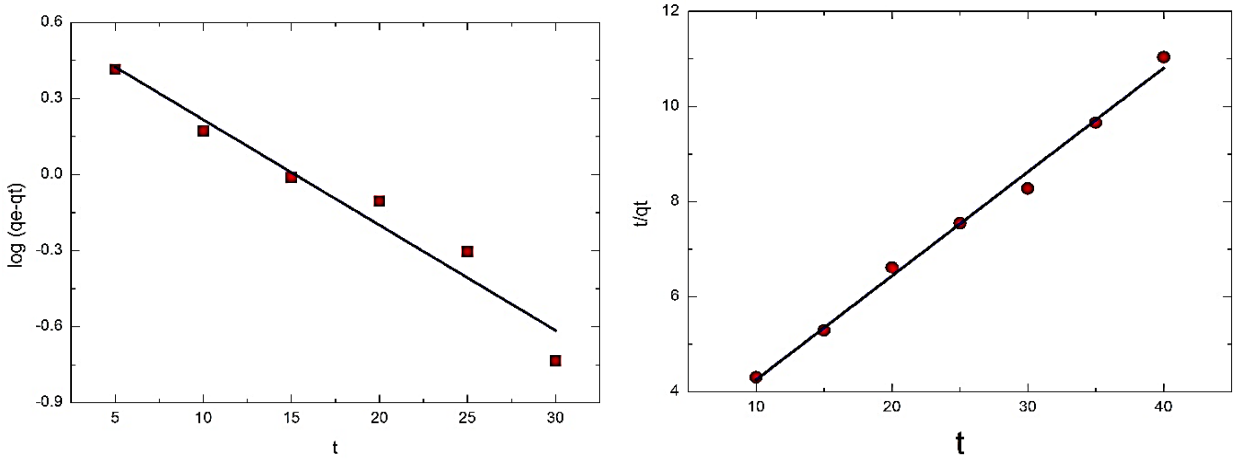

Figure.4.31. Pseudo-first-order model (left) and Pseudo-second-order model (right) for the removal by of Cr(VI) by using GO-Fe_3O_4 hybrids.

Table.4.3. Kinetic parameters for Cr(VI) removal onto GO-Fe_3O_4 hybrids.

Kinetic models	**Parameters**	**Values**
Pseudo-1st Order	R^2	0.943
	K_I (min^{-1})	0.096
	q_e (mg g^{-1})	4.284
Pseudo-2nd Order	R^2	0.99
	K_{II} (g mg^{-1} min^{-1})	0.023
	q_e (mg g^{-1})	4.6
	V_0 (mg g^{-1} min^{-1})	0.48
Elovich	R^2	0.98
	β (mg g^{-1} min^{-1})	0.774
	α (g mg^{-1})	0.55
Weber-Morris	R^2	0.94
	K_{IP} (mg g^{-1} $min^{-1/2}$)	0.699
Bangham	R^2	0.98
	K_B (ml g L^{-1})	61.219
	α	0.985

The overall adsorption kinetics for the Cr(VI) removal was a pseudo-second-order process. However, this could not highlight on the rate-limiting step. Therefore, then the experimental data were analyzed by Elovich model also to understand whether the governing mechanism is diffusion controlled or not. The linear plot of lnt and q_t shows partial fitting with R^2=0.98

shown in **Figure.4.32**. It means transfer of $HCrO_4^-$ oxo anion from the aqueous phase to the adsorbent matrix could be governed by diffusion processes [162].

Surface controlled diffusion process can be derived from the W-M model. The linear plot of q_t and $t^{0.5}$ did not show a a very good fit with regression coefficient of 0.94 (**Figure.4.33**) and not passing through the origin. It means whatever mass transfer occured; it was across the external boundary layer film of liquid surrounding the exterior of the particle. The slope of the linear portion indicates the rate of the adsorption oxo-anions. The lower slope corresponded to a slower sorption process. Poor surface diffusion and slow adsorption after saturation shows there are other rates determining step involved in the adsorption process.

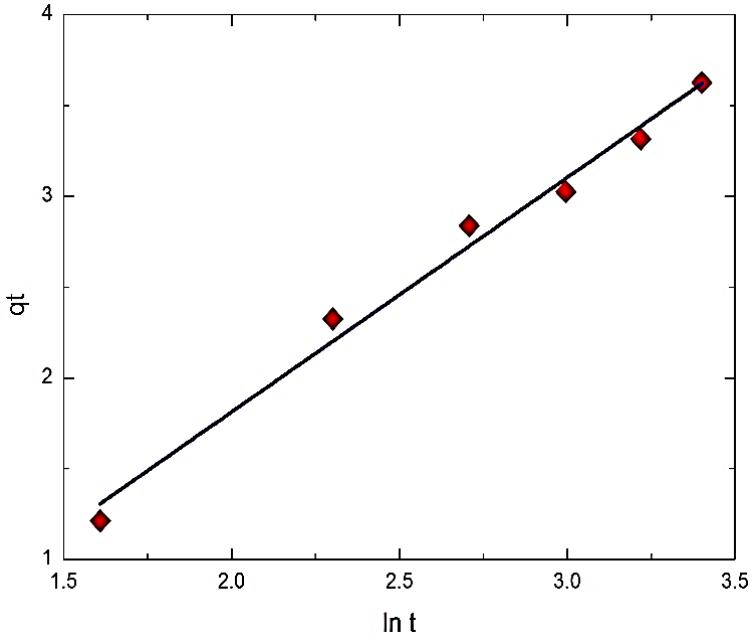

Figure.4.32. Elovich model for the removal of Cr(VI) by using GO-Fe_3O_4 hybrids.

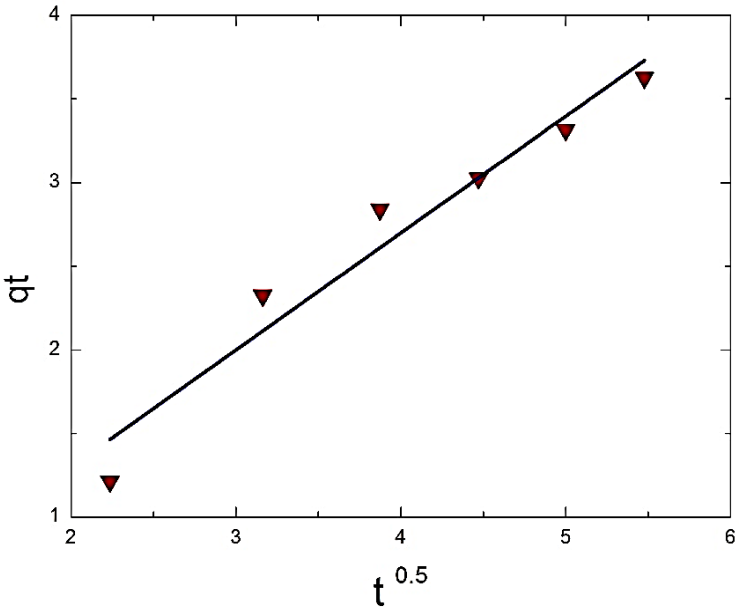

Figure.4.33. Weber- Morris model for the removal of Cr(VI) by using GO-Fe_3O_4 hybrids.

The slow increase in percentage removal after 30 min is attributed to intraparticle diffusion of Cr(VI) into mesopores with the extension of time from 30-40 mins. The pore diffusion controlled mechanism was tested by Bangham model (**Figure.4.34**). The linear fit with R^2=0.98 is a conformation which might be taken as evidence that the rate determining step is controlled by pore diffusion process through the liquid filled pores.

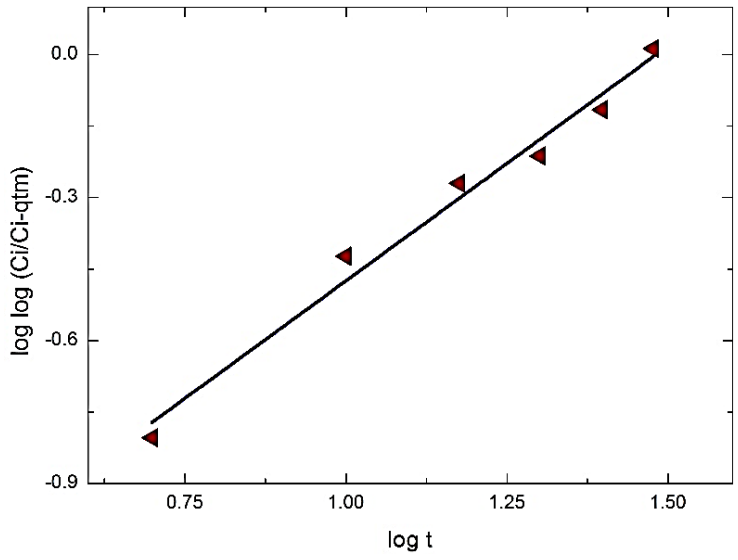

Figure.4.34. Bangham model for the removal of Cr(VI) by using GO-Fe_3O_4 hybrids.

4.2.2.4. Adsorption Isotherms

Batch experiments were performed to investigate the effect of initial chromium concentration on adsorption onto adsorbate. For this experiment the initial concentration of chromium was varied from 10 mg L^{-1} to 100 mg L^{-1} with optimum adsorption dose, time and pH. It is evident from the result that the adsorption efficiency of Cr(VI) decreased from 95.1% to 11.8% for an initial concentration of 10 to 100 mg L^{-1} (**Figure.4.35**). The results indicate that there is a reduction in adsorption, due to the lack of available active sites required for the high concentration of chromium. The higher uptake of chromium at low concentration may be attributed to the availability of more active sites on the surface of the adsorbent for a lesser number of adsorbate species. The various isotherm models, Langmuir (**Eq. 3.6)**, Freundlich (**Eq. 3.9)**, Temkin (**Eq. 3.10)** and Dubinin–Radushkevich (**Eq. 3.12)** essentially correlate the amount of the hexavalent chromium adsorbed at equilibrium (**Table.4.4**).

Table.4.4. Isotherm parameters for Cr(VI) removal onto GO-Fe_3O_4 hybrids.

Isotherm models	**Parameters**	**Values**
Langmuir	R^2	0.96
	q_m (mg g^{-1})	10.23
	K_L (L mg^{-1})	1.49
	ΔG (kJ mol^{-1})	-18.11
	R_L	0.0626
Friendlich	R^2	0.97
	K_F (mg g^{-1})	2.12
	n	4.65
DR	R^2	0.95
	K_{DR}	-0.0003
	q_m (mg g^{-1})	10.63
	E (kJ mol^{-1})	39.24
Temkin	R^2	0.96
	b (J mol^{-1})	1535.45
	K_T (L g^{-1})	36.24

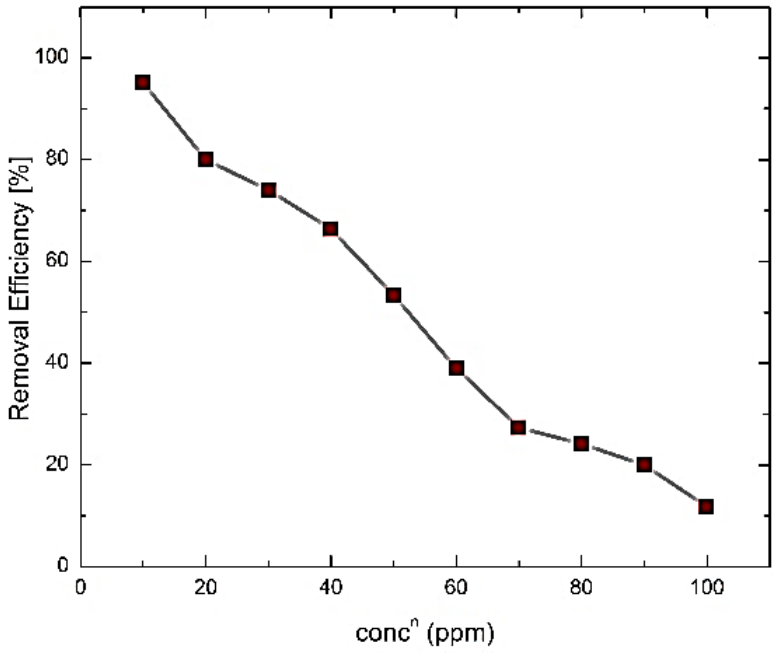

Figure.4.35. Effect of initial Cr(VI) concentration versus %removal of Cr(VI) by GO-Fe_3O_4 hybrids with adsorbent dose 0.25 g, pH 4, room temperature and time 30 min.

The Langmuir plot of $1/q_e$ against $1/C_e$ with higher correlation coefficient, R^2=0.96 indicates the applicability of Langmuir adsorption isotherm shown in **Figure.4.36**. A high Langmuir adsorption capacity of (q_m) and binding energy constant (K_L) of the adsorbent for Cr(VI) was 10.23 mg g^{-1} and 1.49 L mg^{-1} respectively reflects the excellent sorption potential which is valid for monolayer sorption onto a surface with a finite number of identical sites. The -ve free energy parameter, ΔG can be calculated to be -18.11 kJ mol^{-1} is an indication of spontaneity of the process. 21.57 mg g^{-1} maximum capacity for 100 mg L^{-1} chromium concentration by CTAB modified graphene was reported by *Yan Wu et al.* [111]. *Jiahua Zhu et al.* used 1 g L^{-1} Cr(VI) ion concentration and got 1.03 mg g^{-1} capacity for Graphene/Fe@F_2O_3@Si-S-O system [163]. 15.24 mg g^{-1} adsorption capacity was observed for 100 mg L^{-1} concentration by *Vinod K. Gupta et al.* [159] using carbon slurry as an adsorbent system. *Yan Liu et al.* [164]studied on manganese dioxide/iron oxide/graphene oxide for 300 mg L^{-1} with maximum adsorption capacity 175.4 mg g^{-1}. The present system shows a higher Langmuir adsorption capacity of 10.2 mg g^{-1} for a very low concentration of Cr(VI) 10 mg L^{-1}. In order to calculate the

adsorption efficiency of the adsorption process and to know whether the process is favorable or not for the Langmuir type adsorption, the dimensionless equilibrium parameter (R_L), can be calculated using **Eq. 3.8**. The calculated R_L values found in this study was 0.0626 for 10 mg L^{-1} concentration of Cr(VI), representing favorable adsorption process which shows the effectiveness of interaction of the adsorbent with Cr(VI) oxo-anions [165].

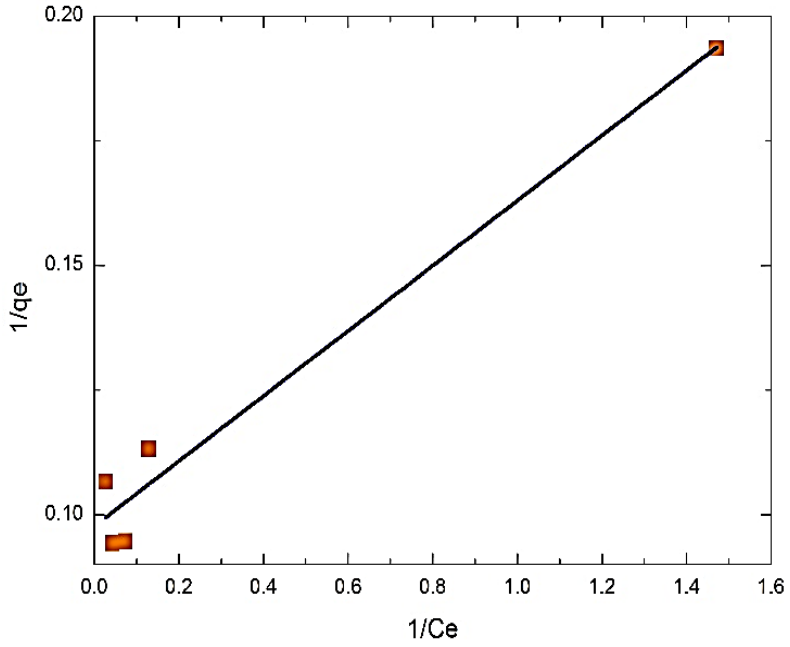

Figure.4.36. Langmuir model for the removal by of Cr(VI) by using GO-Fe_3O_4 hybrids.

The adsorption process on heterogeneous adsorbent was linearized by Freundlich isotherm plot with regression coefficient, R^2=0.97 is shown in **Figure.4.37**. The Freundlich constant, n was calculated from the slope as 4.65 indicates favorable adsorption process.

To understand the interactions between adjacent adsorbate ions Temkin model was taken into consideration. The linear plot of lnC_e and q_e gives regression coefficient 0.96 (**Figure.4.38)**. The energy parameter corresponding to Temkin model also known as heat of adsorption (b) was found out 1.5 kJ mol^{-1}. The high heat of adsorption attributed to chemisorption is the governing mechanism for the Cr(VI) adsorption on GO-Fe_3O_4 hybrids.

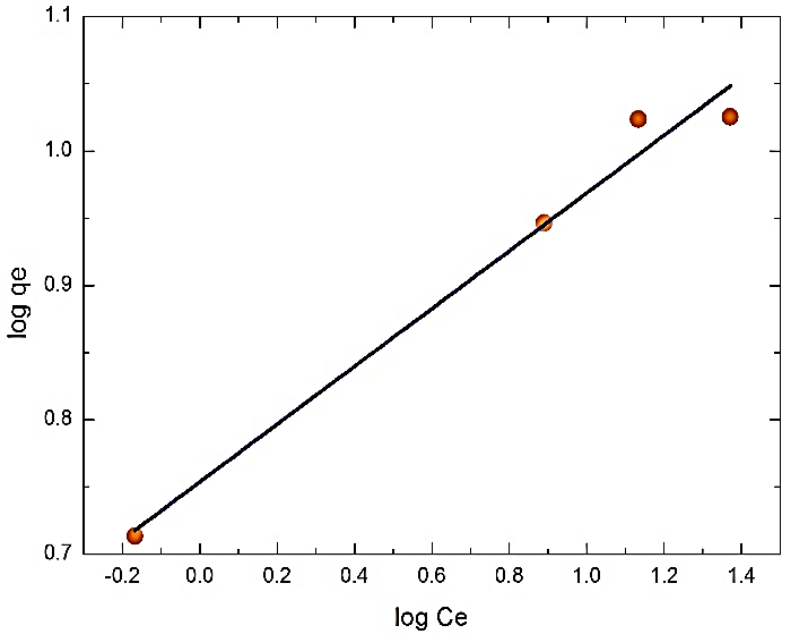

Figure.4.37. Freundlich model for the removal of Cr(VI) by using GO-Fe_3O_4 hybrids.

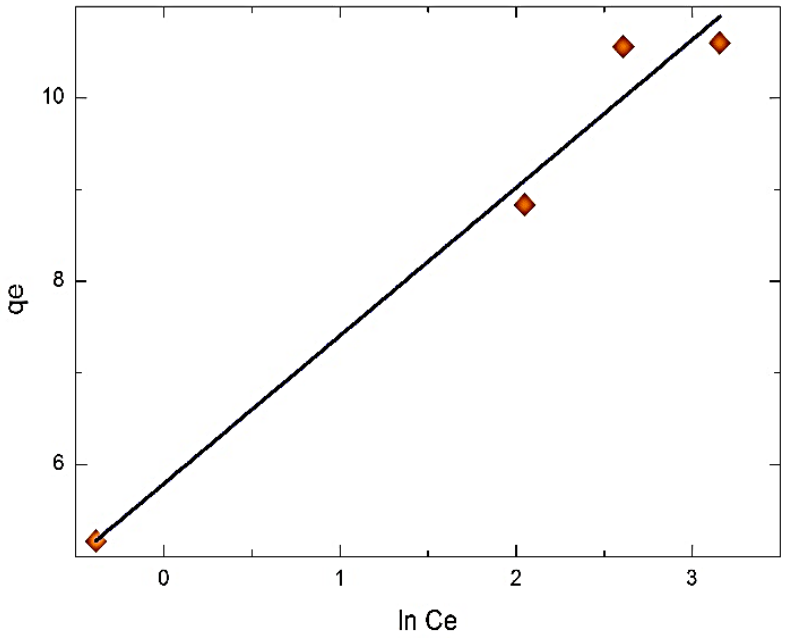

Figure.4.38. Temkin model for the removal of Cr(VI) by using GO-Fe_3O_4 hybrids.

Involvement of pores in the isotherm mechanism can be described by D-R model. The value of R^2 to be 0.95 for D-R model showed a poor fitting for this system (**Figure.4.39)**. But the mean sorption energy (E) is found to be 39.24 kJ mol^{-1}.

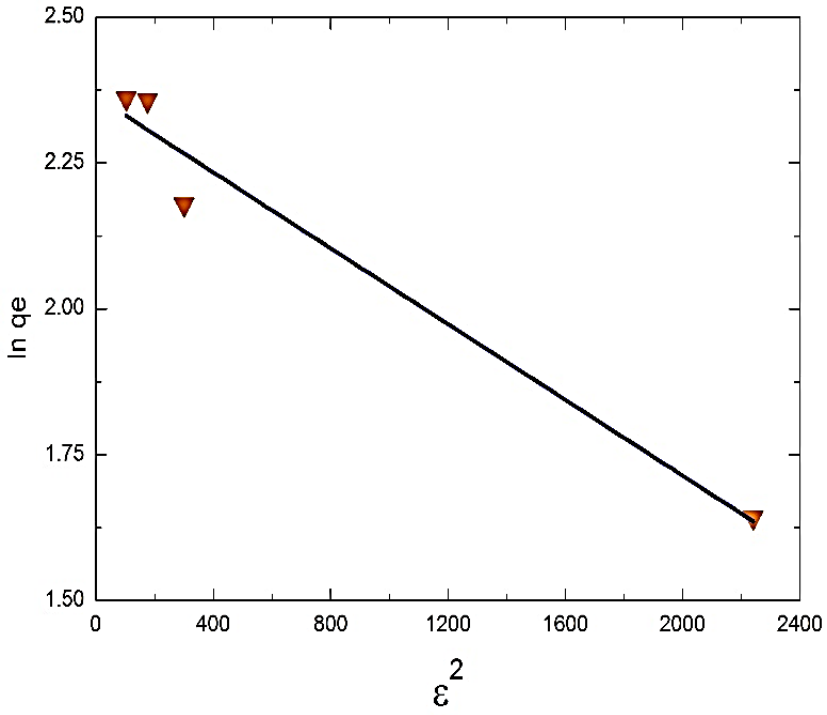

Figure.4.39. Dubinin–Radushkevich model for the removal of Cr(VI) by using GO-Fe_3O_4 hybrids.

4.2.2.5. Mechanism of Desorption

Regeneration studies give an idea about the nature of adsorption. Chemisorption exhibits poor desorption; it may be due to the fact that in chemisorption the adsorbate species are held to adsorbent with comparatively stronger bonds. In any adsorption process, the economics of the entire operation is quite important and in this perspective the regeneration of the adsorbent is also an important parameter [24]. The desorption mechanism of the metal ions onto the adsorbent surface strongly depend on the pH of the solution, shown in **Figure.4.40** respectively. In this process different pH (2-12) of the solution was selected by using 0.1M HCl and 0.1M NH_4OH as an eluent to desorb the metal ions from loaded adsorbent.

In the adsorption process, the percentage of hexavalent chromium ions adsorption onto the GO-Fe_3O_4 hybrids was found to be ~95% between pH 3-4 (acidic medium). At pH < 3, the

adsorbent surface has high positive charge density due to excess [H^+]. Hence under these conditions the adsorption of Cr(VI) oxo-anions would be high due to electrostatic attraction. With increasing pH (pH > 4), the charge density on the adsorbent surface become negative, thereby resulting in a sudden decrease in Cr(VI) oxo-anions adsorption due to electrostatic repulsion. But under basic conditions, the process of desorption predominates over the process of adsorption. The desorption of Cr(VI) ions calculated (**Eq. 4.1)** from the loaded adsorbent surface was found to be ~92% at pH 10.

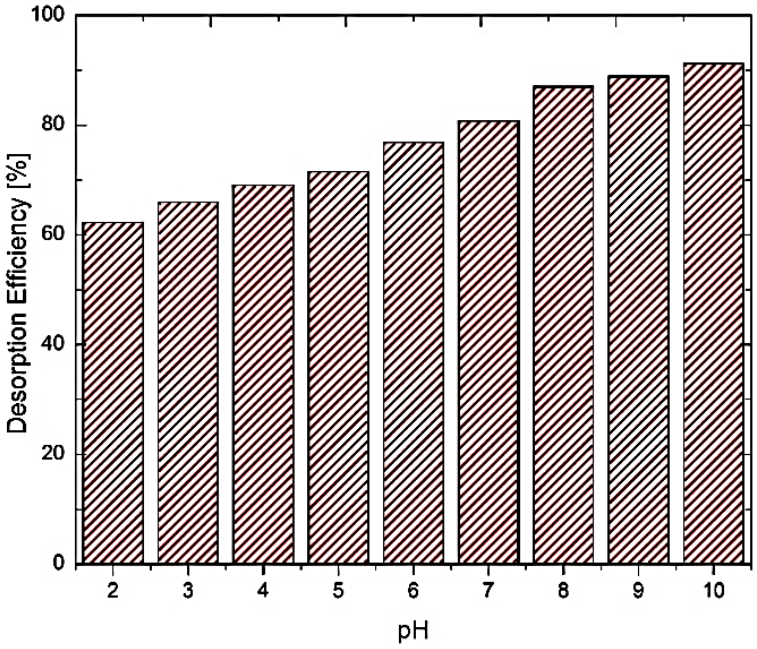

Figure.4.40. %desorption of Cr(VI) from GO-Fe_3O_4 hybrids as a function of pH.

4.2.2.6. Characterization of hybrid after adsorption Cr(VI)

Since, some form of interaction between Cr(VI) ions with the Fe_3O_4 nanoparticles surface was expected, it was considered appropriate to conduct XRD scan of the Cr(VI) adsorbed GO-Fe_3O_4 hybrids. Both the XRD patterns of the hybrid before and after Cr(VI) adsorption were almost similar, although some subtle differences can be observed **Figure.4.41**. The XRD pattern of the hybrid after Cr(VI) adsorption had slightly broader peaks. It can be easily observed from the most intense (311) peak. Additionally, the peak intensity was also found to

be slightly reduced as compared to that of the unused GO-Fe_3O_4 hybrid. A logical explanation to this observation could be that Cr(VI) adsorbed onto the surface of the Fe_3O_4 nanoparticles, thus affecting its crystallinity. As a result some form of surface amorphization of the Fe_3O_4 nanoparticles might occur. The XRD signal, therefore, could have come from the crystalline core of the Fe_3O_4 phase [145].

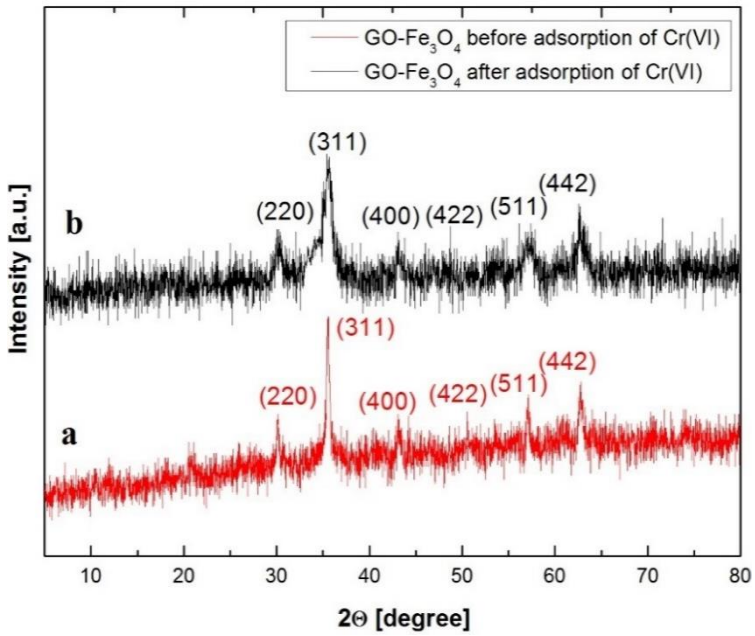

Figure.4.41. XRD patterns of GO-Fe_3O_4 hybrid (a) before and (b) after adsorption of Cr(VI).

The surface elements distribution of GO-Fe_3O_4 hybrid adsorbent after adsorption of Cr(VI) was studied by EDX shown in **(Figure.4.42)**. It could also be substantiated that the adsorption of Cr(VI) from the EDX spectrum in addition to other elements such as Fe, C and O. The appearance of two peaks in the energy range of 5-6 keV in the EDX spectra of adsorbent after adsorption were characteristic of Cr(VI) reported earlier in literatures [145, 146].

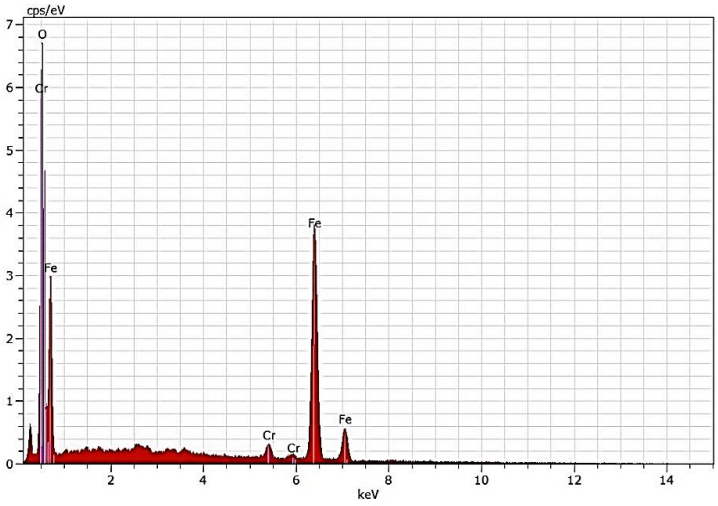

Figure.4.42. EDX spectra of GO-Fe_3O_4 hybrid after adsorption of Cr(VI).

The FTIR spectroscopy of the hybrids before and after Cr(VI) adsorption provided substantial evidence for effective adsorption of the toxins. In the pH range (3-4), the hydroxyl groups in the adsorbent could be protonated and these positively charged surface hydroxy groups could also interact with the hydro chromate anion ($HCrO_4^-$). After adsorption of chromium(VI), two new peaks appeared at 874 cm^{-1} and 770 cm^{-1} characteristics of Cr=O and Cr–O stretching frequencies in the hydrochromate anion respectively [147-150] (**Figure.4.43**).

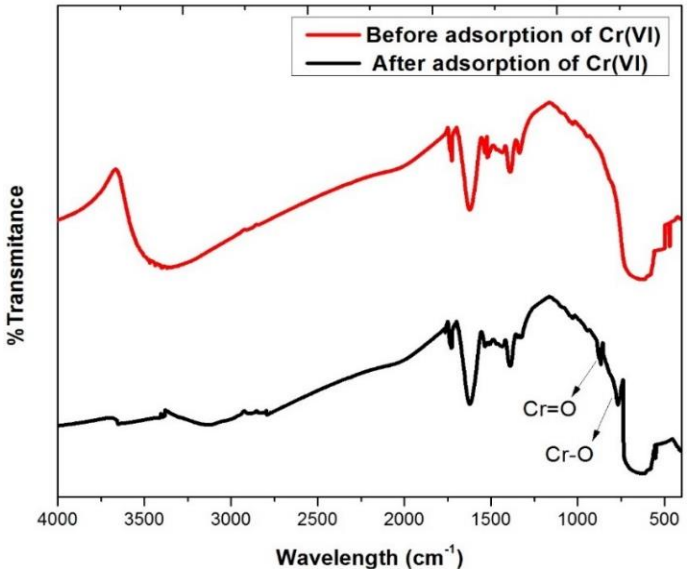

Figure.4.43. FTIR spectra of GO-Fe_3O_4 hybrid before and after adsorption of Cr(VI).

4.2.3. ADSORPTION STUDIES OF MALACHITE GREEN BY GO-Fe_3O_4 HYBRIDS

4.2.3.1. Effect of Adsorbent Dose

Effect of adsorbent doses on the adsorption of malachite green in aqueous solution was performed by varying the GO-Fe_3O_4 hybrids doses from 0.005 g to 0.012 g shown in **Figure.4.44**. The doses are added to a series of 100 mL dye solutions of 10 mg L^{-1} concentration at room temperature and neutral pH under stirring. The graph shows that the adsorption efficiency increases with adsorbent dose due to higher number of available active binding sites for cations in solution. The adsorption efficiency increases up to 97.6% for a very low amount of adsorbent dose of 0.01 g and then no significant changes in adsorption efficiency was observed on increasing the doses due to overlapping of active sites leading to agglomeration of nano particles. So, the optimum dose for malachite green removal was considered to be 0.011 g of GO-Fe_3O_4 hybrids. The above data manifested that the composite material is more practicable for dyes. Besides, the GO sheets also have delocalized π-electrons that act as basic sites providing the ability to bind cations.

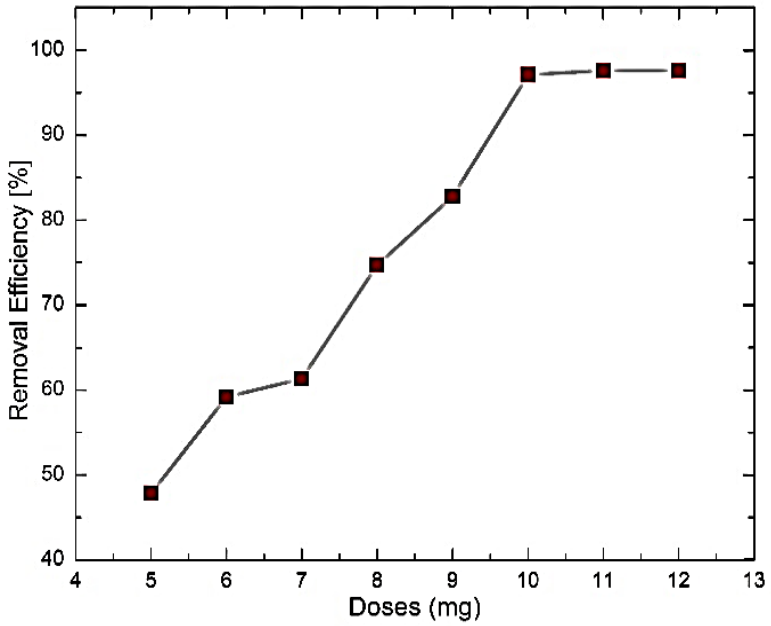

Figure.4.44. Effect of adsorbent doses versus %removal of malachite green on GO-Fe_3O_4 hybrids with an initial dye concentration of 10 mg L^{-1}, at room temperature and neutral pH.

4.2.3.2. Effect of pH and Mechanism of Adsorption

The effect of pH on adsorption and possible interactions of GO-Fe_3O_4 hybrids with dye molecules were further studied by varying the pH from 2 to 11, initial dye concentration of 10 mg L^{-1} and adsorbent dose 0.01 g. pH of the solution was adjusted by adding a suitable volume of HCl (0.1M) and NaOH (0.1M). The role of pH is important in a solution containing ions as it affects the electrostatic interaction between adsorbent and adsorbate (cationic). A plot of %removal and pH clearly revealed that adsorption efficiency increases up to 97.6% with increase in pH and then decreases (**Figure.4.46**). The effect of pH on adsorbent surface is well discussed before for Cr(VI)/GO-Fe_3O_4 hybrid system. Lower pH leads to protonation of adsorbent surface, therefore, adsorption efficiency is low due to electrostatic repulsion of the cationic dye molecules with the adsorbent surface. Increase in pH increases the negative charges with slow deprotonation of surface groups associated with the GO-Fe_3O_4 hybrid, thus, increasing the electrostatic interactions with cationic dye. All possible interactions of malachite green onto GO-Fe_3O_4 hybrid is represented in **Figure.4.45**. But after pH > 8 the there is adecrease in adsorption efficiency because of higher [OH^-] which complete with the adsorbate ions. So, adsorption efficiency increases up to 97.6% considering pH-8 to be the optimum pH for adsorption of malachite green.

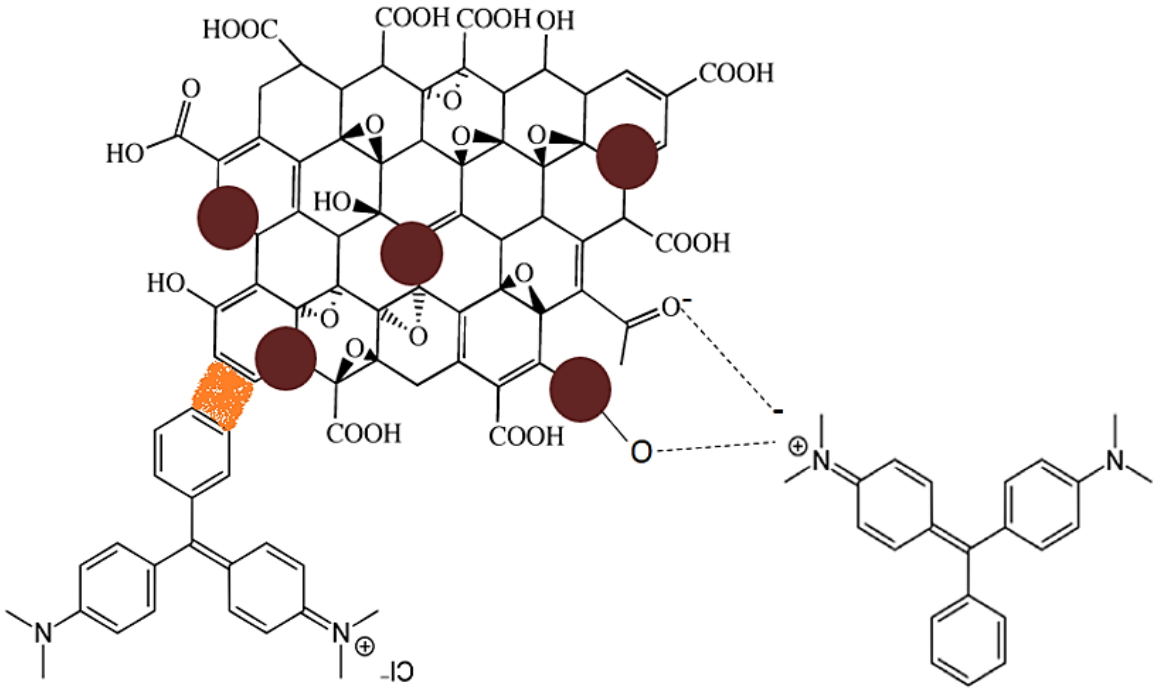

Figure.4.45. Possible interactions of malachite green dye with GO-Fe_3O_4 hybrid.

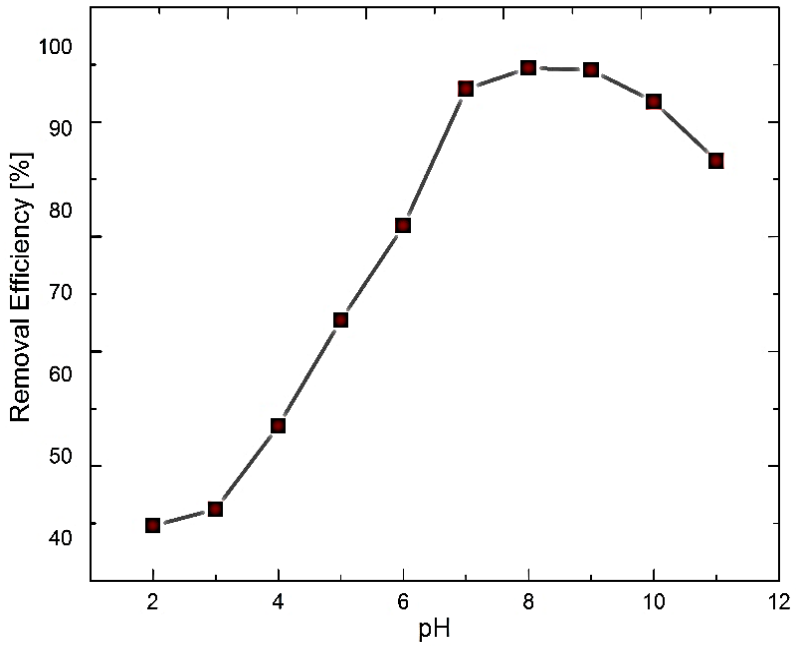

Figure.4.46. Effect of pH versus %removal of malachite green by GO-Fe_3O_4 hybrid for initial dye concentration of 10 mg L^{-1} and adsorbent dose 0.011 g.

4.2.3.3. Adsorption Kinetics

Effect of contact time on adsorption was studied to investigate the rate and kinetics for adsorption of cationic dye on GO-Fe_3O_4 hybrids. The batch experiments were carried out by varying the time period from 10-80 mins for an initial concentration dye to be 10 mg L^{-1}, pH-8 and dose (0.011 g). It is observed from the %removal versus time graph that adsorption efficiency increases with contact time for malachite green (cationic dye). The graph (**Figure.4.47)** shows two kind of behaviors, at initial time periods from 10-60 mins the slope of the graph is high which later gets almost constant values up to 80 mins. It suggested that initially the rate of binding is high because of higher numbers of open active sites get saturated with increasing time. The high slope of the graph suggested the high rate of adsorption of malachite green on to kinetically active GO-Fe_3O_4 hybrids material.

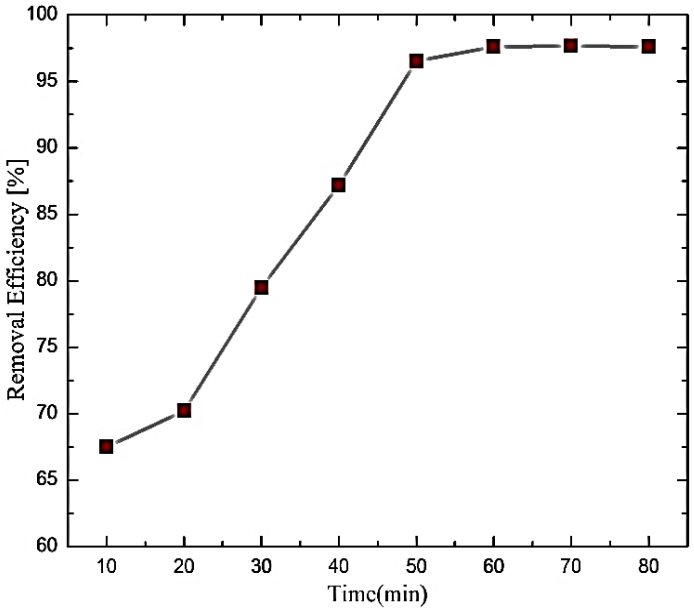

Figure.4.47. Effect of adsorption time versus %removal of malachite green by GO-Fe_3O_4 hybrids for initial dye concentration of 10 mg L^{-1}, adsorbent dose 0.011 g and pH-8.

The adsorption kinetics for the removal of malachite green were investigated by correlating the experimental data to pseudo-first-order (**Eq. 3.1**), pseudo-second-order (**Eq. 3.2**), Elovich (**Eq.**

3.3), Weber-Morris (**Eq. 3.4)** and Bangham (**Eq. 3.5)** models. The corresponding calculated kinetic parameters are summarized (**Table.4.5**).

Table.4.5. Kinetic parameters for malachite green removal onto GO-Fe_3O_4 hybrids.

Kinetic models	**Parameters**	**Values**
Pseudo-1st Order	R^2	0.72
	K_I (min^{-1})	0.175
	q_e (mg g^{-1})	918.54
Pseudo-2nd Order	R^2	0.97
	K_{II} (g mg^{-1} min^{-1})	0.00009
	q_e (mg g^{-1})	102.67
	V_0 (mg g^{-1} min^{-1})	9.7
Elovich	R^2	0.82
	β (mg g^{-1} min^{-1})	0.06
	α (g mg^{-1})	2.925
Weber-Morris	R^2	0.94
	K_{IP} (mg g^{-1} $min^{-1/2}$)	6.775
Bangham	R^2	0.78
	K_B (ml g L^{-1})	50.67
	α	0.503

The pseudo first-order model was plotted between $\log(q_e-q_t)$ versus t, that give a linear relationship. But it was observed that the adsorption of cationic dye to GO-Fe_3O_4 hybrids fits well to pseudo-second-order model with higher R^2 value 0.97 (**Figure.4.48)** than pseudo-first-order (R^2=0.72). Equilibrium adsorption capacity (q_e) and pseudo-second order constant (K_{II}) could be calculated form the slope and intercept of the obtained straight line respectively. The second order adsorption capacity was found to be 102.7 mg g^{-1}. The initial adsorption rate of malachite green on GO-Fe_3O_4 hybrids was calculated to be 9.7 mg g^{-1} min^{-1}, suggesting a much higher and faster kinetics than other, Cr(VI)/magnetite and Cr(VI)/GO-Fe_3O_4 systems.

The lower value of K_{II} (0.0009 g mg^{-1} min^{-1}) shows the applicability of the second-order model to describe and interpret the experimental data better. *Rashmi Rani Mishra, et al.* [166] investigated the initial adsorption rate of citrate-stabilized magnetite particles to be 6.751 mg g^{-1} min^{-1} to remove malachite green with a maximum capacity 0.489 mg g^{-1}. Utilization of oxidized-activated form of hydrothermally carbonized pine needles (HTC-APN) was reported

by *Hassan H. Hammud et al.* [167] showing adsorption capacity and rate to be 24.15 mg g^{-1} and 3.12 mg g^{-1} min^{-1} respectively. In a very interesting study by *Sozia Ahad et al.* [168],5-sulphosalicylic acid doped tetra-ethoxysilane (SATEOS) as an adsorbent showed an equilibrium capacity 4.81 mg g-1and initial adsorption rate 2.128 mg g^{-1} min^{-1}. *Hongmei Sun et al.* [169] reported an initial rate of 1.35 mg g^{-1} min^{-1} for magnetite-RGO at adsorption capacity 6.47 mg g^{-1}. The hybrid material found to possess ultrafast adsorption rate and capacity than the above literatures.

In addition to the applicability of the pseudo-second-order kinetic model, the diffusion model was also found to be slightly applicable to explain the experimental data with regression coefficient 0.82. The bad linear fit of Elovich model is shown in **Figure.4.49**.

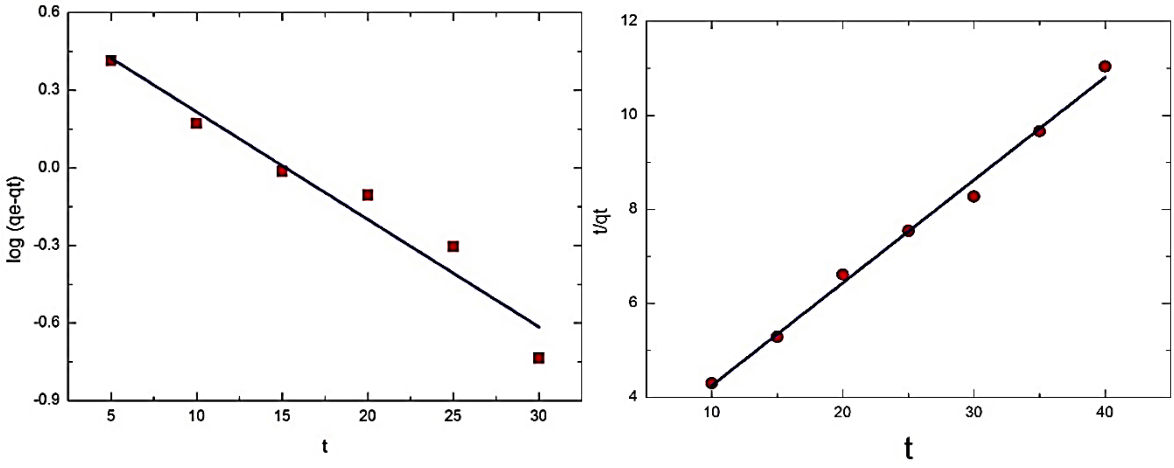

Figure.4.48. Pseudo-first-order model (left) and Pseudo-second-order model (right) for the removal of malachite green by GO-Fe_3O_4 hybrids.

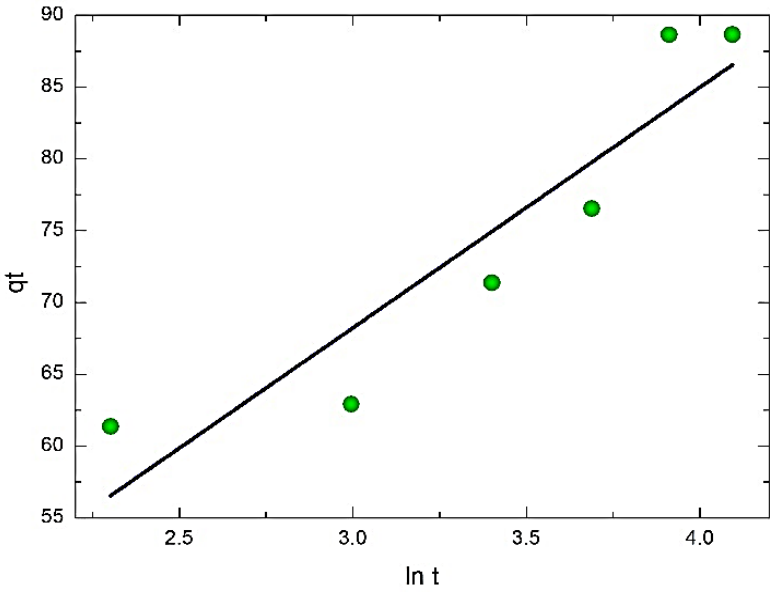

Figure.4.49. Elovich model for the removal of malachite green by GO-Fe_3O_4 hybrids.

Information regarding various intraparticle diffusion processes included were analyzed by partially fitted W-M model with R^2=0.94 (**Figure.4.50)**. It is evident from behavior of the linear plot of W-M model that the mechanism followed surface diffusion and since, the curve did not pass through the origin; it is noticed that in addition to the surface diffusion another stage such as boundary acts to control the adsorption process too. Also, the higher value of K_{IP} (6.775) from W-M model signifies no internal diffusion of adsorbate. A very bad fitting of Bangham plot, the pore diffusion controlled model showing R^2 of 0.78 (**Figure.4.51)** ascribed the adsorption of malachite green on to composite material is not diffusion controlled due its complex aromatic structure. The best followed mechanism is pseudo-second-order kinetics and partly intraparticle diffusion acts to control the adsorption process.

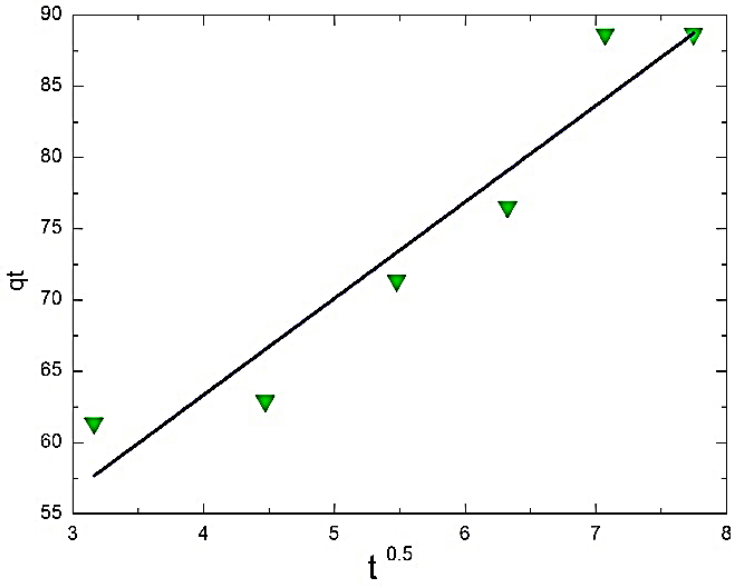

Figure.4.50. Weber-Morris model for the removal of malachite green by GO-Fe_3O_4 hybrids.

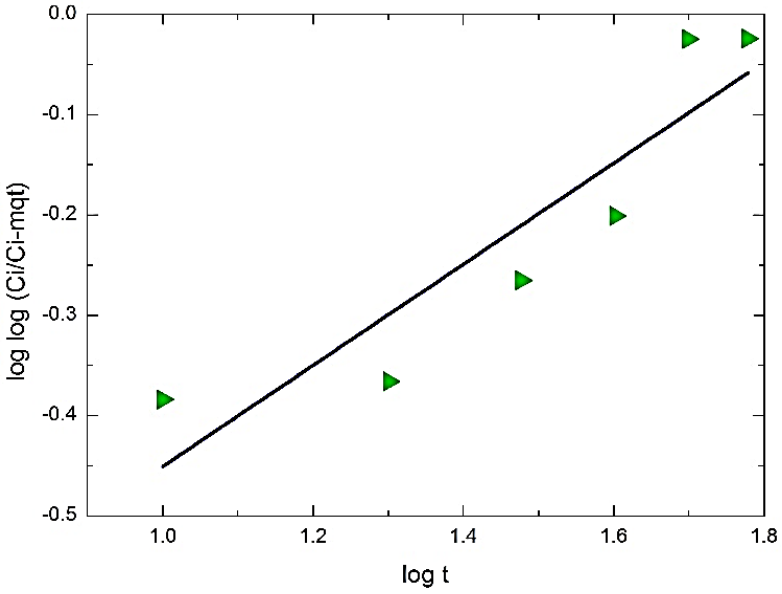

Figure.4.51. Bangham model for the removal of malachite green by GO-Fe_3O_4 hybrids.

4.2.3.4. Adsorption Isotherms

Effect of initial dye (malachite green) concentration on adsorption was performed by varying the dye concentration from 10 mg L^{-1} to 60 mg L^{-1} keeping other parameters constant. The result shows that adsorption efficiency decreasing with increasing the dye concentration (**Figure.4.52)**. This simple adsorption behavior for cationic dye was assumed to be homogeneous.

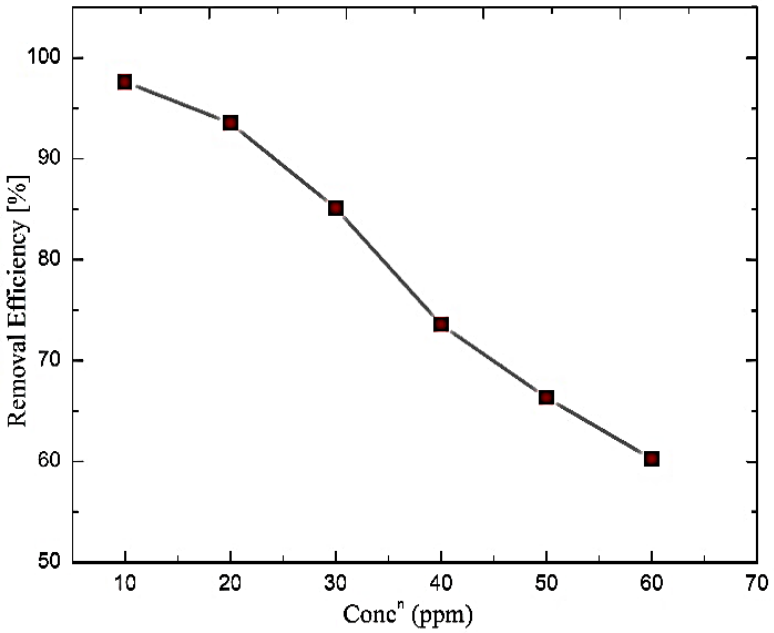

Figure.4.52. Effect of initial dye concentration versus %removal of malachite green by GO-Fe_3O_4 hybrids with adsorbent dose 0.011 g, pH 8, room temperature and time 60 mins.

Whether the adsorption takes place on homogeneous surface or heterogeneous surface can be further proved by isotherm modelling. The experimental data were fitted to Langmuir (**Eq. 3.6)**, Freundlich (**Eq. 3.9)**, Temkin (**Eq. 3.10)** and Dubinin–Radushkevich (**Eq. 3.12)** models. All the constant parameters and correlation coefficients (R^2) corroborated from the plots of known equations for all models are summarized in **Table.4.6**.

Table.4.6. Isotherm parameters for malachite green removal onto GO-Fe_3O_4 hybrids.

Isotherm models	Parameters	Values
Langmuir	R^2	0.98
	q_m (mg g^{-1})	288.2
	K_L (L mg^{-1})	2.103
	ΔG (kJ mol^{-1})	-18.957
	R_L	0.045
Frieundlich	R^2	0.94
	K_F (mg g^{-1})	157.01
	n	3.75
DR	R^2	0.98
	K_{DR}	-0.0002
	q_m (mg g^{-1})	304.95
	E (kJ mol^{-1})	41.76
Temkin	R^2	0.99
	b (J mol^{-1})	49.477
	K_T (L g^{-1})	31.586

Based on the linear plot of Langmuir model (**Figure.4.53**), the values of Langmuir constant (K_L) and maximum monolayer capacity (q_m) were obtained from the intercept and slope of the plot. A correlation coefficient of 0.98 shows the moderate applicability of the model for the interpretation of the experimental data. The maximum monolayer adsorption capacity was found to be 288.2 mg g^{-1}. α-Fe_2O_3–rGO showed maximum adsorption capacity of 438.8 mg g^{-1} for initial malachite green concentration 75 mg L^{-1} by *Airong Liu et al.* [170]. Similarly, 89.3 mg g^{-1} of monolayer capacity was derived from Activated carbon/$CoFe_2O_4$ composite as an adsorbent for 100 mg L^{-1} dye solution by *Lunhong Ai et al.* [171]. *Hongmei Sun et al.* reported maximum capacity 22 mg g^{-1} for 0.7 g L^{-1} of dye solution by magnetite-RGO [169]. Maximum adsorption capacity of malachite green for the present system is found to be better than above reported systems. Furthermore, the Langmuir constant (K_L), related to free energy of adsorption (ΔG) found to be -18.957 kJ mol^{-1} shows the process is spontaneous and dimensionless equilibrium parameter R_L can be found out 0.045 for 10 mg L^{-1} dye concentration. This represents the adsorption of cationic dye on GO-Fe_3O_4 hybrids is favorable.

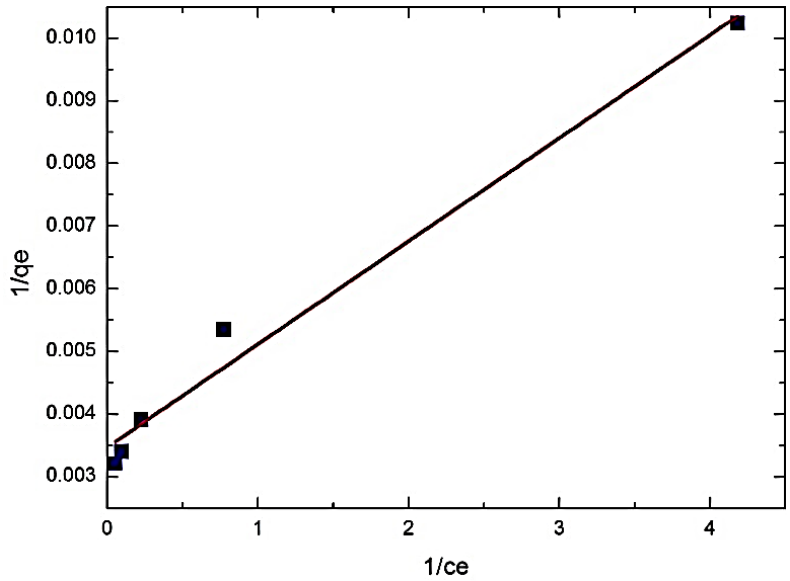

Figure.4.53. Langmuir model for the removal of malachite green by GO-Fe_3O_4 hybrids.

Parameters of the Freundlich isotherm model such as K_F and n were calculated from the intercept and slope of the linear plot of lnq_e versus lnC_e, respectively (**Figure.4.54**). The value of n (3.75) for this system shows the favorable adsorption of malachite green onto GO-Fe_3O_4 hybrids while the lower R^2 value of 0.94 shows its moderate suitability for fitting the experimental data. It means slight multilayer formation due to π-π staking interaction between aromatic part of cationic dye and delocalized π-electron system of graphene oxide [71].

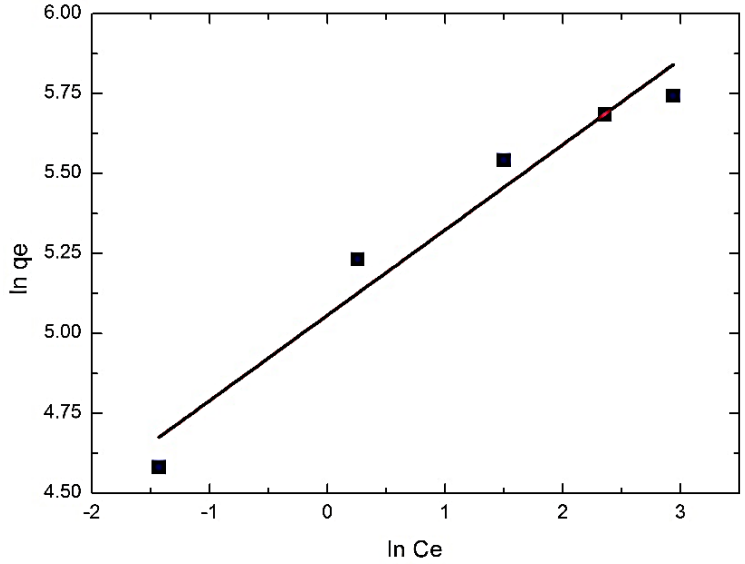

Figure.4.54. Freundlich model for the removal of malachite green by GO-Fe_3O_4 hybrids.

The heat of adsorption (b) for adsorbent–adsorbate interactions and its uniform distribution of binding energy were evaluated by Temkin model. The linear plot of q_e versus ln C_e represented the best fit with highest R^2 value of 0.99 (**Figure.4.55)**. The value of heat of adsorption was found 49.47 J mol^{-1}, which is an indication of physical adsorption. Therefore, the mechanism of adsorption of malachite green onto GO-Fe_3O_4 hybrids completely followed by Temkin model showing physisorption.

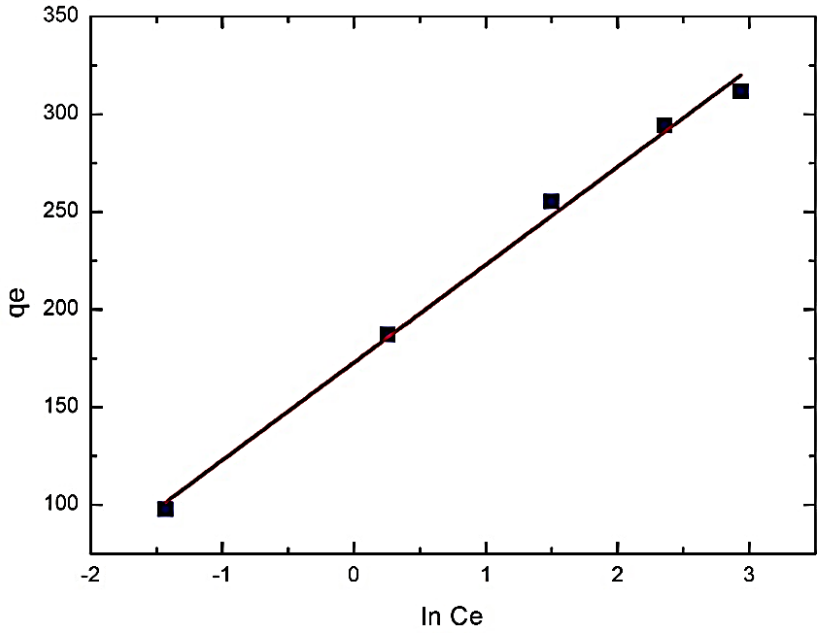

Figure.4.55. Temkin model for the removal of malachite green by GO-Fe_3O_4 hybrids.

To estimate the apparent porosity free energy adsorption isotherm, data were tested by D–R model. The characteristics of adsorption mechanism for this system seems to be partially governed by the linear D-R fit with R^2 value of 0.98 (**Figure.4.56)**. But the mean sorption energy (E) calculated was too high (41.76 kJ mol^{-1}), which means the free energy change when one mole of ion is transferred from the solution to the surface of the sorbent is not an acceptable for this system.

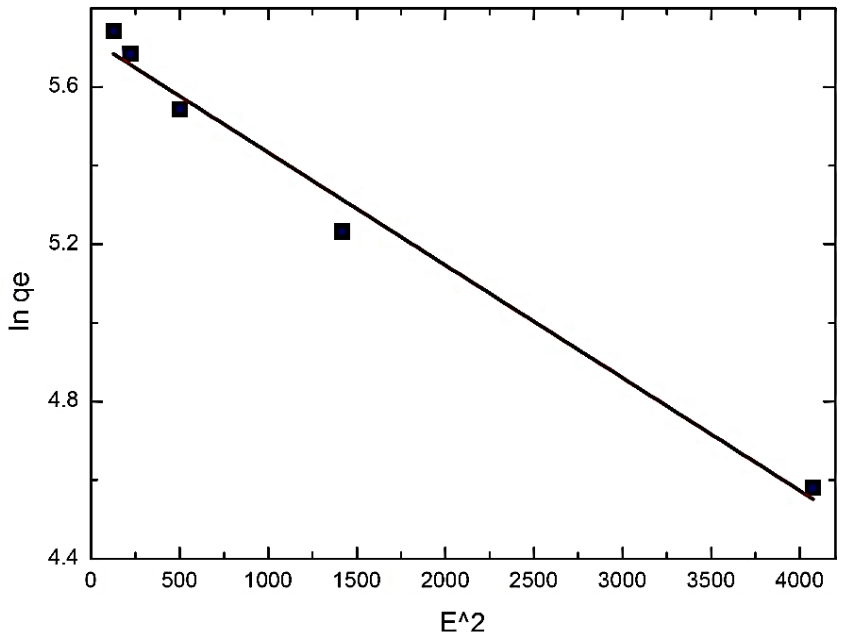

Figure.4.56. D-R model for the removal of malachite green by GO-Fe_3O_4 hybrids.

4.2.3.5. Mechanism of Desorption

The mechanism of desorption as a function of solution pH is investigated using 0.1M HCl and 0.1M NaOH. These used eluents are cost effective and does not harm the adsorbent bed. Adsorption mechanism of malachite green (cationic dye) onto GO-Fe_3O_4 hybrids was favorable at higher pH-8 as illustrated**.** But the process of desorption of cationic dye is seen to be maximum at lower pH. Therefore, a graph with decreasing %desorption with increase in pH is shown in **Figure.4.57**. At lower pH desorption predominance over the adsorption of the malachite green on GO-Fe_3O_4 hybrids. This perhaps due to electrostatic repulsion caused by surface protonation of the composite material with dye cations. The maximum desorption efficiency is calculated from **Eq. 4.2** to be 93.3% at pH-2.

$$\text{Desorption Efficiency (\%)} = \frac{\text{Concentration of dye desorbed into the solution}}{\text{Concentration of dye adsorbed onto the adsorbent}} \times 100 \qquad \textbf{Eq. 4.2}$$

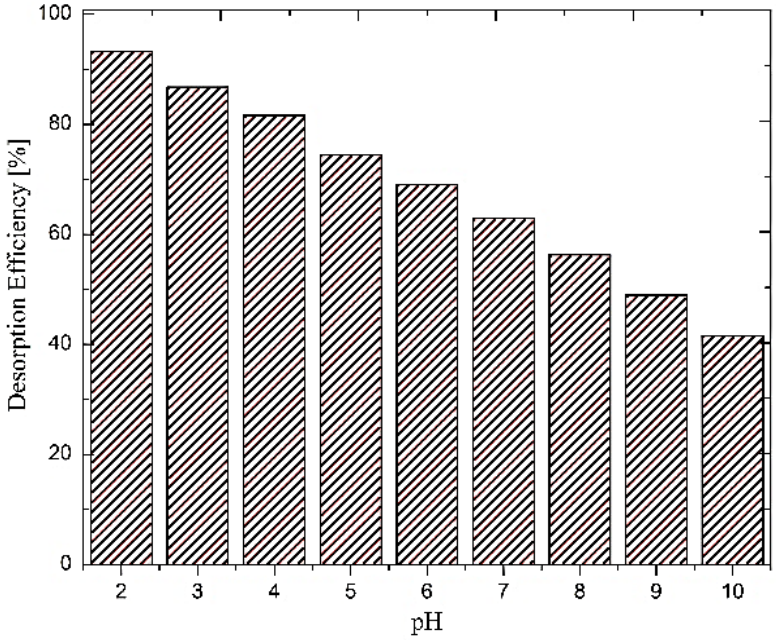

Figure.4.57. %desorption of malachite green from GO-Fe_3O_4 hybrids as a function of pH.

4.2.4. ADSORPTION STUDIES OF PHENOL RED BY GO-Fe_3O_4 HYBRIDS

4.2.4.1. Effect of Adsorbent Dose

This batch experiment was carried with a series of bottles containing 100 mL of phenol red solutions of concentration 10 mg L^{-1} varying the doses from 0.005 to 0.012 g at room temperature and neutral pH. The results of the effect of adsorbent doses on adsorption capacity are illustrated in **Figure.4.58**. An increasing trend in adsorption efficiency with respect to adsorbent dose is seen from the graph. Increasing doses lead to more numbers of active sites which gradually overlap for higher doses [172]. Hence, the adsorption efficiency increases from 39.13% to 67.8% and then remain almost constant. As phenol red carries both the charges which effect of electrostatic interaction, the adsorption efficiency is not so high for the same amount of adsorbent dose used before for malachite green (cationic dye).

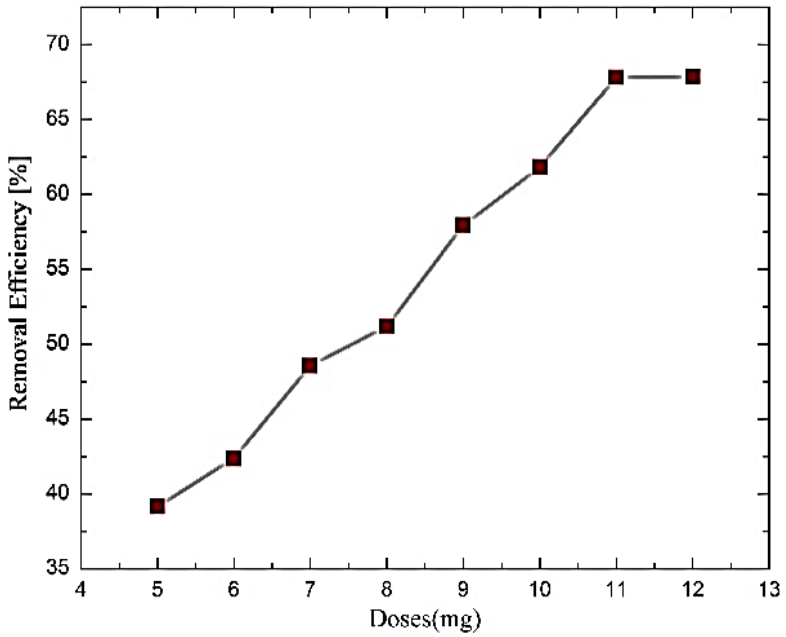

Figure.4.58. Effect of adsorbent dose versus %removal of phenol red by GO-Fe_3O_4 hybrids for initial dye concentration 10 mg L^{-1}, room temperature and neutral pH.

4.2.4.2. Effect of pH and Mechanism of Adsorption

Effect of pH plays a significant role in adsorption mechanism of phenol red (neutral dye) on GO-Fe_3O_4 hybrids as it contains both the charges. Before going to the adsorption efficiency lets us discuss interesting chemistry of phenol red as a function of pH. In solution phase under very acidic conditions phenol red molecule attains the zwitterion form with two functional groups, a negatively charged sulfate group and a positively charged ketone group with an additional proton. If the pH of the solution is increased the pK_a value also increases and the proton from the ketone group is lost resulting the dye molecule to be negatively charged. If the pH is further increased to higher basic level phenol' hydroxyl loses its proton leading an extra negative charge. As the charge on the dye molecule is a function of pH, it will definitely effect the electrostatic interaction between the dye molecules and adsorbent surface hence the adsorption efficiency also.

The batch experiments were studied by varying the pH of the solution from 2-11 for an adsorbent dose of 0.011 g, initial dye concentration 10 mg L^{-1} at room temperature. The decrease in adsorption efficiency of phenol red as a function of pH variation is given in **Figure.4.59**. The prepared GO-Fe_3O_4 hybrids contain various functional groups which get protonated (+ve) at very low pH and as discussed before the dye molecules also acquire both the charges (+ve and –ve) at very low pH. Therefore, a maximum adsorption of 67.8% is possible at pH-3 due to electrostatic attraction between negatively charged protonated groups and positive charge in zwitterion. At higher pH the composite surface becomes more and more negative due to presence of higher [OH^-]. So, at basic medium, there is electrostatic repulsion between negative adsorbent surface and negatively charged dye molecule leads to decrease in adsorption efficiency. This proves that the adsorption of neutral dye works well in acidic condition for GO-Fe_3O_4 hybrids. All possible interactions of phenol red molecules with GO-Fe_3O_4 hybrids is shown in **Figure.4.60**.

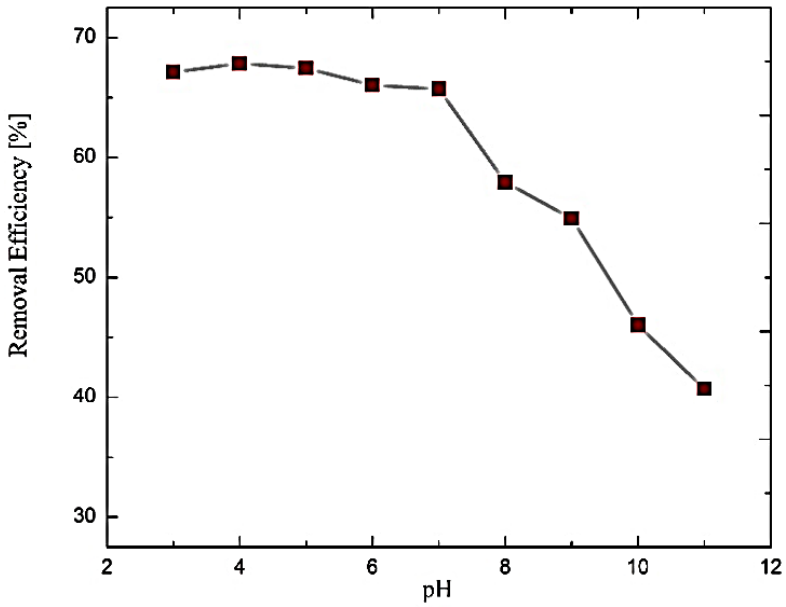

Figure.4.59. Effect of pH versus %removal of phenol red by GO-Fe_3O_4 hybrids with initial concentration of 10 mg L^{-1} and adsorbent dose 0.011 g.

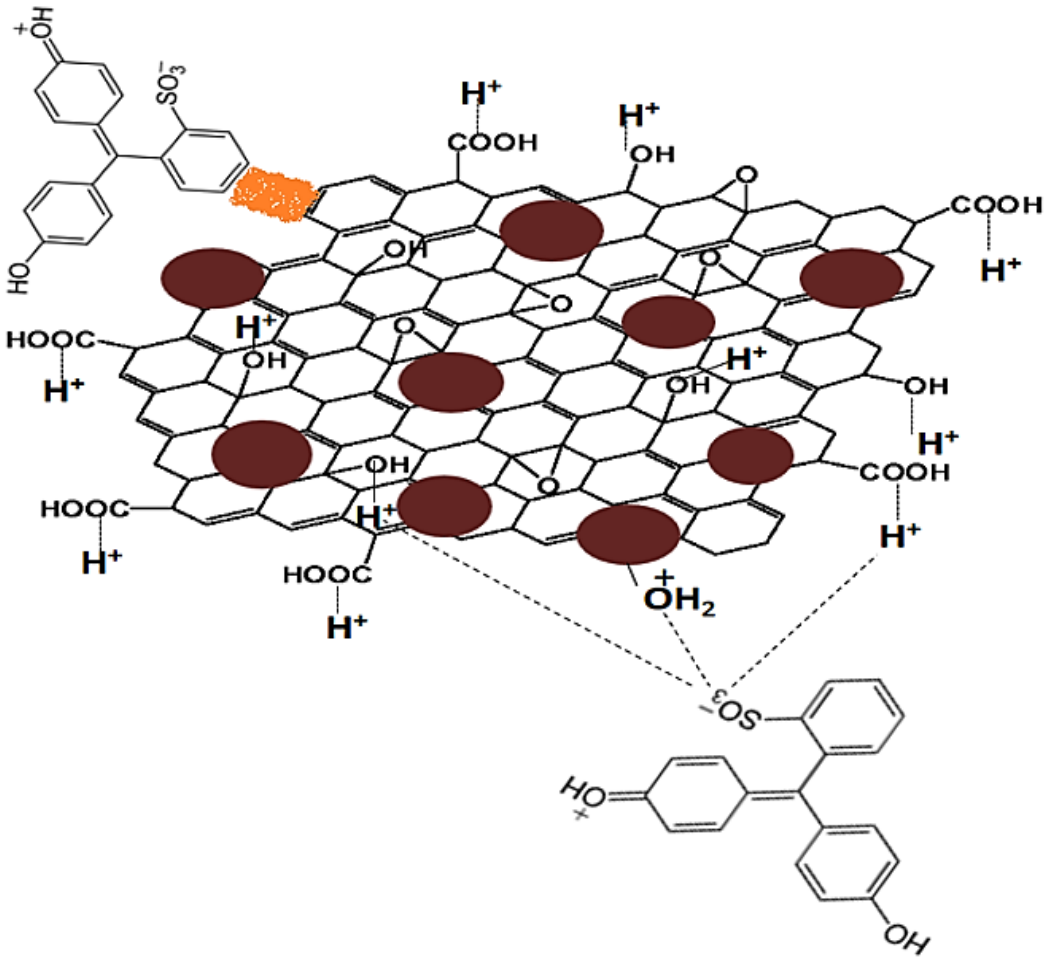

Figure.4.60. Possible interactions of phenol red dye with GO-Fe_3O_4 hybrid.

4.2.4.3. Adsorption Kinetics

The kinetic experiment was done to investigate the efficacy of GO-Fe_3O_4 hybrids (adsorbent) as a function of contact time for the removal of phenol red. The adsorption kinetics play an important role in dye removal as it gives a better understanding of mechanism of adsorption reactions. This experiment was performed at different adsorption times from 10-80 mins for 10 mg L^{-1} initial concentration and optimum dose. phenol red for GO-Fe_3O_4 hybrids system kinetically behave differently than malachite green for the same system. It is observed that almost 67% adsorption efficiency was achieved for 70 mins than there is no significant change is seen after this. As noted, the increase in adsorption is may be due to more number of available

diffusion sites and then further increase leads to increased diffusion path length [173]. The slope of the plot shows a slow rate of adsorption on adsorbent surface **(Figure.4.61)**. This could be due to attractive electrostatic attraction between the adsorbate and adsorbent to attain the equilibrium time.

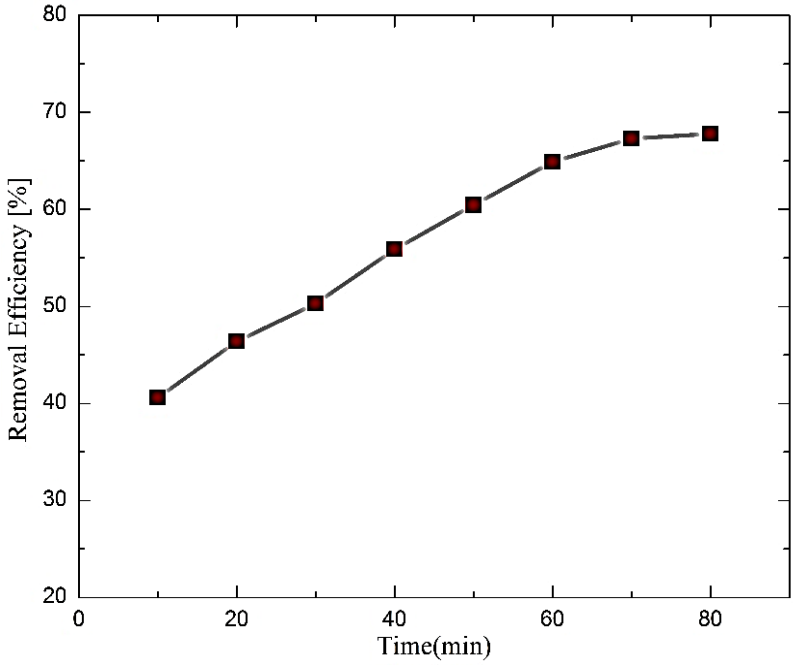

Figure.4.61. Time versus %removal of phenol red by GO-Fe_3O_4 hybrids for initial dye concentration of 10 mg L^{-1}, adsorbent dose 0.011 g and pH-4.

The kinetics of phenol red removal was determined to understand the adsorption behavior of hybrid material. Two different kinetic models such as pseudo-first-order (**Eq. 3.1**) and pseudo-second-order (**Eq. 3.2**) have been used to investigate the adsorption kinetics and furthermore, the kinetics of neutral dye were well described by three diffusion controlled model, Elovich (**Eq. 3.3)**, Weber-Morris (**Eq. 3.4)**, and Bangham (**Eq. 3.5)**. The results from above mentioned kinetic models and their calculated parameters are shown in **Table.4.7**.

Table.4.7. Kinetic parameters for phenol red removal onto GO-Fe_3O_4 hybrids.

Kinetic models	**Parameters**	**Values**
Pseudo-1st Order	R^2	0.82
	K_I (min^{-1})	0.06
	q_e (mg g^{-1})	82.92
Pseudo-2nd Order	R^2	0.99
	K_{II} (g mg^{-1} min^{-1})	0.0009
	q_e (mg g^{-1})	78.67
	V_0 (mg g^{-1} min^{-1})	5.77
Elovich	R^2	0.94
	β (mg g^{-1} min^{-1})	0.071
	α (g mg^{-1})	1.495
Weber-Morris	R^2	0.99
	K_{IP} (mg g^{-1} $min^{-1/2}$)	5.31
Bangham	R^2	0.95
	K_B (ml g L^{-1})	59.83
	α	0.04

Adsorption kinetics for the phenol red onto GO-Fe_3O_4 was investigated by pseudo-first-order and pseudo-second-order model. A bad fit (R^2=0.82) was obtained from the linear pseudo-first order model, indicating it is completely not applicable to this system. But the regression coefficient, obtained from a pseudo second order kinetic model, is close to 1 i.e. 0.99 (**Figure.4.62)** showing applicability of this model fitting the experimental data. It supports an assumption that may be chemisorption is one of the involved interaction mechanism. The equilibrium adsorption capacity (q_e) and initial adsorption rate (V_0) found out as 78.67 mg g^{-1} and 5.77 mg g^{-1} min^{-1} respectively. 46.29 mg g^{-1} second order capacity was reported by M. *Ghaedi et al.* [174].

The kinetic data subsequently were analyzed by Elovich model. The diffusion based Elovich model was found to be partly applicable for diffusion of neutral dye molecules. The data were analyzed, a linear fit of this model with R^2 value of 0.94 is presented in **Figure.4.63**.

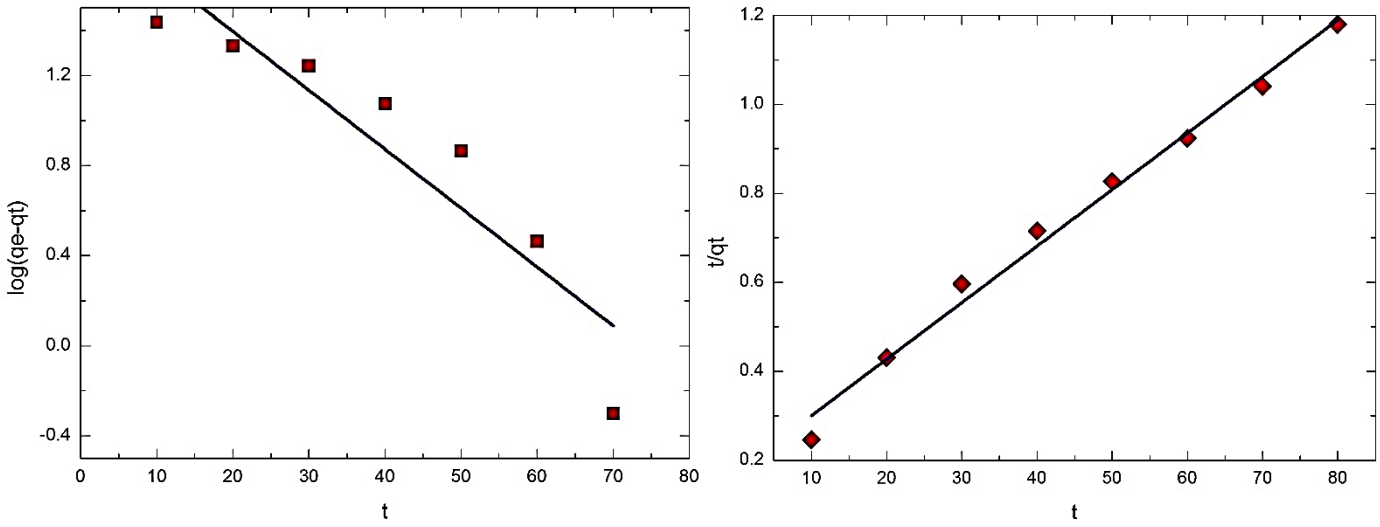

Figure.4.62. Pseudo-first-order model (left) and Pseudo-second-order model (right) for the removal of phenol red by GO-Fe_3O_4 hybrids.

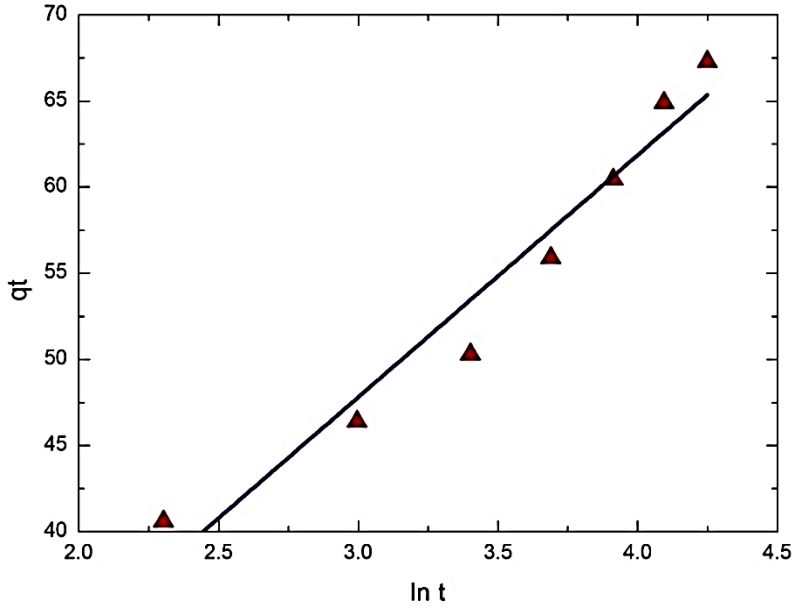

Figure.4.63. Elovich model for the removal of phenol red by GO-Fe_3O_4 hybrids.

To distinguish the rate limiting stage, W-M model was applied. It was reported that an intraparticle diffusion mechanism is active from calculated high value R^2 of 0.99 proved the linearity of adsorption completely followed Weber-Morris kinetics (**Figure.4.64)**. The behavior of W-M plot is linear for this system shows surface diffusion mechanism, the very

fast diffusion of dye molecules on the available active adsorbing site. But the line has an intercept, indicating the diffusion of the dye molecules through the boundary layer. It means boundary diffusion controlled adsorption mechanism is also considered to be the rate determining step. From the calculated high value of K_{IP} (5.31) suggest the intraparticle diffusion is not reasonable for internal diffusion.

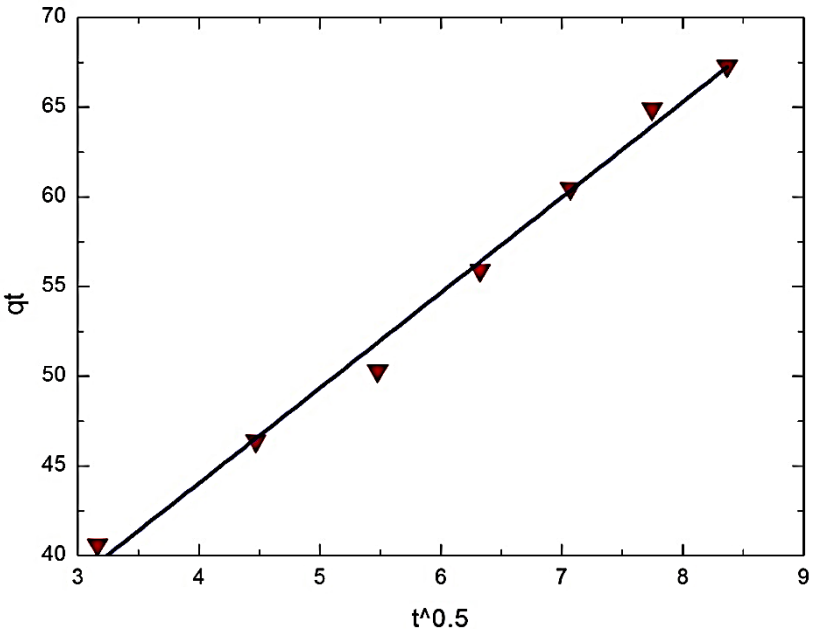

Figure.4.64. Weber-Morris model for the removal of phenol red by GO-Fe_3O_4 hybrids.

The final stage is generally considered as rate limiting step and require more time for migration and transfer of dye molecules to the inner pores of hybrid structure. After saturation time, the adsorption rate slows down which can be modelled by Bangham fit of the experimental data showed adsorption process has few contributions from pore diffusion. The linear plot with R^2 value of 0.95 presented in **Figure.4.65**. Actually, the slow adsorption of dye molecules after saturation is due to the migration of molecules inside the pores, but phenol red has a aromatic ring structure renders the pure pore diffusion process. The above phenomena justified the pore diffusion is not the rate limiting step.

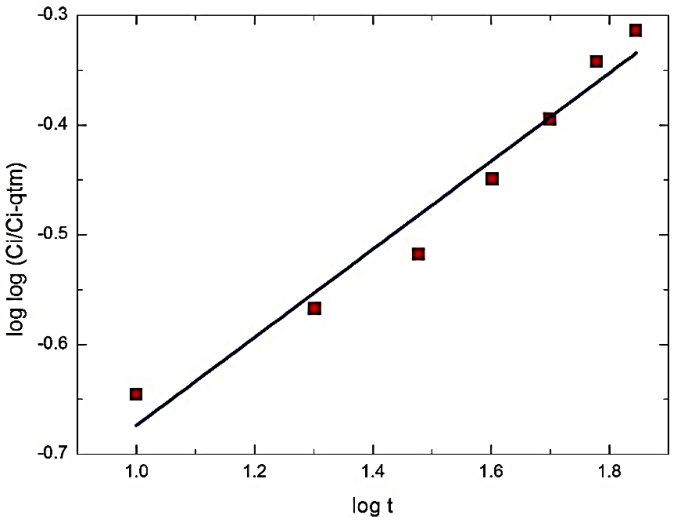

Figure.4.65. Bangham model for the removal of phenol red by GO-Fe_3O_4 hybrids.

4.2.4.4. Adsorption Isotherms

Concentration is a vital parameter needs to be studied because a very small concentration of dye in water is unpleasant. Variation of initial dye concentration from 10-80 mg L^{-1} and its effect on adsorption efficacy is shown in **Figure.4.66**. It is observed that increasing the dye concentration for a constant dose the adsorption efficiency is quite complex. The complexity of the graph is because of dual charge present in neutral dye [62].

However, from the calculated isotherm parameters (**Table.4.8**) it proved the adsorption of phenol red onto GO-Fe_3O_4 hybrids followed Langmuir model, has a highest R^2 value of 0.99. It supported the assumption of monolayer formation of neutral dye molecules. The maximum monolayer adsorption capacity (q_m) and Langmuir constant (K_L) could be calculated from the intercept and slope of the linear plot of $1/C_e$ versus $1/q_e$ plot (**Figure.4.67**). The free energy parameter related to Langmuir constant calculated to be -8.48 kJ mol^{-1} confirmed the process is spontaneous with +ve enthalpy. However, the energy is falling in the range of physisorption. It means the monolayer formation of dye molecules on GO-Fe_3O_4 hybrids surface but the type of interaction satisfied physisorption process. Additionally, the dimensionless parameter (R_L) calculated as 0.76 indicated the favorable process. The maximum adsorption was found out 657.89 mg g^{-1}. *Alok Mittal et al.* [175] has reported 2.6×10^{-5} mol g^{-1} of monolayer capacity by Bottom ash, a waste from thermal power plant for 10×10^{-5} M of phenol red. 276.24 mg g^{-1}

capacity was investigated using SBA-16 as an adsorbent by *Haribandhu Chaudhuri et al.* [176] for 100 mg L^{-1} dye solution. Activated charcoal was used by *Muhammad J. Iqbal et al.* [177] for removal of 3.5 mg L^{-1} with 0.04 mg g^{-1} capacity.

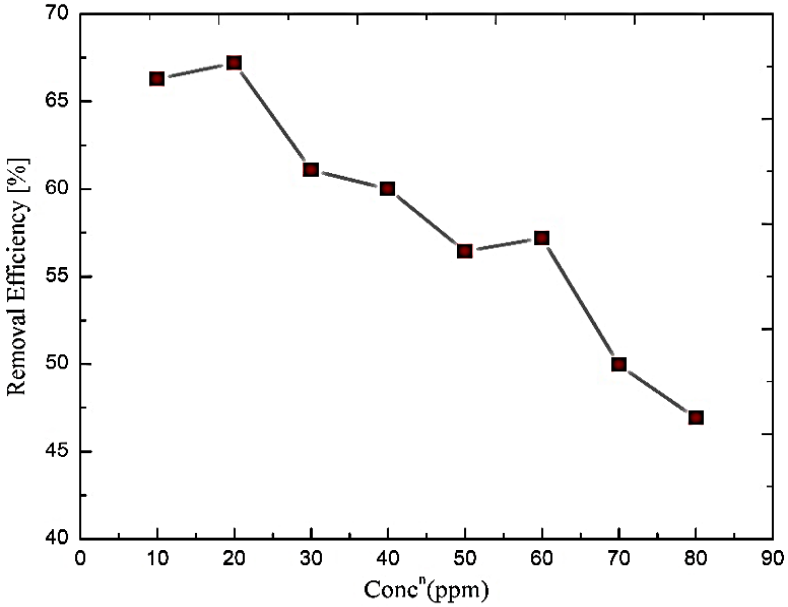

Figure.4.66. Effect of initial dye concentration versus %removal of phenol red by GO-Fe_3O_4 hybrids for adsorbent dose 0.011 g, pH-4, room temperature and time 70 mins.

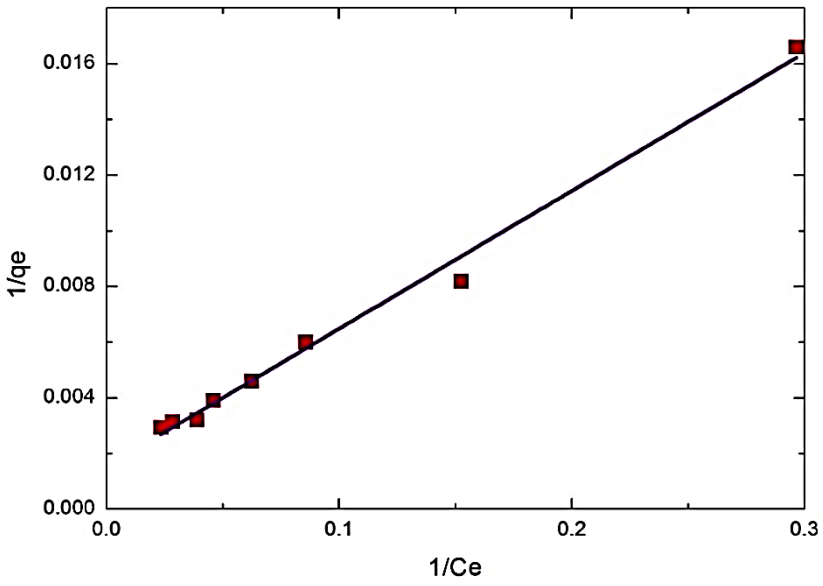

Figure.4.67. Langmuir model for the removal of phenol red by GO-Fe_3O_4 hybrids.

The Freundlich plot of data showed a poor fit with regression coefficient 0.96. It suggested the possibility of physisorption is not suitable for this system. The intensity of the adsorption is represented as a constant n, was calculated to be 1.47 from the slope of the linear plot (**Figure.4.68)**. The value n showed the high tendency of adsorption and, in addition, indicates the favorable process of adsorption.

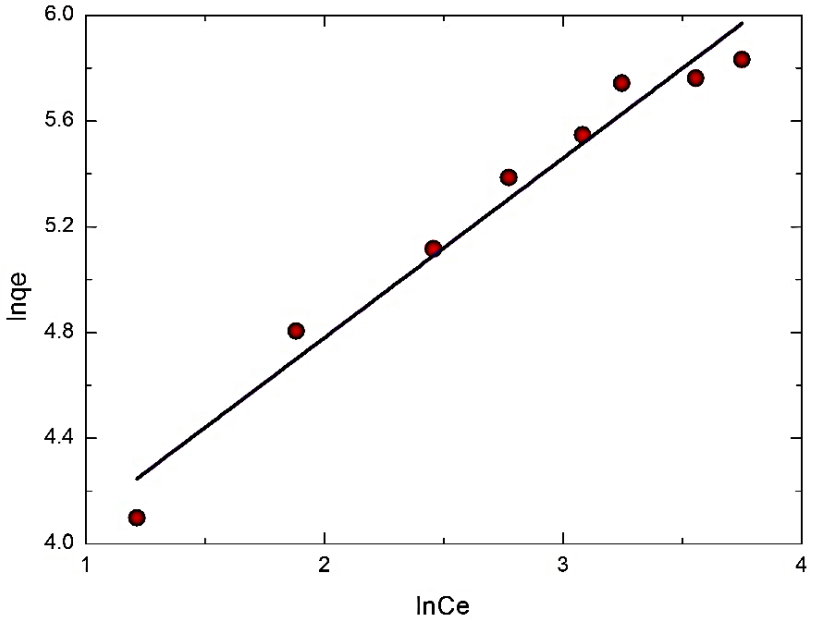

Figure.4.68. Freundlich model for the removal of phenol red by GO-Fe_3O_4 hybrids.

Then the Temkin isotherm model was derived using the data showed R^2 value of 0.97 from Temkin plot (**Figure.4.69**). The low heat of adsorption (b), 21.35 J mol^{-1} from this model suggested the mechanism of adsorption followed physisorption.

Table.4.8. Isotherm parameters for phenol red removal onto GO-Fe_3O_4 hybrids.

Isotherm models	Parameters	Values
Langmuir	R^2	0.99
	q_m (mg g^{-1})	657.89
	K_L (L mg^{-1})	0.03
	ΔG (kJ mol^{-1})	-8.48
	R_L	0.76
Friendlich	R^2	0.96
	K_F (mg g^{-1})	30.595
	n	1.47
DR	R^2	0.96
	K_{DR}	-0.006
	q_m (mg g^{-1})	366.58
	E (kJ mol^{-1})	8.59
Temkin	R^2	0.97
	b (J mol^{-1})	21.35
	K_T (L g^{-1})	0.444

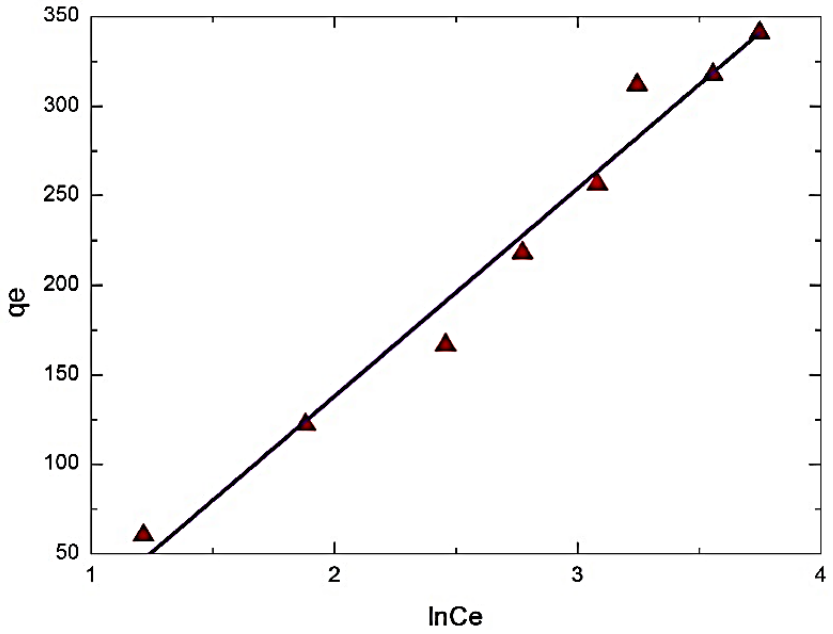

Figure.4.69. Temkin model for the removal of phenol red by GO-Fe_3O_4 hybrids.

A partially fitted D-R plot with R^2=0.96 for this system is shown in **Figure.4.70**. The mean sorption energy (E) derived 8.59 kJ mol^{-1} is related to physisorption. Some π-π interactions are also involved which has low energy. Therefore, the adsorption of phenol red onto GO-Fe_3O_4 hybrids is monolayer type, but the interaction involves electrostatic and π-π interactions. The complexcity in the adsorption mechanism is due to dual charge present in the dye molecules [62].

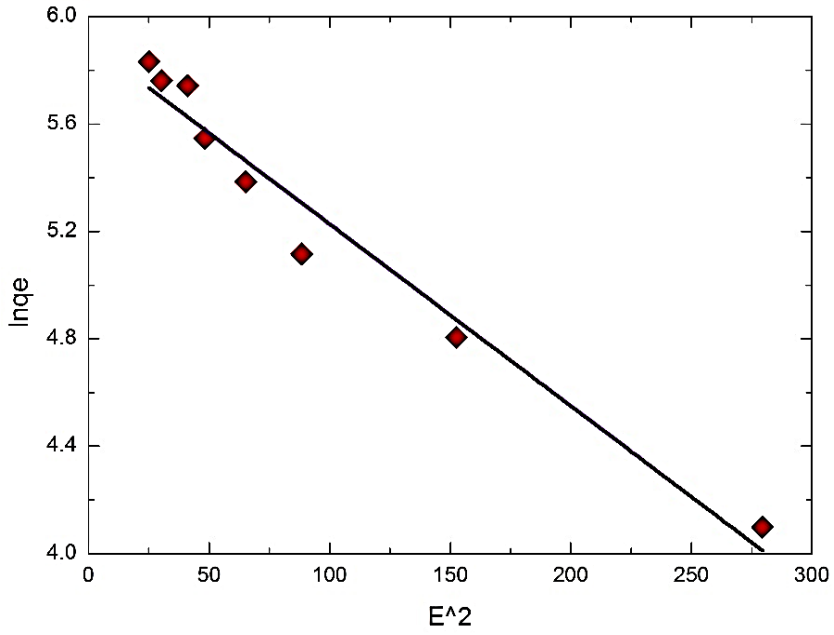

Figure.4.70. D-R model for the removal of phenol red by GO-Fe_3O_4 hybrids.

4.2.4.5. Mechanism of Desorption

Desorption of phenol red from GO-Fe_3O_4 hybrids bed was achieved by acid/base leaching process. Two cost effective eluents 0.1M HCl and 0.1M NaOH are used for eluting the adsorbent bed. Adsorption of phenol red is completely based on the electrostatic interactions between adsorbent surface and dye molecules. Physisorption shows superior desorption than chemisorption. The chemistry of chromium metal and adsorbent material in acidic solution reported in previous sections demonstrate the maximum adsorption is favorable in acidic medium. As desorption is the reverse mechanism of adsorption, it is favorable at basic medium

shown in **Figure.4.71**. The maximum 66.37% of desorption was calculated from **Eq. 4.2** at pH-10 for this system.

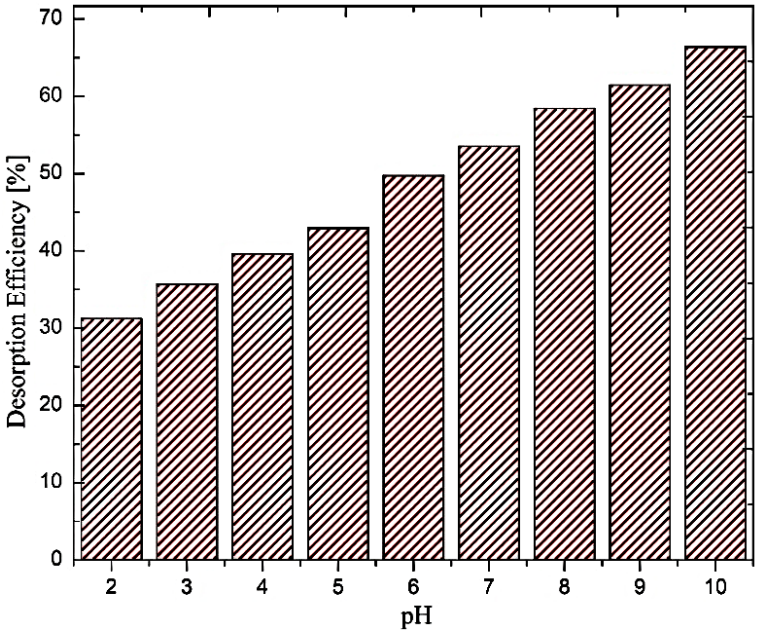

Figure.4.71. %desorption of phenol red from GO-Fe_3O_4 hybrids as a function of pH.

CHAPTER-5

CONCLUSION AND SUMMARY

In this section, all of the results in the current work are summarized and future prospects of the work are outlines.

The evaluation of adsorption of toxins by the novel graphene oxide-magnetite based hybrid nanoadsorbents, prepared by a facile straight forward process, was done, and interesting informations were obtained. The results can be summarized as follows.

- The sonication assisted synthesis of bare magnetite materials exhibited nanoparticulate morphology with narrow size distribution, and specific surface area of 128.6 m^2 g^{-1}, which is encouraging for such a simple process. The pore size distribution indicated porosity between 2-6 nm.
- The adsorption of Cr(VI) ions by the magnetite nanoparticles showed adsorption capacity of 1.67 mg g^{-1}, which is comparable or better than many of the adsorbents in the literature. The initial adsorption rate was much better at 0.03 mg g^{-1} min^{-1}, as calculated from pseudo-second order kinetics.
- The adsorption kinetics followed intraparticle diffusion model, followed by pore diffusion towards saturation of adsorption. These results are in congruence with the morphology of the nanoparticles examined by electron microscopy, and from gas adsorption techniques.
- The adsorption isotherm data of Cr(VI) could be modeled with Langmuir adsorption isotherms, indicating monolayer adsorption. The monolayer adsorption capacity of 5.9 mg g^{-1} was found. The process was found to be energetically favorable, and spontaneous in nature.
- The GO-Fe_3O_4 hybrid nanoadsorbents exhibited almost 95% of removal efficiency at an initial concentration of 10 mg L^{-1} of Cr(VI).
- The kinetics followed pseudo-second order rate model, with an excellent initial adsorption rate of 0.48 mg g^{-1} min^{-1}, which was an order of magnitude higher than that of the bare magnetite nanoparticles. The second order adsorption capacity was 4.6 mg g^{-1}.
- Other kinetic models showed variable degrees of agreement indicating that intraparticle diffusion controlled by the surface diffusion of Cr ions, as well as pore diffusion dominated the adsorption process at several stages. The process was clearly chemisorption.

- The adsorption isotherms exhibited fit to the Langmuir model with maximum adsorption capacity of 10.23 mg g^{-1}. The free energy change for the process was -18.11 kJ $mole^{-1}$ indicating that the process was spontaneous and favorable.
- The use of GO-Fe_3O_4 hybrids for the removal of malachite green exhibited excellent adsorption capacity of more than 97% removal efficiency in a very low initial concentration of 10 mg L^{-1}. The adsorption capacity calculated was 102.67 mg g^{-1} from the adsorption kinetics data.
- The initial adsorption capacity found was exceptionally high and indicated kinetically faster adsorption of the cationic dye.
- Based on the Langmuir adsorption isotherms that maximal adsorption capacity was calculated as 288.18 mg g^{-1}, which is considerably higher than data reported in the literature.
- The hybrids showed very good adsorption kinetics, with removal efficiency of 68% for phenol red. The kinetics followed second-order model while other models indicated that the process can be a mixture of diffusion and physisorption. The adsorption capacity of 78.67 mg g^{-1}, as calculated from pseudo-second order kinetics.
- Based on Langmuir isotherm the maximum adsorption capacity was found to be 657.89 mg g^{-1}, and the process was spontaneous under the experimental conditions. The slightly inferior adsorption of phenol red as compared to malachite green was due to neutral nature of the dye, leading to physisorption as the only mechanisms.

Thus, the current work has clearly demonstrated that graphene oxide-magnetite hybrids synthesized in this study can act as potential adsorbents for a variety of toxins, starting from heavy metals to different dye molecules. The fact that no particular functionalization of the adsorbents was followed in this work underscores the high efficiency of this material. The hybrid can be appropriately functionalized depending on the targeted toxic ion to enhance further the adsorption capacity and kinetics.

REFERENCES:

1. Myers, R.A. and B. Worm, *Rapid worldwide depletion of predatory fish communities.* Nature, 2003. **423**(6937): p. 280-283.
2. Freedman, B., *Environmental ecology: the ecological effects of pollution, disturbance, and other stresses*. 1995: Academic Press.
3. Claxton, L.D., V.S. Houk, and T.J. Hughes, *Genotoxicity of industrial wastes and effluents.* Mutation Research/Reviews in Mutation Research, 1998. **410**(3): p. 237-243.
4. Hua, M., et al., *Heavy metal removal from water/wastewater by nanosized metal oxides: a review.* Journal of Hazardous Materials, 2012. **211**: p. 317-331.
5. Kampa, M. and E. Castanas, *Human health effects of air pollution.* Environmental pollution, 2008. **151**(2): p. 362-367.
6. Costa, M., *Toxicity and carcinogenicity of Cr(VI) in animal models and humans.* Critical reviews in toxicology, 1997. **27**(5): p. 431-442.
7. Axtell, N.R., S.P.K. Sternberg, and K. Claussen, *Lead and nickel removal using Microspora and Lemna minor*. Bioresource Technology, 2003. **89**(1): p. 41-48.
8. Amarasinghe, B.M.W.P.K. and R.A. Williams, *Tea waste as a low cost adsorbent for the removal of Cu and Pb from wastewater.* Chemical Engineering Journal, 2007. **132**(1-3): p. 299-309.
9. Yurtsever, M. and I.A. Sengil, *Biosorption of Pb(II) ions by modified quebracho tannin resin.* Journal of Hazardous Materials, 2009. **163**(1): p. 58-64.
10. Kazi, T.G., et al., *Evaluation of toxic metals in blood and urine samples of chronic renal failure patients, before and after dialysis.* Renal Failure, 2008. **30**(7): p. 737-745.
11. Afridi, H.I., et al., *Essential trace and toxic element distribution in the scalp hair of Pakistani myocardial infarction patients and controls.* Biological Trace Element Research, 2006. **113**(1): p. 19-34.
12. Skerfving, S., et al., *Lead - Biological monitoring of exposure and effects.* Journal of Trace Elements in Experimental Medicine, 1998. **11**(2-3): p. 289-301.
13. Soylak, M., et al., *On-line preconcentration system for determination of lead in water and sediment samples by flow injection-flame atomic absorption spectrometry.* Analytical Letters, 2002. **35**(3): p. 487-499.
14. Raungsomboon, S., et al., *Removal of lead (Pb2+) by the Cyanobacterium Gloeocapsa sp.* Bioresource Technology, 2008. **99**(13): p. 5650-5658.
15. Unlu, N. and M. Ersoz, *Adsorption characteristics of heavy metal ions onto a low cost biopolymeric sorbent from aqueous solutions.* Journal of Hazardous Materials, 2006. **136**(2): p. 272-280.
16. Eren, E., B. Afsin, and Y. Onal, *Removal of lead ions by acid activated and manganese oxide-coated bentonite.* Journal of Hazardous Materials, 2009. **161**(2-3): p. 677-685.
17. Aksu, Z., F. Gonen, and Z. Demircan, *Biosorption of chromium(VI) ions by Mowital (R) B30H resin immobilized activated sludge in a packed bed: comparison with granular activated carbon.* Process Biochemistry, 2002. **38**(2): p. 175-186.

18. Charerntanyarak, L., *Heavy metals removal by chemical coagulation and precipitation.* Water Science and Technology, 1999. **39**(10): p. 135-138.
19. Corbitt, R.A., *Standard Hand Book of Environmental Engineering*. second ed. 1999: McGraw Hill.
20. Yu, Q.M. and P. Kaewsarn, *Adsorption of Ni2+ from aqueous solutions by pretreated biomass of marine macroalga Durvillaea potatorum.* Separation Science and Technology, 2000. **35**(5): p. 689-701.
21. Bailey, S.E., et al., *A review of potentially low-cost sorbents for heavy metals.* Water research, 1999. **33**(11): p. 2469-2479.
22. Babel, S. and T.A. Kurniawan, *Low-cost adsorbents for heavy metals uptake from contaminated water: a review.* Journal of hazardous materials, 2003. **97**(1): p. 219-243.
23. King, P., et al., *Removal of lead from aqueous solution using Syzygium cumini L.: Equilibrium and kinetic studies.* Journal of Hazardous Materials, 2007. **142**(1-2): p. 340-347.
24. Ahalya, N., T.V. Ramachandra, and R.D. Kanamadi, *Biosorption of heavy metals.* Res. J. Chem. Environ. , 2003. **7**: p. 71-78.
25. Volesky, B., *Detoxification of metal-bearing effluents: biosorption for the next century.* Hydrometallurgy, 2001. **59**(2-3): p. 203-216.
26. Crist, R.H., et al., *Uptake of metals on feat moss: An ion-exchange process.* Environmental Science & Technology, 1996. **30**(8): p. 2456-2461.
27. Ajmal, M., et al., *Adsorption studies on rice husk: removal and recovery of Cd(II) from wastewater.* Bioresource Technology, 2003. **86**(2): p. 147-149.
28. Panday, K.K., G. Prasad, and V.N. Singh, *Cu(II) removal from aqueous solutions by fly ash.* Water Res., 1985. **19**: p. 869–873.
29. Al-Asheh, S. and Z. Duvnjak, *Binary metal sorption by pine bark: Study of equilibria and mechanisms.* Separation Science and Technology, 1998. **33**(9): p. 1303-1329.
30. Bulut, Y. and Z. Tez, *Removal of heavy metals from aqueous solution by sawdust adsorption.* Journal of Environmental Sciences-China, 2007. **19**(2): p. 160-166.
31. Al-Asheh, S., F. Banat, and F. Mohai, *Sorption of copper and nickel by spent animal bones.* Chemosphere, 1999. **39**(12): p. 2087-2096.
32. Rao, M.M., et al., *Removal of copper and cadmium from the aqueous solutions by activated carbon derived from Ceiba pentandra hulls.* Journal of Hazardous Materials, 2006. **129**(1-3): p. 123-129.
33. Chowdhury, S. and R. Balasubramanian, *Recent advances in the use of graphene-family nanoadsorbents for removal of toxic pollutants from wastewater.* Advances in colloid and interface science, 2014. **204**: p. 35-56.
34. Panasiuk, O., *Phosphorus removal and recovery from wastewater using magnetite.* 2010.
35. Fu, F.L. and Q. Wang, *Removal of heavy metal ions from wastewaters: A review.* Journal of Environmental Management, 2011. **92**(3): p. 407-418.
36. Febrianto, J., et al., *Equilibrium and kinetic studies in adsorption of heavy metals using biosorbent: A summary of recent studies.* Journal of Hazardous Materials, 2009. **162**(2-3): p. 616-645.

37. Netzer, A. and D.E. Hughes, *Adsorption of copper, lead and cobalt by activated carbon.* Water research, 1984. **18**(8): p. 927-933.
38. Corapcioglu, M.O. and C.P. Huang, *The adsorption of heavy metals onto hydrous activated carbon.* Water research, 1987. **21**(9): p. 1031-1044.
39. Kadirvelu, K., K. Thamaraiselvi, and C. Namasivayam, *Removal of heavy metals from industrial wastewaters by adsorption onto activated carbon prepared from an agricultural solid waste.* Bioresource Technology, 2001. **76**(1): p. 63-65.
40. Namasivayam, C. and D. Kavitha, *Removal of Congo Red from water by adsorption onto activated carbon prepared from coir pith, an agricultural solid waste.* Dyes and Pigments, 2002. **54**(1): p. 47-58.
41. Baral, S.S., S.N. Das, and P. Rath, *Hexavalent chromium removal from aqueous solution by adsorption on treated sawdust.* Biochemical Engineering Journal, 2006. **31**(3): p. 216-222.
42. Selvaraj, K., S. Manonmani, and S. Pattabhi, *Removal of hexavalent chromium using distillery sludge.* Bioresource Technology, 2003. **89**(2): p. 207-211.
43. Garg, U.K., et al., *Removal of hexavalent chromium from aqueous solution by agricultural waste biomass.* Journal of Hazardous Materials, 2007. **140**(1-2): p. 60-68.
44. Rao, G.P., C. Lu, and F. Su, *Sorption of divalent metal ions from aqueous solution by carbon nanotubes: A review.* Separation and Purification Technology, 2007. **58**(1): p. 224-231.
45. Gupta, V.K., et al., *Adsorptive removal of dyes from aqueous solution onto carbon nanotubes: A review.* Advances in Colloid and Interface Science, 2013. **193**: p. 24-34.
46. Stafiej, A. and K. Pyrzynska, *Adsorption of heavy metal ions with carbon nanotubes.* Separation and Purification Technology, 2007. **58**(1): p. 49-52.
47. Tofighy, M.A. and T. Mohammadi, *Adsorption of divalent heavy metal ions from water using carbon nanotube sheets.* Journal of Hazardous Materials, 2011. **185**(1): p. 140-147.
48. Mishra, A.K., T. Arockiadoss, and S. Ramaprabhu, *Study of removal of azo dye by functionalized multi walled carbon nanotubes.* Chemical Engineering Journal, 2010. **162**(3): p. 1026-1034.
49. Wu, C.H., *Adsorption of reactive dye onto carbon nanotubes: Equilibrium, kinetics and thermodynamics.* Journal of Hazardous Materials, 2007. **144**(1-2): p. 93-100.
50. Kuo, C.Y., C.H. Wu, and J.Y. Wu, *Adsorption of direct dyes from aqueous solutions by carbon nanotubes: Determination of equilibrium, kinetics and thermodynamics parameters.* Journal of Colloid and Interface Science, 2008. **327**(2): p. 308-315.
51. Clark, K.A., et al., *Evaluation of the Interactions between Multiwalled Carbon Nanotubes and Caco-2 Cells.* Journal of Toxicology and Environmental Health-Part a-Current Issues, 2012. **75**(1): p. 25-35.
52. Kim, J.S., et al., *Evaluation of biocompatible dispersants for carbon nanotube toxicity tests.* Archives of Toxicology, 2011. **85**(12): p. 1499-1508.
53. Liu, T.H., et al., *Adsorption of methylene blue from aqueous solution by graphene.* Colloids and Surfaces B-Biointerfaces, 2012. **90**: p. 197-203.
54. Li, Y.H., et al., *Adsorption of fluoride from aqueous solution by graphene.* Journal of Colloid and Interface Science, 2011. **363**(1): p. 348-354.

55. Zhao, J.P., W.C. Ren, and H.M. Cheng, *Graphene sponge for efficient and repeatable adsorption and desorption of water contaminations.* Journal of Materials Chemistry, 2012. **22**(38): p. 20197-20202.
56. Xu, J., L. Wang, and Y.F. Zhu, *Decontamination of Bisphenol A from Aqueous Solution by Graphene Adsorption.* Langmuir, 2012. **28**(22): p. 8418-8425.
57. Cheng, J.S., J. Du, and W.J. Zhu, *Facile synthesis of three-dimensional chitosan-graphene mesostructures for reactive black 5 removal.* Carbohydrate Polymers, 2012. **88**(1): p. 61-67.
58. Dreyer, D.R., et al., *The chemistry of graphene oxide.* Chemical Society Reviews, 2010. **39**(1): p. 228-240.
59. Lei, Y.L., et al., *Synthesis of three-dimensional graphene oxide foam for the removal of heavy metal ions.* Chemical Physics Letters, 2014. **593**: p. 122-127.
60. Zhao, G.X., et al., *Few-Layered Graphene Oxide Nanosheets As Superior Sorbents for Heavy Metal Ion Pollution Management.* Environmental Science & Technology, 2011. **45**(24): p. 10454-10462.
61. Yang, S., et al., *Adsorption kinetics, isotherms and thermodynamics of Cr(III) on graphene oxide.* Colloids and Surfaces a-Physicochemical and Engineering Aspects, 2014. **457**: p. 100-106.
62. Ramesha, G.K., et al., *Graphene and graphene oxide as effective adsorbents toward anionic and cationic dyes.* Journal of Colloid and Interface Science, 2011. **361**(1): p. 270-277.
63. Sun, L., H.W. Yu, and B. Fugetsu, *Graphene oxide adsorption enhanced by in situ reduction with sodium hydrosulfite to remove acridine orange from aqueous solution.* Journal of Hazardous Materials, 2012. **203**: p. 101-110.
64. Pavagadhi, S., et al., *Removal of microcystin-LR and microcystin-RR by graphene oxide: Adsorption and kinetic experiments.* Water Research, 2013. **47**(13): p. 4621-4629.
65. Zhu, Y.W., et al., *Graphene and Graphene Oxide: Synthesis, Properties, and Applications (vol 22, pg 3906, 2010).* Advanced Materials, 2010. **22**(46): p. 5226-5226.
66. Huang, X., et al., *Graphene-Based Materials: Synthesis, Characterization, Properties, and Applications.* Small, 2011. **7**(14): p. 1876-1902.
67. Wang, S.B., et al., *Adsorptive remediation of environmental pollutants using novel graphene-based nanomaterials.* Chemical Engineering Journal, 2013. **226**: p. 336-347.
68. Lu, K., G.X. Zhao, and X.K. Wang, *A brief review of graphene-based material synthesis and its application in environmental pollution management.* Chinese Science Bulletin, 2012. **57**(11): p. 1223-1234.
69. Perreault, F., A.F. de Faria, and M. Elimelech, *Environmental applications of graphene-based nanomaterials.* Chemical Society Reviews, 2015. **44**(16): p. 5861-5896.
70. Zhang, N.N., et al., *Fabrication of highly porous biodegradable monoliths strengthened by graphene oxide and their adsorption of metal ions.* Carbon, 2011. **49**(3): p. 827-837.

71. Upadhyay, R.K., N. Soin, and S.S. Roy, *Role of graphene/metal oxide composites as photocatalysts, adsorbents and disinfectants in water treatment: a review.* Rsc Advances, 2014. **4**(8): p. 3823-3851.
72. Hua, M., et al., *Heavy metal removal from water/wastewater by nanosized metal oxides: A review.* Journal of Hazardous Materials, 2012. **211**: p. 317-331.
73. Li, L.L., et al., *Adsorbent for chromium removal based on graphene oxide functionalized with magnetic cyclodextrin-chitosan.* Colloids and Surfaces B-Biointerfaces, 2013. **107**: p. 76-83.
74. Wilke, M., W.A. Caliebe, and P. Machek, *Magnetite at low temperature: Resonant Inelastic X-ray Scattering (RIXS) at the Fe K-edge.* Journal of Physics: Conference Series, 2009. **190**: p. 012090.
75. Harrison, R.J., R.E. Dunin-Borkowski, and A. Putnis, *Direct imaging of nanoscale magnetic interactions in minerals.* Proceedings of the National Academy of Sciences, 2002. **99.26**: p. 16556-16561.
76. Kumar, R., B.S. Inbaraj, and B.H. Chen, *Surface modification of superparamagnetic iron nanoparticles with calcium salt of poly (γ-glutamic acid) as coating material.* Materials Research Bulletin, 2010. **45.11**: p. 1603-1607.
77. Jang, J.H. and H.B. Lim, *Characterization and analytical application of surface modified magnetic nanoparticles.* Microchemical Journal, 2010. **94.2**: p. 148-158.
78. Petcharoen, K. and A. Sirivat, *Synthesis and characterization of magnetite nanoparticles via the chemical co-precipitation method.* Materials Science and Engineering :B, 2012. **177.5**(421-427).
79. Shen, Y.F., et al., *Preparation and application of magnetic Fe 3 O 4 nanoparticles for wastewater purification.* Separation and Purification Technology, 2009. **68.3**: p. 312-319.
80. Selvi, K., S. Pattabhi, and K. Kadirvelu, *Removal of Cr (VI) from aqueous solution by adsorption onto activated carbon.* Bioresource Technology, 2001. **80.1**: p. 87-89.
81. Karami, H., *Heavy metal removal from water by magnetite nanorods.* Chemical Engineering Journal, 2013. **219**: p. 209-216.
82. Saha, B., et al., *Preferential and enhanced adsorption of different dyes on iron oxide nanoparticles: a comparative study.* The Journal of Physical Chemistry C, 2011. **115.16**: p. 8024-8033.
83. Yuan, P., et al., *Removal of hexavalent chromium [Cr(VI)] from aqueous solutions by the diatomite-supported/unsupported magnetite nanoparticles,.* Journal of hazardous materials, 2010. **173.1** p. 614-621.
84. Sivudu, K.S. and K.Y. Rhee, *Preparation and characterization of pH-responsive hydrogel magnetite nanocomposite.* Colloids and Surfaces A: Physicochemical and Engineering Aspects, 2009. **349.1**: p. 29-34.
85. Basavaiah, K., Y.P. Kumar, and A.V.P. Rao, *A facile one-pot synthesis of polyaniline/magnetite nanocomposites by micelles-assisted method.* Applied Nanoscience, 2013. **3.4**: p. 409-415.
86. Yang, X., et al., *Graphene oxide-iron oxide and reduced graphene oxide-iron oxide hybrid materials for the removal of organic and inorganic pollutants.* RSC Advances, 2012. **2.23**: p. 8821-8826.

87. Deng, J.H., et al., *Simultaneous removal of Cd (II) and ionic dyes from aqueous solution using magnetic graphene oxide nanocomposite as an adsorbent.* Chemical Engineering Journal, 2013. **226**: p. 189-200.
88. Liu, M., et al., *Synthesis of magnetite/graphene oxide composite and application for cobalt (II) removal.* The Journal of Physical Chemistry C, 2011. **115.51**: p. 25234-25240.
89. Barakat, M.A., *New trends in removing heavy metals from industrial wastewater.* Arabian Journal of Chemistry, 2011. **4.4**: p. 361-377.
90. Xia, L., et al., *Storage and Release of Soluble Hexavalent Chromium from Chromate Conversion Coatings Equilibrium Aspects of Cr VI Concentration.* Journal of The Electrochemical Society, 2000. **147.7** p. 2556-2562.
91. Fu, F. and Q. Wang, *Removal of heavy metal ions from wastewaters: a review.* Journal of Environmental Management, 2011. **v**: p. 407-418.
92. Pradhan, J., S.N. Das, and R.S. Thakur, *Adsorption of hexavalent chromium from aqueous solution by using activated red mud.* Journal of Colloid and Interface Science, 1999. **217.1**: p. 137-141.
93. Deng, S. and R. Bai, *Removal of trivalent and hexavalent chromium with aminated polyacrylonitrile fibers: performance and mechanisms.* Water research, 2004. **38.9**.
94. Owlad, M., et al., *Removal of hexavalent chromium-contaminated water and wastewater: a review.* Water, Air, and Soil Pollution, 2009. **200. 1-4** p. 59-77.
95. Granados-Correa, F. and J. Jiménez-Becerril, *Chromium (VI) adsorption on boehmite.* Journal of hazardous materials, 2009. **162.2**: p. 1178-1184.
96. Li, Y., et al., *Hexavalent chromium removal from aqueous solution by adsorption on aluminum magnesium mixed hydroxide.* Water research, 2009. **43.12**: p. 3067-3075.
97. Gupta, V.K., A. Rastogi, and A. Nayak, *Adsorption studies on the removal of hexavalent chromium from aqueous solution using a low cost fertilizer industry waste material.* Journal of Colloid and Interface Science, 2010. **342.1**: p. 135-141.
98. Hena, S., *Removal of chromium hexavalent ion from aqueous solutions using biopolymer chitosan coated with poly 3-methyl thiophene polymer.* Journal of hazardous Materials, 2010. **181.1**: p. 474-479.
99. Hamadi, N.K., et al., *Adsorption kinetics for the removal of chromium (VI) from aqueous solution by adsorbents derived from used tyres and sawdust.* Chemical Engineering Journal, 2001. **84.2**: p. 95-105.
100. Pérez-Candela, M., J. Martín-Martínez, and R. Torregrosa-Macia, *Chromium (VI) removal with activated carbons.* Water Research, 1995. **29.9**: p. 2174-2180.
101. Karthikeyan, T., S. Rajgopal, and L.R. Miranda, *Chromium (VI) adsorption from aqueous solution by Hevea Brasilinesis sawdust activated carbon.* Journal of hazardous materials, 2005. **124.1**: p. 192-199.
102. Sharma, D.C. and C.F. Forster, *A preliminary examination into the adsorption of hexavalent chromium using low-cost adsorbents.* Bioresource Technology, 1994. **47.3**: p. 257-264.
103. Alaerts, G.J., V. Jitjaturunt, and P. Kelderman, *Use of coconut shell-based activated carbon for chromium (VI) removal.* Water science and technology, 1989. **21.12**: p. 1701-704.

104. Cimino, G., A. Passerini, and G. Toscano, *Removal of toxic cations and Cr (VI) from aqueous solution by hazelnut shell.* Water Research, 2000. **34.11**: p. 2955-2962.
105. Acar, F.N. and E. Malkoc, *The removal of chromium (VI) from aqueous solutions by Fagus orientalis L.* Bioresource Technology, 2004. **94.1**: p. 13-15.
106. Babel, S. and T.A. Kurniawan, *Cr (VI) removal from synthetic wastewater using coconut shell charcoal and commercial activated carbon modified with oxidizing agents and/or chitosan.* Chemosphere, 2004. **54.7**: p. 951-967.
107. Garg, V.K., et al., *Adsorption of chromium from aqueous solution on treated sawdust.* Bioresource Technology, 2004. **92.1**: p. 79-81.
108. Aydın, Y.A. and N.D. Aksoy, *Adsorption of chromium on chitosan: Optimization, kinetics and thermodynamics.* Chemical Engineering Journal, 2009. **151.1**: p. 188-194.
109. Schmuhl, R.H., M. Krieg, and K. Keizer, *Adsorption of Cu (II) and Cr (VI) ions by chitosan: Kinetics and equilibrium studies.* Water Sa, 2004. **27.1**: p. 1-8.
110. Kumar, A.S.K., et al., *Effective adsorption of hexavalent chromium through a three center (3c) co-operative interaction with an ionic liquid and biopolymer.* Journal of hazardous materials, 2012. **239**: p. 213-224.
111. Wu, Y., et al., *Adsorption of hexavalent chromium from aqueous solutions by graphene modified with cetyltrimethylammonium bromide.* Journal of colloid and interface science, 2013. **394**: p. 183-191.
112. Kumar, A.S.K. and N. Rajesh, *Exploring the interesting interaction between graphene oxide, Aliquat-336 (a room temperature ionic liquid) and chromium (VI) for wastewater treatment.* RSC Advances, 2013. **3.8**.
113. Mahmoud, D.K., et al., *Batch adsorption of basic dye using acid treated kenaf fibre char: equilibrium, kinetic and thermodynamic studies.* Chemical Engineering Journal, 2012. **181**: p. 449-457.
114. Lokman, F., *Dye removal from simulated wastewater by using empty fruit bunch as an adsorption agent*, in *Diss. Universiti Malaysia Pahang*. 2006.
115. Dash, B., *Competitive Adsorption of dyes (congo red, methylene blue, malachite green) on Activated Carbon.* Diss. NATIONAL INSTITUTE OF TECHNOLOGY, ROURKELA, 2010.
116. Gupta, V.K., et al., *Adsorption kinetics and column operations for the removal and recovery of malachite green from wastewater using bottom ash.* Separation and Purification Technology, 2004. **v**: p. 87-96.
117. Culp, S.J., et al., *Toxicity and metabolism of malachite green and leucomalachite green during short-term feeding to Fischer 344 rats and B6C3F 1 mice.* Chemico-biological interactions, , 1999. **122.3**: p. 153-170.
118. Srivastava, S., R. Sinha, and D. Roy, *Toxicological effects of malachite green.* Aquatic toxicology, 2004. **66.3**: p. 319-329.
119. Chowdhury, S., et al., *Adsorption thermodynamics, kinetics and isosteric heat of adsorption of malachite green onto chemically modified rice husk.* Desalination, 2011. **265.1** p. 159-168.
120. Khattri, S.D. and M.K. Singh, *Removal of malachite green from dye wastewater using neem sawdust by adsorption.* Journal of Hazardous Materials, 2009. **167.1**: p. 1089-1094.

121. Kumar, K.V., S. Sivanesan, and V. Ramamurthi, *Adsorption of malachite green onto Pithophora sp., a fresh water algae: equilibrium and kinetic modelling.* Process Biochemistry, 2005. **40.8**: p. 2865-2872.
122. Gupta, V.K., et al., *Adsorption kinetics and column operations for the removal and recovery of malachite green from wastewater using bottom ash.* Separation and Purification Technology, 2004. **40.1**: p. 87-96.
123. Ahmad, R. and R. Kumar, *Adsorption studies of hazardous malachite green onto treated ginger waste.* Journal of Environmental Management, 2010. **91.4**: p. 1032-1038.
124. Onal, Y., C. Akmil-Başar, and C. Sarıcı-Ozdemir, *Investigation kinetics mechanisms of adsorption malachite green onto activated carbon.* Journal of hazardous materials, 2007. **146.1**: p. 194-203.
125. Tian, Y., et al., *Adsorption of malachite green from aqueous solutions onto ordered mesoporous carbons.* Chemical Engineering Journal, 2011. **171.3**: p. 1263-1269.
126. Santhi, T., S. Manonmani, and T. Smitha, *Removal of malachite green from aqueous solution by activated carbon prepared from the epicarp of Ricinus communis by adsorption.* Journal of hazardous materials, 2010. **179.1**: p. 178-186.
127. Guo, Y., et al., *Adsorption of malachite green and iodine on rice husk-based porous carbon.* Materials chemistry and physics, 2003. **82.1**: p. 107-115.
128. Guo, Y., et al., *Adsorption of malachite green on micro-and mesoporous rice husk-based active carbon.* Dyes and Pigments, 2003. **56.3**: p. 219-229.
129. Nethaji, S., et al., *Adsorption of Malachite Green dye onto activated carbon derived from Borassus aethiopum flower biomass.* Journal of Hazardous Materials, 2010. **181.1**: p. 271-280.
130. Samiey, B. and A.R. Toosi, *Adsorption of malachite green on silica gel: Effects of NaCl, pH and 2-propanol.* Journal of hazardous materials, 2010. **184.1**: p. 739-745.
131. Hameed, B.H. and M.I. El-Khaiary, *Kinetics and equilibrium studies of malachite green adsorption on rice straw-derived char.* Journal of Hazardous Materials, 2008. **153.1**: p. 701-708.
132. Bulut, E., M. Ozacar, and I.A. Şengil, *Adsorption of malachite green onto bentonite: equilibrium and kinetic studies and process design.* Microporous and mesoporous materials, 2008. **115.3**: p. 234-246.
133. Ai, L., et al., *Activated carbon/CoFe2O4 composites: Facile synthesis, magnetic performance and their potential application for the removal of malachite green from water,.* Chemical Engineering Journal, 2010. **156.2**: p. 243-249.
134. Bekçi, Z., et al., *Sorption of malachite green on chitosan bead.* Journal of hazardous materials, 2008. **154.1**: p. 254-261.
135. Bradder, P., et al., *Dye adsorption on layered graphite oxide.* Journal of Chemical & Engineering Data, 2010. **56.1** p. 138-141.
136. Geng, Z., et al., *Highly efficient dye adsorption and removal: a functional hybrid of reduced graphene oxide-Fe3O4 nanoparticles as an easily regenerative adsorbent.* Journal of Materials Chemistry A, 2012. **22.8**: p. 3527-3535.
137. Pagga, U. and K. Taeger, *Development of a method for adsorption of dyestuffs on activated sludge.* Water Research, 1994. **28.5** p. 1051-1057.

138. Zhu, Y., et al., *Cytotoxicity of phenol red in toxicity assays for carbon nanoparticles.* International journal of molecular sciences, 2012. **13.10** p. 12336-12348.
139. Iqbal, M.J. and M.N. Ashiq, *Adsorption of dyes from aqueous solutions on activated charcoal,* . Journal of Hazardous Materials, 2007. **139.1**: p. 57-66.
140. Wu, Z., et al., *Organic dye adsorption on mesoporous hybrid gels,* . Chemical Engineering Journal, 2004. **102.3**: p. 277-282.
141. Wu, Z., et al., *Enhancing the organic dye adsorption on porous xerogels.* Colloids and Surfaces A: Physicochemical and Engineering Aspects, 2004. **240.1**: p. 157-164.
142. Liu, M.C., et al., *Synthesis of Magnetite/Graphene Oxide Composite and Application for Cobalt(II) Removal.* Journal of Physical Chemistry C, 2011. **115**(51): p. 25234-25240.
143. Petcharoen, K. and A. Sirivat, *Synthesis and characterization of magnetite nanoparticles via the chemical co-precipitation method.* Materials Science and Engineering B-Advanced Functional Solid-State Materials, 2012. **177**(5): p. 421-427.
144. Deng, J.H., et al., *Simultaneous removal of Cd(II) and ionic dyes from aqueous solution using magnetic graphene oxide nanocomposite as an adsorbent.* Chemical Engineering Journal, 2013. **226**: p. 189-200.
145. Kumar, A.S.K. and N. Rajesh, *Exploring the interesting interaction between graphene oxide, Aliquat-336 (a room temperature ionic liquid) and chromium(VI) for wastewater treatment.* Rsc Advances, 2013. **3**(8): p. 2697-2709.
146. Rajesh, N., et al., *Trialkylamine Impregnated Macroporous Polymeric Sorbent for the Effective Removal of Chromium from Industrial Wastewater.* Journal of Chemical and Engineering Data, 2011. **56**(5): p. 2295-2304.
147. Kalidhasan, S., et al., *An efficient ultrasound assisted approach for the impregnation of room temperature ionic liquid onto Dowex 1 x 8 resin matrix and its application toward the enhanced adsorption of chromium (VI).* Journal of Hazardous Materials, 2012. **213**: p. 249-257.
148. Kumar, A.S.K., et al., *Application of Cellulose-Clay Composite Biosorbent toward the Effective Adsorption and Removal of Chromium from Industrial Wastewater.* Industrial & Engineering Chemistry Research, 2012. **51**(1): p. 58-69.
149. Singh, V., et al., *Efficient chromium(VI) adsorption by Cassia marginata seed gum functionalized with poly(methylmethacrylate) using microwave irradiation.* Industrial & Engineering Chemistry Research, 2008. **47**(15): p. 5267-5276.
150. Kumar, A.S.K., et al., *Effective adsorption of hexavalent chromium through a three center (3c) co-operative interaction with an ionic liquid and biopolymer.* Journal of Hazardous Materials, 2012. **239**: p. 213-224.
151. Kalidhasan, S., et al., *Ultrasound-assisted preparation and characterization of crystalline cellulose-ionic liquid blend polymeric material: A prelude to the study of its application toward the effective adsorption of chromium.* Journal of Colloid and Interface Science, 2012. **367**: p. 398-408.
152. Sahu, M.K., et al., *Removal of Pb (II) from aqueous solution by acid activated red mud.* Journal of Environmental Chemical Engineering, 2013. **1.4** p. 1315-1324.
153. Salmimies, R., *Acidic dissolution of iron oxides and regeneration of a ceramic filter medium.* Acta Universitatis Lappeenrantaensis, 2012.

154. Lagergren, S., K. Sven, and Vetenskapsakad, *Citation review of lagergren kinetic rate equation on adsorption reactions.* Handl, 1898. **24**: p. 1-39.
155. Ho, Y.S., *Review of second-order models for adsorption systems.* Journal of Hazardous Materials, 2006. **136**(3): p. 681-689.
156. Elouear, Z., et al., *Heavy metal removal from aqueous solutions by activated phosphate rock.* Journal of Hazardous Materials, 2008. **156**(1-3): p. 412-420.
157. Kumar, A.S.K., et al., *Application of cellulose-clay composite biosorbent toward the effective adsorption and removal of chromium from industrial wastewater.* Industrial & Engineering Chemistry Research, 2011. **51.1**: p. 58-69.
158. Malkoc, E. and Y. Nuhoglu, *Determination of kinetic and equilibrium parameters of the batch adsorption of Cr(VI) onto waste acorn of Quercus ithaburensis.* Chemical Engineering and Processing, 2007. **46**(10): p. 1020-1029.
159. WooáLee, J. and S. BináKim, *Enhanced Cr (VI) removal using iron nanoparticle decorated graphene.* Nanoscale, 2011. **3**(9): p. 3583-3585.
160. Zhu, J., et al., *Mesoporous magnetic carbon nanocomposite fabrics for highly efficient Cr (VI) removal.* Journal of Materials Chemistry A, 2014. **2**(7): p. 2256-2265.
161. Tian, Z., et al., *Synthesis of poly (m-phenylenediamine)/iron oxide/acid oxidized multi-wall carbon nanotubes for removal of hexavalent chromium.* RSC Advances, 2015. **5**(3): p. 2266-2275.
162. Boparai, H.K., M. Joseph, and D.M. O'Carroll, *Kinetics and thermodynamics of cadmium ion removal by adsorption onto nano zerovalent iron particles.* Journal of Hazardous Materials, 2011. **186**(1): p. 458-465.
163. Zhu, J., et al., *One-pot synthesis of magnetic graphene nanocomposites decorated with core@ double-shell nanoparticles for fast chromium removal.* Environmental science & technology, 2011. **46**(2): p. 977-985.
164. Liu, Y., et al., *Synthesis of manganese dioxide/iron oxide/graphene oxide magnetic nanocomposites for hexavalent chromium removal.* RSC Advances, 2015. **5**(67): p. 54156-54164.
165. Hall, K.R., et al., *Pore-and solid-diffusion kinetics in fixed-bed adsorption under constant-pattern conditions.* Industrial & Engineering Chemistry Fundamentals, 1966. **5.2**: p. 212-223.
166. Mishra, R.R., P. Chandran, and S.S. Khan, *Equilibrium and kinetic studies on adsorptive removal of malachite green by the citrate-stabilized magnetite nanoparticles.* RSC Advances, 2014. **4**(93): p. 51787-51793.
167. Hammud, H.H., A. Shmait, and N. Hourani, *Removal of Malachite Green from water using hydrothermally carbonized pine needles.* RSC Advances, 2015. **5**(11): p. 7909-7920.
168. Ahad, S., et al., *Adsorption studies of Malachite green on 5-sulphosalicylic acid doped tetraethoxysilane (SATEOS) composite material.* RSC Advances, 2015. **5**(112): p. 92788-92798.
169. Sun, H., L. Cao, and L. Lu, *Magnetite/reduced graphene oxide nanocomposites: one step solvothermal synthesis and use as a novel platform for removal of dye pollutants.* Nano Research, 2011. **4**(6): p. 550-562.

170. Liu, A., et al., *One-pot hydrothermal synthesis of hematite-reduced graphene oxide composites for efficient removal of malachite green from aqueous solution.* RSC Advances, 2015. **5**(22): p. 17336-17342.
171. Ai, L., et al., *Activated carbon/CoFe 2 O 4 composites: Facile synthesis, magnetic performance and their potential application for the removal of malachite green from water.* Chemical Engineering Journal, 2010. **156**(2): p. 243-249.
172. Islam, M. and R. Patel, *Polyacrylamide thorium (IV) phosphate as an important lead selective fibrous ion exchanger: synthesis, characterization and removal study.* Journal of hazardous materials, 2008. **156.1**: p. 509-520.
173. Gupta, V.K., et al., *Equilibrium uptake and sorption dynamics for the removal of a basic dye (basic red) using low-cost adsorbents.* Journal of Colloid and Interface Science, 2003. **265**(2): p. 257-264.
174. Ghaedi, M., et al., *Artificial neural network-genetic algorithm based optimization for the adsorption of phenol red (PR) onto gold and titanium dioxide nanoparticles loaded on activated carbon.* Journal of Industrial and Engineering Chemistry, 2015. **21**: p. 587-598.
175. Mittal, A., et al., *Adsorption studies on the removal of coloring agent phenol red from wastewater using waste materials as adsorbents.* Journal of colloid and interface science, 2009. **337**(2): p. 345-354.
176. Chaudhuri, H., et al., *SBA-16: Application for the removal of neutral, cationic, and anionic dyes from aqueous medium.* Journal of Environmental Chemical Engineering, 2016. **4**(1): p. 157-166.
177. Iqbal, M.J. and M.N. Ashiq, *Adsorption of dyes from aqueous solutions on activated charcoal.* Journal of Hazardous Materials, 2007. **139**(1): p. 57-66.